DISS. ETH NO. 25426

QUANTITATIVE MICRO XRF MAPPING OF CHLORIDES:
POSSIBILITIES, LIMITATIONS AND APPLICATIONS,
FROM CEMENT PASTES TO DIGITAL CONCRETE

A thesis submitted to attain the degree of

DOCTOR OF SCIENCES of ETH ZURICH

(Dr. sc. ETH Zurich)

presented by

PAULA CECILIA BRAN ANLEU

M. Sc., University of California, Berkeley

born on 23.07.1985

citizen of Guatemala

accepted on the recommendation of

Prof. Dr. Robert J. Flatt, examiner
Fernand Deillon, co-examiner
Prof. Dr. Mette R. Geiker, co-examiner
Dr. Timothy Wangler, co-examiner

2018

To my parents

Acknowledgements

I am grateful to the members of my doctoral committee for revising this manuscript and for their help in getting it to its final shape: my thesis supervisor Prof. Dr. Robert J. Flatt, Fernand Deillon (TFB AG, Wildegg Switzerland), Prof. Dr. Mette R. Geiker (Norwegian University of Science and Technology), Dr. Timothy Wangler (ETH Zurich). I would also like to thank Prof. Dr. Andreas Wieser for agreeing to chair my doctoral examination.

I would like to acknowledge the people who contributed in one way or another to this work. I am thankful to Asel Maria Aguilar Sanchez (ETH Zurich), Dr. Leonel Aguilar Melgar (ETH Zurich), Carolina Boschmann (ETH Zurich), Dr. Gabriela Bran Anleu (SANDIA), Jefferey Davis (PNDetector GmbH), Fernand Deillon (TFB AG), Stephan Frey (TFB AG), Dr. Kevin L. Keys (UCSF), Dr. Marta Palacios (IETCC Madrid), and Dr. Yurena Segui Femenias (ETH Zurich) for supporting me with experimental work, data analysis or collection, and/or for engaging in insightful discussions. I would especially like to thank Prof. Dr. Francesco Caruso (UiO) for his extraordinary help and contribution in the shaping of the chapter concerning the method development; Dr. Ekaterina

Pomjakushina (PSI) for providing access to the equipment I used for this work, and for the initial help in understanding the ways of data collection using micro XRF; and Dr. Timothy Wangler (ETH Zurich) for his time and the many helpful, and encouraging discussions throughout this six-years.

I would like to express my deep gratitude to my supervisor Prof. Dr. Robert J. Flatt for his patient guidance and valuable support on this crazy journey, and for his valuable and constructive suggestions during the planning and development of this thesis. I would also like to truly thank him for placing his confidence in my work, which at (many) times gave me the strength to continue.

My very special gratitude goes out to my mentor Dr. Timothy Wangler for the many, many encouraging pep talks he gave me over the course of the PhD. I am very thankful to him for restoring my "belief in myself" when I couldn't find the strength to do it myself. I will always remember and cherish the support he's given me throughout the last years, especially in the last months before submitting this thesis; without his support I might never have managed to believe this was possible.

I would also like to thank all the past and current members of the PCBM and corrosion research groups, for creating a great and enjoyable working environment. Every single person in the group contributed to make my PhD journey a very special, extremely enjoyable, and incredibly rewarding experience. I especially would like to openly thank the following members for being not only my colleagues, but also my friends and at times my moral support: Delphine, Elizaveta, Francesco, Giulia, Lex, Matteo, Nicolas, Omar, Prannoy, Tim, Thibault, and Ylenia. All the hours spent outside the lab made this experience unforgettable and even more enjoyable. A special thanks also goes

out to my two Spanish guardian angels, Ana and Yurena. I thank them for their moral support in the last weeks before the thesis submission, and an extra thank you to Ana for feeding me when I would forget. (¡Gracias frijoles!).

Thank you to my officemates (past and current) for making my working space the most delightful distraction. The ability to have more than two conversations at the same time with four people actively involved is something I will cherish forever. The ones who have left, Delphine and Prannoy; the ones who just got there, Federico and Luigi; and the one constant in this messy chaos, Giulia. The atmosphere in HIF E 17.1 made coming to the office a joy.

I thank my friends, who are scattered around the world, for their support even when we are in very different time zones. I explicitly want to thank Ana Luz Acevedo, Andrea Viteri, Anna Buser, Claudia Meneses, Ilgin Guler, Joanna Huey, Kevin Keys, Leonel Aguilar, Lucia Rosales, Marielos Garcia, Marlen Morales, Shreya Ramesh, and Ximena Meneses.

The time at ETH would not have been the same if it wasn't for the people who eventually became my close friends. I especially want to thank Delphine Marchon for being a caring friend, even if it took Giulia and I ages to make her comfortable enough to hug us, and for our shared love for (large) dogs and super kondi. I am also grateful to Prannoy Suraneni for being a wonderful friend. Circumstances, distance, and time have distanced us, but I will always treasure your kind and unconditional support. Your weird sense of humor, and lack of working taste buds are some of the things I will always remember.

People say: "friends are the family you choose," and this is the case for Giulia Gelardi and Ylenia Praticò. Over the course of my PhD these two people became my family.

I am grateful to Ylenia for helping me put my anxieties into perspective, and for (most times) knowing me better that I know myself. Thank goodness for Sziget! Thank you for our TWD and GoT nights, and for putting up with my cheesiness. You're the kindest person I have ever met; I don't know what I would have done without my supporting sister (from another family).

I am forever grateful to Giulia for being there for me for every up and down in the last six years. From our first date at Big Ben Pub, it was clear to me we'd be at least good friends for years to come. Quoting a song: "Though we don't share the same blood, you're my [sister] and I love you. That's the truth." Thank you for your many indispensable hugs.

And lastly, but most importantly, I want to thank my family. I am eternally grateful to my parents, Cecilia and Walter Bran, for setting the model of how to be the person I am today. Their belief in me, and their constant and unconditional support have always given me the strength to follow my dreams no matter how crazy they may seem. I dedicate this work to them. I also want to thank my sister Gaby, for always being there for me, as my eye opener, as my certainty, as my support, as my best friend. My life would be a disaster without you. Thank you to my brother Andre, for being there for me in his own weird way. Somehow you manage to show you care with very few words or gestures. I would not be the human I am without these four people.

Abstract

Among the principal reasons for premature deterioration in reinforced concrete is chloride-induced corrosion. In this respect, chloride distribution is an important factor within the greater endeavor of better understanding of chloride transport in concrete. In the last few decades little progress has been made about the fundamentals of chloride ingress into concrete. The reliable quantification of chlorides can therefore provide valuable insights into the important societal objective of improving service life predictions of reinforced concrete.

In practice, oversimplified material models are commonly used, many of which were developed decades ago. This may now be one of the greatest limitations to the application of reliable chloride transport models in practice and is specifically the problem to which we want to contribute with useful, spatially determined chloride characterization.

One of the most widely used techniques for chloride quantification in concrete includes a destructive sample preparation for either titration (powder dissolved in nitric acid) or XRF (powder fused into pellets), which provide averaged information over a volume of sample. However, in order to obtain quantitative

mapping of chlorides, a more effective approach with a higher spatial resolution is needed.

A new method to quantify chlorides with a (semi) non-destructive approach, whose limits of quantification are suitable for fundamental studies of the behavior of chlorides in concrete, is described. The achieved levels of trueness are comparable to those indicated by the international standard organization procedure for cement chemical analysis with XRF. While establishing this method, we also demonstrated that Support Vector Machines (SVMs) offer a worse calibration procedure than peak integration, despite the advantages that SVMs can theoretically claim because of matrix effects in micro XRF measurements.

A series of experiments was attempted, to combine the quantification method by micro XRF with that of the free chloride measurement method by ion selective electrodes. Unfortunately, this work mainly highlighted shortcomings of these electrodes under the specific conditions of our experiments of diffusion and capillary transport respectively.

The same experiments also led to a number of important unexpected observations. Indeed, the chemical imaging of cement paste samples subjected to diffusive chloride transport revealed certain inhomogeneities that can be described as "channels of accelerated chloride transport". These have a major effect on chloride transport, are very localized, and would not have been detected without the use of micro-XRF mapping. These channels can have major implications for the durability of cementitious systems, such as grouts.

With respect to the chloride sensors, we underline that the so called streaming potentials proved to produce a significant artifact in capillary rise experiments.

This should be considered if such ion selective electrodes are to be used in situations where data is needed at times when the level of water saturation in concrete is changing.

Finally, the use of qualitative micro XRF chemical imaging proved that the presence of cold joints is a potentially detrimental aspect for a 3D printed cementitious system in terms of its durability. Micro XRF offered a higher resolution than neutron imaging to identify cold joints. Also, since micro XRF is much easier to implement it has the potential to become a preferred method for studying the respective durability of the vast number of concretes that can be produced in digital fabrication, and for which inhomogeneous microstructures are a great concern.

x

Kurzfassung

Einer der Hauptgründe für einen vorzeitigen Zerfall von Stahlbeton ist chloridinduzierte Korrosion. Die Chloridverteilung ist somit ein wichtiger Parameter im Bestreben ein besseres Verständnis des Chloridtransports im Beton zu erhalten.

In den letzten Jahrzehnten wurde wenig Fortschritt in der Grundlagenforschung des Chlorideintrags in Beton erreicht. Die zuverlässige Quantifizierung von Chloriden kann somit wertvolle Erkenntnisse für das wichtige gesellschaftliche Ziel der Verbesserung von Lebensdauervorhersagen von Stahlbeton zur Verfügung stellen.

In der Praxis werden häufig stark vereinfachte Materialmodelle genutzt; viele davon wurden vor Jahrzehnten entwickelt. Dies mag eine der grössten Einschränkungen für die Anwendung von verlässlichen Chloridtransportmodellen in der Praxis sein und ist besonders die Fragestellung, zu welcher wir mit einer nützlichen, räumlich definierten Chloridbestimmung beitragen wollen.

Eine der meistverbreiteten Methoden für Chloridquantifizierung in Beton beinhaltet zerstörende Probenpräparation entweder für Titration (Pulverauflösung in Salpetersäure) oder für XRF (Pulver in Pellets gepresst), welche gemittelte Informationen über das Probenvolumen liefern. Um jedoch eine quantitative Chloridverteilung zu erhalten, ist ein effektiverer Ansatz mit einer grösseren räumlichen Auflösung erforderlich.

Es wird eine neue Methode zur Chloridquantifizierung mit einem zerstörungsarmen Ansatz beschrieben, dessen Grenzen für fundamentale Studien von Chloridverhalten in Beton geeignet sind. Die erreichte Genauigkeit ist vergleichbar mit derjenigen, die von internationalen Normungsorganisationen für die Methode der chemischen Zementanalyse mit XRF angegeben wird. Während der Etablierung der Methode, zeigten wir, dass Support Vector Machines (SVMs) eine ungenauere Kalibrierung ermöglichen als die Messung der Intensität der Röntgenstrahlung, trotz den Vorteilen, die die SVMs theoretisch wegen möglicher Matrixeffekten in Mikro-XRF-Messungen für sich beanspruchen.

Eine Serie von Experimenten versuchte, die Quantifizierungsmethode nach Mikro-XRF mit der Messung von freien Chloriden mit ionenselektiven Elektroden zu kombinieren. Leider beleuchtete diese Arbeit hauptsächlich die Unzulänglichkeiten dieser Elektroden unter den spezifischen Bedingungen in unseren Diffusions-, bzw. Kapillaritätsexperimenten.

Dieselben Experimente führten allerdings zu einer Anzahl an wichtigen, unerwarteten Beobachtungen. Die chemische Färbung von Zementleimproben, die zuvor einem diffusionskontrollierten Chloridtransport ausgesetzt wurden, zeigte eine gewisse Inhomogenität, die als „Kanäle für beschleunigten

Chloridtransport" beschrieben werden können. Diese haben einen bedeutenden Einfluss auf den Chloridtransport, sind sehr lokal, und wären ohne den Gebrauch von Mikro-XRF-Mapping nicht entdeckt worden. Diese Kanäle können bedeutende Auswirkungen auf die Dauerhaftigkeit von zementösen Systemen, wie z.B. Mörtel, haben.

In Bezug auf die Chloridsensoren, betonen wir, dass die so genannten Strömungspotentiale ein signifikantes Artefakt für Kapillaritätsexperimente sein können. Das sollte bei Verwendung von ionenselektiven Elektroden in wechselnden Wassersättigungsgraden in Beton berücksichtigt werden.

Die Verwendung von qualitativer Mikro-XRF chemischer Bildgebung zeigte schlussendlich, dass das Vorhandensein von Betonierfugen ein potentiell schädlicher Aspekt für 3D-gedruckte zementöse Systeme in Bezug auf Dauerhaftigkeit darstellen. Mikro-XRF ermöglicht eine höhere Auflösung als Neutron-imaging zur Identifizierung von Betonierfugen. Da die Mikro-XRF-Methode wesentlich leichter zu implementieren ist, hat es das Potenzial, die bevorzugte Methode für die Untersuchung der Dauerhaftigkeit einer Grosszahl von Betonen zu werden, die in der digitalen Fabrikation verwendet werden und für welche inhomogene Mikrostrukturen eine grosse Herausforderung sind.

Table of Contents

Chapter 1 - Introduction

The present chapter is partly based on a section of a grant proposal written for the ETH Grant (ETH-33 12-1) and partly on the introduction of a paper published in the Microchemical Journal:

 "Standard and sample preparation for the micro XRF quantification of chlorides in hardened cement pastes"

By P. Bran-Anleu, F. Caruso, T. Wangler, E. Pomjakushina, R. J. Flatt [1]

1.1. General introduction

Civil engineering infrastructure is the mainstay of society and most of it is built of concrete. As a result, the durability of this material is a growing concern since a large amount of private and public budget goes to the repair and restoration of prematurely deteriorated infrastructure [2–4]. One of the principal reasons for such deterioration in reinforced concrete is chloride-induced corrosion, where chloride ions penetrate the concrete cover and degrade the steel reinforcement once a certain concentration is reached at the interface [2–4]. A recent review by Angst and Elsener [5] affirms that in the early 2000s in the United States of America alone, chloride-induced-corrosion-related repair costs were higher than the combined costs for heart disease and cancer. Yet, little progress has been made to understand the fundamentals of chloride ingress into concrete [3,5].

Understanding them is however the first step towards being able to more accurately predict the service life of reinforced concrete structures exposed to aggressive chloride environments [6].

A reason for that can be found in the lack of analytical methods for the detection of chlorides able to take into account the nonhomogeneous ingress of chlorides in concrete and the resulting spatial variability thereof. The determination of chloride content generally consists of drilling into concrete and collecting the powder at different depths or of taking cores followed by a cutting or grinding procedure before treating chlorides to establish their profiles. Thus, these methods deliver the average chloride content in the sampled volume and neglect the spatial variability of chlorides in concrete [7]. Furthermore, in literature, data has been reported mostly on a macroscopic and averaged out scale and the spatial variability remains at best only poorly taken into account [7–9].

Concerning the transport of chlorides into concrete, this only rarely occurs with saturated concrete, except in submerged parts of marine structures. As briefly discussed in Chapter 2, this situation renders the modelling of chloride transport more complex, which is why it has not been dealt much in the past literature. However, in more recent years some researchers have been developing models for chloride penetration into partly saturated concrete [10]. Such research is important to adequately predict the amount of chlorides that can enter concrete over time, something that is paramount for service life predictions.

Even if the transport mechanisms of chlorides in concrete are not fully understood [2], it is certain that diffusion of chloride ions and capillary suction of chloride-contaminated water are both possible transport mechanisms for chlorides in partly saturated concrete [11]. In this respect it is worth noting that

a recent review on the prospect of predicting chloride transport in concrete reached very pessimistic conclusions [3]. This is because practicing engineers rely on oversimplified material models, many of which were developed a few decades ago. Today's practice thus relies on empirical equations based on previous, disused experiences. This is now one of the greatest limitations to the application of reliable chloride transport models in practice and is specifically the problem to which we want to contribute with useful, spatially determined chloride characterization.

In addition to determining the total amount of chlorides that can ingress concrete over time, it is also important to know their spatial distribution, an issue that is currently given only very little attention, as mentioned above. Therefore, reliable and cost-effective characterization techniques must become more widely available. Other methods have been developed with this in mind [8,9,12,13], where the approach mainly consists on determining the average chloride contents within a certain volume of a sample, however they lack basic method validation data. Additionally, very few details are offered in terms of the preparation of the standards for the calibration.

Developing and applying a method for determining the spatial distribution of chlorides has been the challenge addressed in this thesis. For the first time, it presents a reliable micro XRF method able to spatially measure and quantify chlorides in cement paste. In doing so, this thesis first establishes the necessary protocols for the method, and then moves on to apply it on samples exposed to chlorides. It examines situations of diffusion and capillary rise in Chapter 4, evidencing at the same time the dramatic consequences that "visually undetectable bleeding" can have on chloride ingress. Furthermore, Chapter 5

presents a case in which it is necessary to have a spatial resolution, because the presently used chloride profile determination techniques would produce highly misleading results.

1.2. Objective of the thesis

The objective of this study is to develop a method that allows the quantification of chlorides using micro XRF chemical maps. This represents a first step to obtain data on the microscopic and macroscopic level, granting high spatial resolution.

In this thesis, cement paste was used for the development of the method. Factors as cement composition and water cement ratio were examined in terms of their effect on chloride quantification. Additionally, the quantification was extended to mortars and guidelines for doing with limited additional calibration work are proposed.

Those steps are important for the end goal of developing this method for concrete samples, for which the original composition is not necessarily known when these are taken for standing structures. Moreover, for field exposure, it has been shown that, although exposure may be homogenous, the chloride front may not be (macroscopically) homogeneous whatsoever [7]. At the scale of concrete cover (the distance between exposed surface to interface with the reinforcing steel), this can play a major influence on corrosion initiation. Therefore, an important objective of this thesis is to develop a methodology allowing to exploit the spatial resolution offered by micro XRF for mapping chloride in cementitious materials.

The advantages of chloride mapping include the prospect to achieve a more detailed understanding of chloride transport mechanisms, better accounting for

the various factors that can influence it, such as material properties and exposure conditions [2]. This remains a challenge despite considerable effort having been expended in the development of models for the prediction of the life service of reinforced concrete [11]. Thus, one of the goals of this thesis, through developing chloride mapping is to contribute to provide the means of acquiring higher quality data allowing to establish more reliable chloride transport models and service life predictions.

The scope of the ultimate goal behind developing this method of chloride mapping can be illustrated in Figure 1.1, where the different key challenges for a better understanding and description of chloride transport are presented in a ternary diagram.
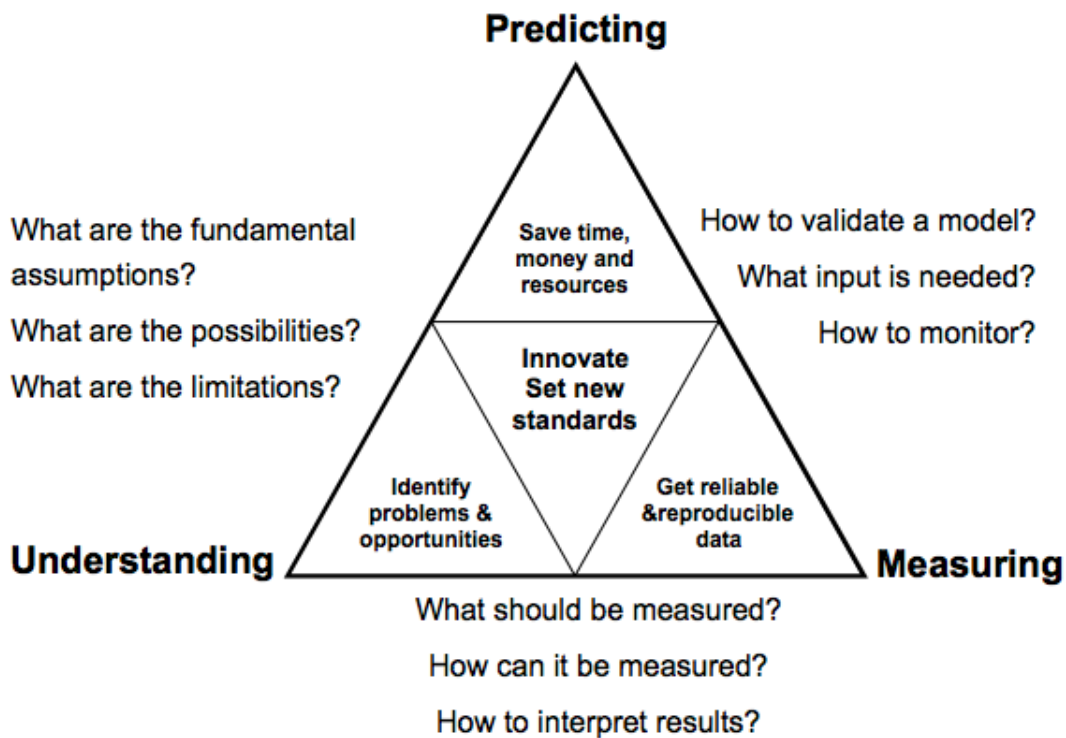
Figure 1.1: Conceptual summary of the ultimate goal behind the development of the method for the quantification of chlorides using micro XRF chemical maps, described in chapter 3 of this thesis.

In addition, this thesis aims at illustrating cases in which chloride mapping acts as an "eye opener" into cases of inhomogeneous chloride ingress. This is illustrated mainly by two cases including "visible undetectable bleeding" as well as cold joints in 3D extrusion printing of concrete.

1.3. Structure of the thesis

The manuscript is structured as follows:

Chapter 2 presents the state of the art, which is divided into two parts. The first part gives an overview of chlorides and their role in reinforced concrete. More specifically, it reviews some of the currently used methods to test the concrete's resistance to chloride penetration and their limitations. It also reviews some of the methods used to quantify chlorides in concrete. Finally it introduces some basic concepts regarding layer extrusion 3D printed concrete. The second part introduces basic concepts regarding X ray fluorescence, and the machine learning technique called Support Vector Machines.

Chapter 3 thoroughly describes the protocols for the developed method to quantify chlorides in hardened cement pastes using micro XRF. The method is tested against different cements and a different water cement ratio. The relevant statistical figures of merit are presented. Additionally, it is shown that data processing with Support Vector Machines, though advantageous in many fields, proved to be less effective than our linear method to quantify chlorides in cement pastes.

Chapter 4 deals with the combination of the micro XRF method with ion selective electrodes. Though results were not as expected, they are presented and

discussed because they generated a number of important and unexpected observations. In particular, they illustrate the limitations and significance of both methods. Some important insights and conclusions are found.

Chapter 5 deals with the importance of having a spatial resolution quantification method in the field of digitally fabricated concrete. Although the analysis that is presented in this chapter in only qualitative, it revealed the implications of having cold joints in layer extruded 3D printed concrete on its durability.

Chapter 6 presents a summary of the results, and details the conclusions achieved in this thesis. It also presents an outlook of the possible developments in the research regarding chlorides in concrete.

Chapter 2 - State of the Art

Part I: Chlorides and their role in reinforced concrete

Sections 2.1 and 2.4 of the present chapter are based on a section of a grant proposal written for the ETH Grant (ETH-33 12-1).

Chlorides can be present in concrete in two forms, as free and bound chlorides. The free chlorides are dissolved in the pore solution, and it is this portion of the total amount of chlorides that can be detrimental to the reinforcing steel in concrete. Once the free chlorides reach the reinforcement, the protective passivation layer on the steel can be damaged and corrosion occurs (*chloride induced corrosion*). The rest of the chlorides are either chemically bound into compounds such as Friedel's salt or physically adsorbed to the phases of the paste. Generally, bound chlorides are harmless to reinforcing steel, however it has been found that they can be released into the pore solution given certain conditions such as carbonation or sulphate attack [14,15]. The capability of concrete to bind chloride ions depends on different factors, primarily the type of cement, the pH of the pore solution, and the amount C-S-H [16–18]. The binding capacity is therefore not constant, and so it plays an important role in the displacement of chlorides within concrete's matrix [2]

Typically, chloride ions penetrate hardened concrete that is exposed to sea water or deicing salts. They can also be present in the fresh mix, if chloride contaminated water or aggregates are used. Chloride ingress involves complex physical and chemical processes, and is dependent on the following factors [2]:

- Environmental exposure and the variation thereof (temperature, humidity and exposure to liquid water)

- Material properties, which do not only depend on the concrete composition, but also evolve with time

In particular, the above factors influence the nature of the rate limiting for chloride transport (diffusion or convection) and determine which chloride binding, physical and chemical, may slow down any of those processes.

Understanding the fundamentals of chloride ingress into concrete is therefore the first step towards being able to more accurately predict the service life of reinforced concrete structures exposed to aggressive chloride environments. There exist many methods and models to study the transport of chlorides in concrete, but until now researchers and practitioners have not reached a general agreement on a single test method or predictive model due to the complexity of the process [2,3].

2.1. Measuring concrete's resistance to chloride ingress

The process of chloride penetration is rather slow, and it cannot be defined in a time frame that is suitable as a quality control measure when considering ingress

distances typically encountered in practice. Because of this, a wide variety of methods that accelerate the rate of penetration were developed a few decades ago [2].

By the 1980s, two test methods had been developed in North America [2]. One of them is the Standard Method of Test for Resistance of Concrete to Chloride Ion Penetration, or AASHTO T295 (The ponding test)[2,19,20]. It is a long term (non-steady state) test that consists on ponding a 3 % NaCl solution on the top a 75-mm thick slab (Figure 2.1). After the sample is conditioned to the prescribed specifications, the solution is ponded on the top surface for 90 days, while the bottom surface is exposed to a drying condition. At the end of the 90 days, the samples are removed from the drying environment and the chloride concentration of 1.5 cm thick slices is determined by a usual profile grinding technique [20,21].

The ponding test provides a simple one-dimensional chloride profile. On the other hand, one of the main limitations of this method is the long exposure time, which makes it unpractical for many construction projects [2]. Another limitation is the fact that very little information is being gathered in the 1.5 cm sampling process. One cannot say much about the chloride profile within that slice, since only the average chloride concentration is determined. A clear example of this issue is well described by [21], where there could be two samples with the same average chloride concentration at a certain depth, where in one of them the distribution of chlorides is more uniformly distributed than in the other (where for example a very high concentration is found near the surface). In the later concrete, a critical chloride concentration might be reached much sooner than in

the first concrete, and this distinction cannot be detected with such sampling procedures.
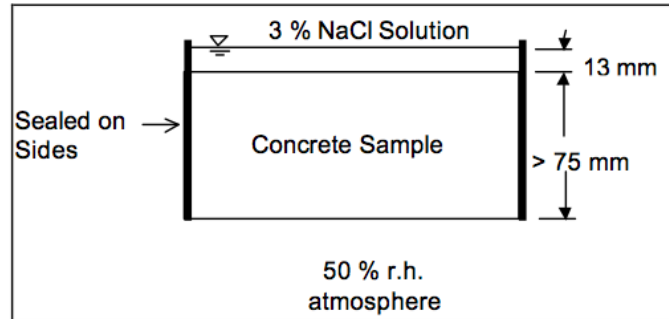
Figure 2.1: Schematic of AASHTO T259 (Ponding test) [21]

The second test method is the Electrical Indication of Concrete's Ability to Resist Chloride Ion Penetration or AASHTO T277 (ASTM C1202 – Rapid Chloride Permeability Test). This is an accelerated test method (non-steady state) that consists of subjecting a water saturated 50 mm thick, 100 mm diameter concrete disk to a DC voltage for 6 hours in a setup such as the one showed in Figure 2.2. The total charge passed is a measure of the electrical conductance of the concrete during the period of the test. Then the value of the total charge passed is compared to a prescribed table to determine the concrete's chloride ion penetrability [21,22]. Even if this method has been implemented by many practitioners, it has been subject to many criticisms in the literature [19,23,24]. The main criticisms include the fact that the current passed is a function of all the ions in the pore solution and not just chlorides, steady-state migration is not yet achieved before the measurements take place, and the high voltage tends to increase the temperature of the samples, especially for poor quality concretes making them seem worse than they are [21].
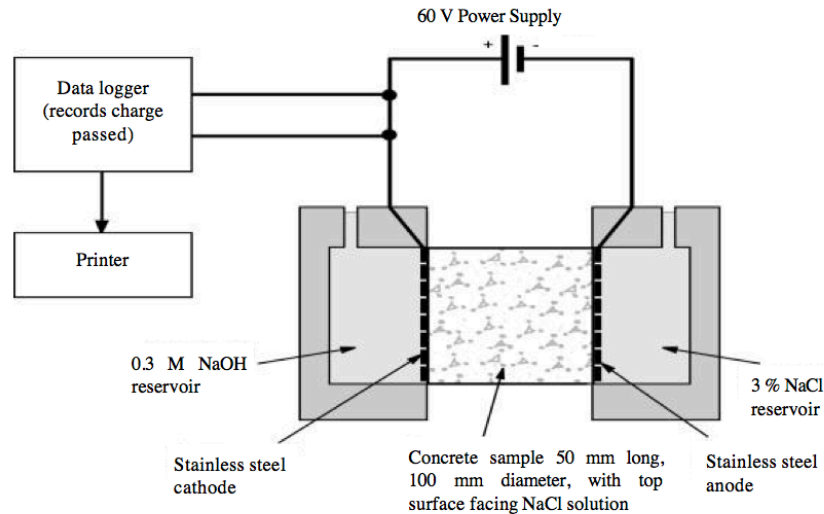
Figure 2.2: Schematic of the AASHTO T277 (ASTM C1202) test setup [21].

In the decades that followed, several more tests were developed and standardized in Europe. The methods above were adopted and modified as scientists gathered more insight and knowledge about the complexity of the chloride transport in concrete.

In addition to the heavily accelerated tests, different versions that avoided acceleration were developed. Yet, these methods are laborious, and though they are time consuming, they are still not representative of the time scale in reality. Moreover, it is not always convenient or economically feasible to perform them [2,19]. Nowadays, Swiss standards implement a particular procedure for determining the chloride resistance of concrete in accordance to the European standards EN 206-1 and EN 12 390-2 [25]. The test method is similar to the Rapid Migration Test [26]. This is in a sense a combination of an accelerated test and a non-accelerated test (the ponding test and the migration test), as is described in SIA 262/1 Appendix B [25] (Figure 2.3).
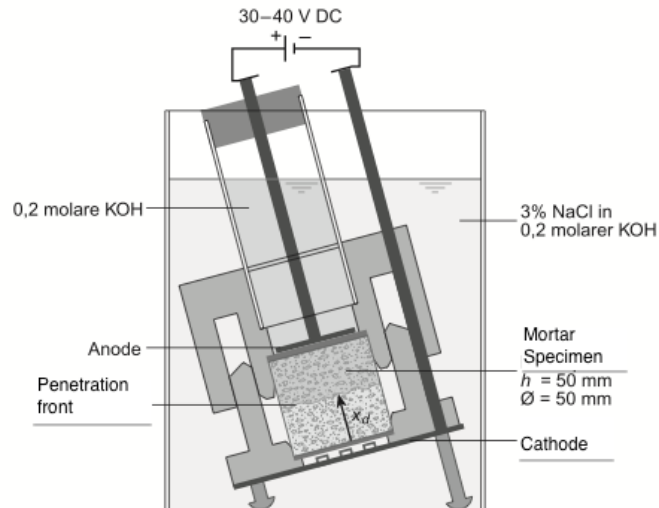
Figure 2.3: Schematic of the Swiss Standard procedure to measure concrete's resistance to chloride ingress [25].

In short, the previously mentioned methods are all macroscopic methods, which either need a long period of time, or a strong acceleration to allow detection of any phenomena within a reasonable time frame. The problem with time consuming tests is not only economical, but that results are not available in the time frame needed in practice. The alternative accelerated tests generally implement an electrical current to accelerate ionic movement. The challenges are, first, that in concrete there are other ions than just chlorides. The measurement of the total current passing through the concrete sample is a function of the amount and type of ions. Secondly, high voltage drops may induce heat which in turn will affect the flow speed. Third, integrating a current does not mean that there is a distinction between free and bound chlorides [11,19]. Last but not least, accelerated test often use excessively high chloride concentrations that favor the chloride binding and the transport of chlorides, because the electrical coupling of ions significantly influences the ingress rate [27]. In other words, chloride binding, which works against chloride ingress, is not simply a function of the

amount of chlorides in the pore solution, but it is strongly influenced by the composition of the pore solution, especially the pH [27].

2.2. Measuring chloride ions in concrete

In order to analyze or interpret the data collected with the methods described above, the amount of chloride ions in the specimen needs to be somehow quantified or at least measured. There are several ways to do this, some of which will be briefly described in the following paragraphs. In all the methods discussed, it is important to consider the difference between obtaining free, bound and/or total chlorides. Another significant point to consider is the variable nature of chloride transport within the concrete. It has been acknowledged that chloride transport in concrete is a non-homogeneous process, and that it does not lead to a uniform front even if the exposure is monitored and kept homogenous [7,28–30]. Moreover, pitting corrosion has a stochastic nature as it does not necessarily initiate at the locations where the chloride content is highest [31], but it depends on the probability of the chloride front reaching a vulnerable part of the reinforcement.

2.2.1. Qualitative colorimetric indicator

The technique consists of spraying a freshly broken concrete surface with a silver nitrate solution (typically 0.1 N AgNO3) [15]. When the solution is sprayed on chloride contaminated concrete, the chloride ions bind with the silver to produce silver chloride staining it with a white color. In the absence of chlorides, the silver bonds with hydroxides staining it with a light brown. This method offers a fast way for a visual inspection and for a rough estimate of the chloride ion

penetration depth [32]. Normally, it is used for specimens tested with the different variations of the Rapid Chloride Penetrability Test.

2.2.2. Acid-soluble chloride content- quantitative analysis

Most of the standardized tests require the samples to be ground off in layers parallel to the exposed surface. There are different techniques to obtain a powdered sample of the specimen. One way is, for example, to use a rotary impact drill and drill the sample perpendicular to the surface to a specified depth [33]. Another way is to slice, crush and grind the sample [25]. Once the powder sample is prepared as per the chosen standardized test (usually a powder that passes through a specific sieve), one can proceed to analyze it to determine its chloride content.

The most commonly used methods are the Volhard titration method [34], or the potentiometric titration method [33,35]. The sample is thus dissolved in nitric acid. In most cases, the acid-soluble chloride content is the total chloride content [35,36]. The Volhard method is an indirect titration procedure, used to determine the anions that precipitate with silver. The potentiometric titration method uses a silver electrode to measure the potential difference, which is a function of the concentration of silver ions in solution.

2.2.3. X-ray fluorescence spectroscopy- quantitative analysis

Even though the previously discussed techniques are still widely used, nowadays, X-ray fluorescence is more frequently implemented to determine the total chloride content in powdered samples [36,37]. In this case, the sample is either pressed into pellets or fused as glass beads before the sample is analyzed

[38]. As it was mentioned in Section 1.1, a few recent studies implement this technique to determine the chloride content as explained in [8,9,12]. This technique requires the proper and careful development of a calibration curve using standards with known chloride concentrations usually measured by other means.

2.2.4. Ion selective electrodes

A valid and convenient technique to measure and quantify free chlorides in concrete is the use of ion selective electrodes (ISE). These electrodes are embedded in the concrete specimens and allow for continuous monitoring of chloride contents in the pore solution (free chlorides) [36,39,40]. Specifically, silver/silver chloride (Ag/AgCl) electrodes have previously proven effective when measuring the chloride ion activity in concrete using highly localized point measurements with an accuracy on the microscopic scale [39–41].

As it has been briefly described in this section, the movement of chlorides in concrete is irregular. Taking the effects that impact this phenomenon into account is possible, but requires more input data than what can be obtained with established approaches. Therefore, reliable and cost-effective characterization techniques must become more widely available. This becomes essential, in the case of the new trending construction technique of digitally fabricated concrete as described in the following section.

2.3. Spatial variability of chloride front and its importance in the new, trending field of digitally fabricated concrete

Chloride ingress in concrete is not homogeneous, and it does not lead to a uniform chloride front (see Figure 2.4). This can be attributed to differences in exposure conditions, or the innate heterogeneity of concrete, in particular the porosity difference between the binding cement paste and the aggregates [7]. However, the same phenomenon has been observed in laboratories where exposure and material are controlled. In literature, data has been reported mostly on a macroscopic scale [7,8,12]. Usually, the analyzed chloride content in concrete corresponds to the average chloride content in the sampled volume, and the spatial variability is not determinable or only poorly taken into account [7].
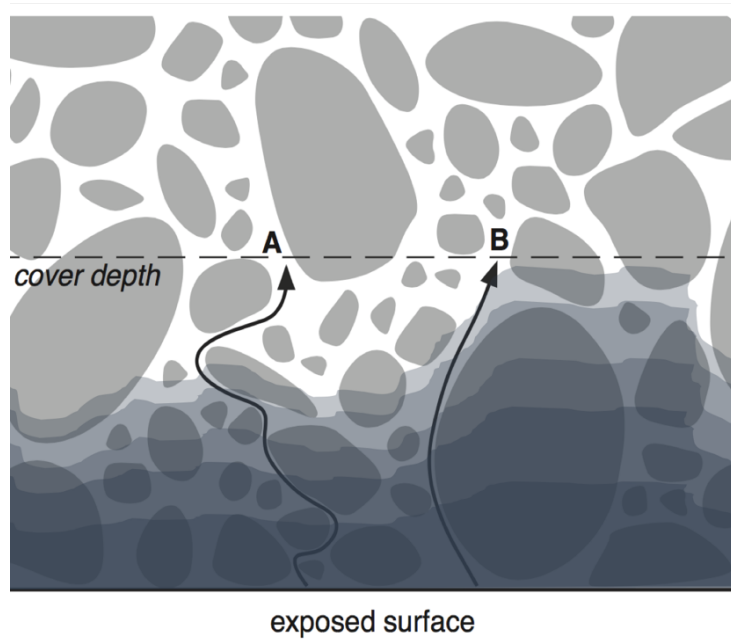
Figure 2.4: Schematic diagram that illustrates one of the factors that contribute to the variability in the chloride front; the effect of aggregates on the local transport in concrete. Line A indicates a long and tortuous pathway affected by the dense packing of smaller aggregates. Line B, represents the a path that is relatively short influenced by the local higher porosity, inherent of the interfacial transitions zones between the larger aggregates and the paste. The average chloride content determined in the layer closest to the end of the cover depth, might be misleading and even detrimental for a reinforced concrete structure (adapted from [7]).

With the increased popularity of digitally fabricated concrete, in particular 3D printing by layered extrusion, many researchers have embarked in research concerning these methods. Related research questions include material placement, cement hydration control and placement of reinforcement [42]. However there remains an important open question that needs to be addressed; the formation of cold joints between layers [42,43], that ultimately may compromise final structural performance and durability.

Cold joints occur between consecutively extruded layers that have limited intermixing [44]. It may happen if a critical resting time is exceeded. To illustrate this, the layered extrusion process is schematically shown in Figure 2.5. The

concrete has to be fluid enough to be extruded and to intermix with previous layers, but strong enough to hold its own weight plus the weight of the subsequent layers.
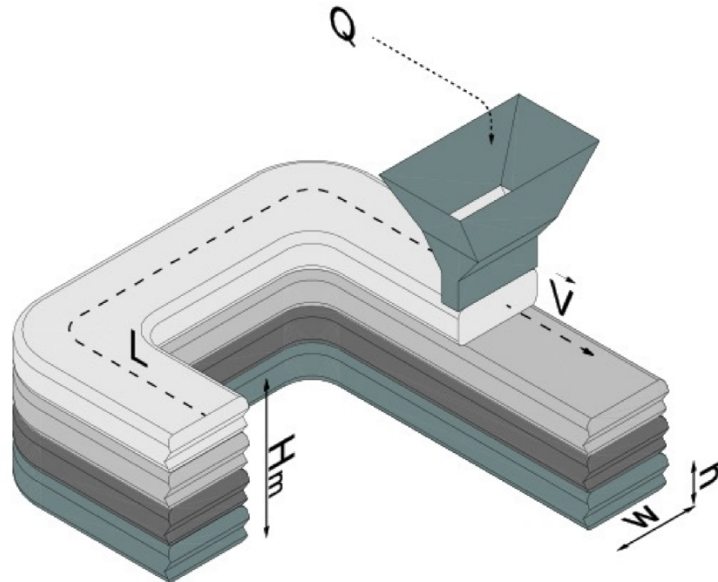
Figure 2.5: Schematic illustration of the layered extrusion process. A digitally controlled extrusion head moves at velocity V, placing layers of individual height h and width w. The overall height Hm depends on the velocity and the contour length L [42].

The formation of cold joints presents a favorable path for external substances to ingress the concrete. In terms of chloride ingress, this can be detrimental for cases where steel reinforcements are implemented, causing serious durability issues. If chlorides penetrate concrete through cold joints, conventional methods to determine chloride concentrations at different depths are limited use. Indeed chloride concentrations would be very inhomogeneous, so that the average chloride content over the slice volume would definitely be misleading. In this case, a high spatial resolution would be absolutely needed, specifically to know if chlorides are present much deeper in cold joints than in the bulk concrete. For

this, Micro XRF offers interesting perspectives. A more detailed description of this is given in the following section. The topic of chloride ingress through cold joints is further discussed in Chapter 5.

Part II: Background – data collection and processing

As described in Part I, having a spatial resolution of the quantified chlorides presents a significant advantage not only for the durability of "ordinary" reinforced, but also in the emerging field of digitally fabricated reinforced concrete. In both cases, we underlined the need for quantitative and high spatial resolution, which can be obtained by the chemical imaging of freshly split or cut samples using the micro analytical technique of micro- X-Ray Fluorescence. For a large part of this thesis, Support Vector Machines (SVMs) and the use of statistical learning theory for the quantification process were being implemented as a tool to quantify the chlorides in concrete using the entire X-ray fluorescence spectrum data. A potential advantage of this approach is a more robust quantification, although our results ultimately disproved the expectation. Despite this negative result, it was an important outcome of this thesis to demonstrate that, so that the principles of SVMs are presented in this chapter, whereas the results and discussions are presented in Chapter 3.

2.4. X-Ray Fluorescence

X ray fluorescence (XRF) is a useful technique for elemental analysis of materials, in that it is fast and all inclusive. In the decades after the X-rays were discovered by Röntgen in 1895, many developments were made in the field of X-ray spectrometry. Following the work of two of the pioneers of the XRF spectrometer, the first commercial X-ray fluorescence spectrometer was built in the late 1940s

[45,46]. Since the early 1950s, there has been an increasing use of X-rays in the field of materials characterization. And in the last few decades, XRF has become one of the most important tools in the analysis of materials [46,47]. Furthermore, its potential gave way to further developments to facilitate the characterization of inhomogeneous materials, which resulted in the micro XRF spectrometer [48]. Micro XRF gives access to the elemental composition of a sample on top of the related elemental spatial distribution. Micro XRF uses direct X-ray excitation to induce characteristic X-ray fluorescence emissions from the sample for elemental analysis, and uses X-ray optics to restrict the excitation beam size or focus the excitation beam to a small spot on the sample surface so that small features can be analyzed [47].

2.4.1. Principles of X-ray fluorescence

XRF spectrometry allows the identification of an element by measuring its characteristic X-ray emission wavelength or energy. When a bound atomic electron is struck by a high-energy particle- whose energy is greater than the binding energy of the atomic electron- it may be ejected from the atom with a kinetic energy, which is equivalent to the difference between the initial potential energy and the binding energy of the atomic electron [47]. This is referred to as the photoelectric effect (see Figure 2.6a). In other words, as an x-ray is absorbed by transferring all of its energy to the atom's innermost electron, they are ejected, creating vacancies. These vacancies present an unstable condition for the atom, and an electron from the outer shells falls into the inner shells giving off a characteristic X-ray (i.e. X-ray photon) in the process (Figure 2.6b). Because the energies of all emitted X-ray photons are proportional to the differences in the energy states of atomic electrons, the lines from a given element will be

characteristic of that element. This process gives rise to the characteristic lines in the X-ray emission spectrum (Figure 2.7) and allows the non-destructive measurement of a sample's elemental composition.
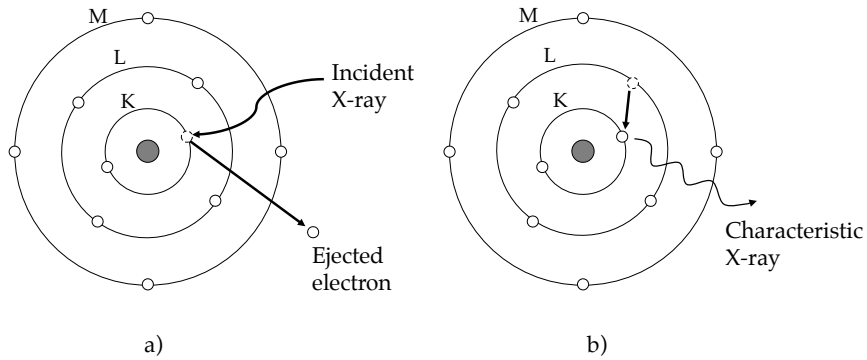
Figure 2.6: Simple sketch illustrating the photoelectric effect. a) An electron from the K line is ejected by incident X-rays. b) An electron from the L line falls into the K line, emitting a characteristic X-ray in the process.
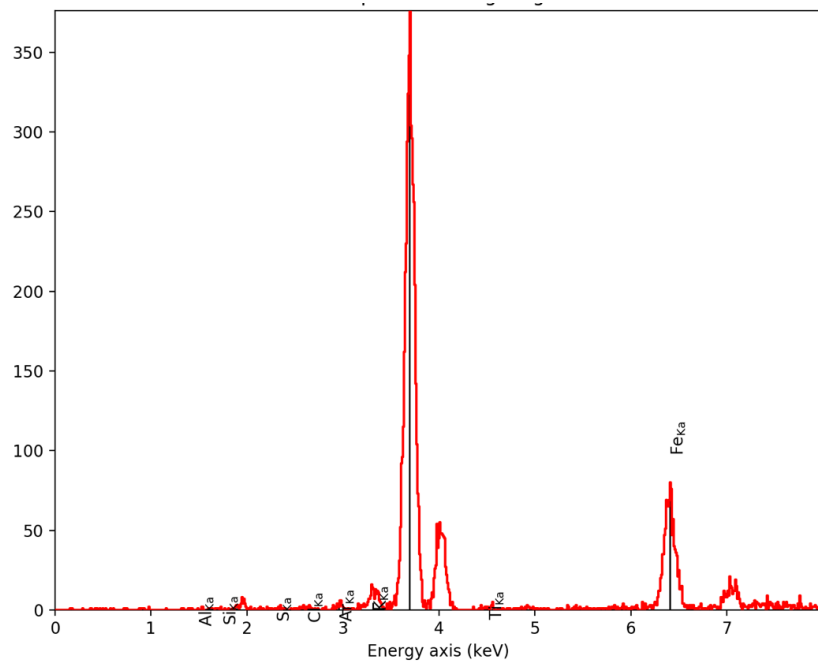
Figure 2.7: Typical spectrum of a cement paste sample. The y-axis represents the counts or intensity of the respective K lines.

2.4.2. Analytical precision and accuracy in X-ray Fluorescence Analysis

Like other analytical methods, quantitative X-ray fluorescence analysis is subject to both random and systematic errors that contribute to the accuracy of the analytical result [47,49]. When fluorescent X-rays are generated in a sample, these can be measured for quantitative analysis of the sample's constituent elements. Such analysis is fast, precise and nondestructive [50].

By understanding the source of errors, one can develop and improve an XRF analytical method. The high precision of X-ray spectrometry can only be translated into high accuracy if the various systematic errors are taken care of. A significant source of random errors is the X-ray source itself. Additionally, the line overlap may also introduce large random errors. And even though there are decent programs to deal with peak overlap and background noise, there are still some random errors introduced by the statistical limitations in counting [47,50].

The four main categories of errors encountered in XRF are summarized in Table 2.1. the first category deals with the sample to be measured. The largest potential error source in an XRF analysis is an inadequately prepared specimen [48,51–54]. A more detailed description of this error source is found later in this chapter. The second category corresponds to the instrument being used. The third category involves the counting process, which nowadays is usually carried out by the accompanying software. Finally, the fourth category deals with interelement effects.

Table 2.1: Main sources of random and systematic errors encountered in XRF analysis (adapted from[47]).

Source		Random error	Systematic error
1.	Sampling	x	-
	Sample preparation	x	x
	Sample inhomogeneity	-	x
2.	X-ray source	x	x
	Spectrometer	x	x
3.	Counting statistics	x	-
	Deadtime losses	-	x
4.	Primary absorption	-	x
	Secondary absorption	-	x
	Enhancement	-	x

In the conversion of net line intensity to analyte concentration, it is necessary to correct for any interactions that may occur. The intensity of an X-ray that propagates in a sample can be modified by matrix element effects, together with the generation of characteristic X-rays, absorption of the emitted X-rays along their paths, and the enhancement effect due to secondary excitation [47,55]. These physical phenomena have led to the derivation of practical and effective mathematical correction formulae. In this sense, the correction for matrix element effects is of great importance.

Assuming the specimen is homogeneous, these interelement effects fall into two categories, mainly absorption and enhancement effects. Absorption effects include primary and secondary absorption [47]. The first occurs because all atoms in the matrix will compete for the absorption of these primary photons. In other words, other matrix elements may modify the intensity distribution of the available photons. Secondary absorption occurs when the characteristic analyte radiation is absorbed by the specimen matrix. This absorption is relative to the mass absorption coefficients of the elements present in the matrix. Similarly, enhancement effects occur when a matrix element emits a characteristic line that has an energy that is high enough and close to the absorption edge of the analyte element. In other words, the non-analyte element is able to excite the analyte, adding characteristic photons to the ones already produced by the primary excitation [47,55,56].

2.4.3. Specimen preparation

As discussed in section 2.4.2, matrix effects are of significant concern when it comes to analyzing XRF data, and sample preparation has a big influence in how much these matrix effects will influence the results. Unless the specimen is properly prepared, it is difficult or even impossible to get accurate analytical data. Even if the XRF analysis can be short, more often than not the preparation of the samples is an overwhelming task.

XRF is a versatile analytical tool, for which the samples can be liquid, solid, or powder. Given the appropriate specimen preparation, large errors can be minimized. Sampling and specimen preparation errors can be orders of magnitude larger than any other error encountered during the analysis itself.

2.4.3.1. Solid specimens

In principle, the bulk composition of solid samples can be determined directly if the element distribution inside the solid specimen is homogeneous and the specimen shows a sufficiently flat surface [47,50,51]. Direct analysis of solid samples is possible; however, it presents a potential problem, in that local heterogeneity will not be representative of the total specimen. Moreover, the surface imperfections can also cause misinterpretations in the measurements of the bulk composition of the sample [47,51].

In literature [47,51,57], when referring to direct measurement on solid samples, one usually implicitly refers to the measurement on metallic samples. More often than not, when analyzing a solid sample known to be heterogeneous, the sample is prepared by grinding, followed by pressing or fusing into a pellet.

2.4.3.2. Powdered specimens

The preparation of powders and pellets is a common technique used for geological, industrial and biological materials [47,51]. The most common approach is to grind and then pelletize at high pressure, and in some cases, it is necessary to add an appropriate binder, such as a small amount of cellulose [47,50,51]. All things considered, the end goal of preparing a sample is to have a homogeneous material with a flat surface in order to minimize errors in the XRF measurement. Perhaps, the most efficient way to prepare a homogeneous sample is to use the borax fusion method [47,50,51,58]. It consists of the fusion of the sample with an excess of sodium or lithium tetraborate and casting it into a solid glass bead. The chemical reaction in the melt, converts the phases present in the samples into glass-like borates. This method produces a homogeneous bead or

pellet of which the dimensions can be controlled, making it a very efficient way of samples preparation. It is however, time consuming, and often expensive [59].

2.4.4. Quantitative analysis in X-ray fluorescence

The count rate of an analyte in a sample depends on various factors, such as weight fraction, matrix, type of specimen, sample preparation, and detection system, among others [47,50]. A commonly used theoretical method is the fundamental parameter (FP) method. Its name comes from the fact that it utilizes several basic physical parameters such as attenuation coefficients, transition probabilities, and fluorescent yields [50].The method has many roots in the works of different scientists [46,50],and it was Sherman [60–62] who laid the mathematical foundations for the FP method as it is used today. The FP algorithm is able to accurately correct matrix effects. Other commonly used methods are the theoretical influence coefficient methods, which are based on the classical set of FPs. The main time-consuming step is the computation of the influence coefficients, so once the sets of coefficients are precomputed, routine analysis is very fast [50].Currently, the FP method is included with the software supplied with each instrument.

Theoretical XRF intensities (i.e. photon count rate), can be calculated with the implementation of fundamental parameters. This is done in theory by taking into account the excitation conditions, geometry and absorption and enhancement (up to secondary fluorescence) by other elements in the sample matrix [63]. In XRF quantitative analysis, the concentration is proportional to the net measured intensity given the appropriate corrections [47,48,50,52,53]. Generally, the software supplied with the measuring instrument, consistently and properly corrects the measured net intensities for background and line overlaps.

The influence coefficients represent the relationship between count rates and concentrations in a way that directly shows the effect of the matrix on the count rates from the analyte element [50]. The general principle is that the ideal calibration curve is assumed to be linear, however it is nonlinear precisely because of the matrix effects. The experimental curve is linearized by applying corresponding counteracting corrections. The coefficients, which account for the extent of these (mathematical) corrections for each matrix element, are called empirical or theoretical influence coefficients, depending on the method of their determination [50]. There exist methods to calculate these coefficients, mainly based on the Sherman equation [47,50,52,53], but most of them are approximation designed for very specific applications.

Rousseau [50,52,53,64,65] proposed the fundamental algorithm (FA) to extend the FP method. The FA that is more universal and general. It is able to calculate the composition of heterogeneous samples. It was derived from the Sherman equation [52,60]. It considers direct and indirect (secondary) excitations, calculates influence coefficients, and separately takes into account matrix effects, absorption and enhancement. It can thus be considered as an extension to the Sherman equation [50]. A short summary of the approach is given in the following paragraphs.

The most general and basic expression used in XRF analysis for converting measured net intensities into concentrations is given by the so-called KIM equation (equation (2.1)) [52]

$$C_i = K_i \cdot I_i \cdot M_{is} \qquad (2.1)$$

Where C_i is concentration of the analyte i in the sample, K_i is the calibration factor, I_i is the measured net intensity of i, and M_{is} is the factor correcting the effect of the specimen matrix composition on the intensity of i.

For a pure element analyte, equation (2.1) becomes $1 = K_i \cdot I_{(i)} \cdot 1$, and combining this with equation (2.1) we get,

$$C_i = \frac{I_i}{I_{(i)}} * M_{is} \tag{2.2}$$

$\frac{I_i}{I_{(i)}}$ can be referred to as the relative intensity (R_i) where the nominator and denominator can change with each spectrometer, but their ratio will remain constant. This becomes useful in Rousseau's FA in which he defines C_i as,

$$C_i = R_i \frac{1 + \sum_j \alpha_{ij} C_j}{1 + \sum_j \varepsilon_{ij} C_j} \tag{2.3}$$

Where α_{ij} and ε_{ij} are the influence coefficients correcting for the absorption and enhancement, respectively. Equation (2.2) can be rewritten and divided by I_{iM}, the measured gross intensity of the analyte i in a drift monitor, which gives

$$\frac{I_i}{I_{iM}} = \frac{I_{(i)}}{I_{iM}} \cdot \frac{C_i}{M_{is}} \tag{2.4}$$

This gives an equation for a straight line with slope m_i given by $\frac{I_{(i)}}{I_{iM}}$. Rewriting equation (2.4) leads to

$$\frac{I_i}{I_{iM}} = m_i \cdot R_i \qquad\qquad (2.5)$$

This means that Rousseau's calibration procedure compares the measured relative intensity ($\frac{I_i}{I_{iM}}$) to the calculated one R_i. This trick allows the comparison of the relative intensities of any standard, independently of the matrix. In this way, the slope becomes a scaling factor that allows adapting the theory to the experimental data of an XRF spectrometer.

More frequently than not, as the motive for the development of the fundamental algorithm suggests, there is a high interest in characterizing the chemical composition of inhomogeneous materials such as geological samples or concrete. Therefore, to better characterize this kind of materials, spatial resolution is needed and this should be possible with by micro-X-ray fluorescence, which offers the additional advantage of being non-destructive, this also requiring limited effort in sample preparation.

2.4.5. Micro X-ray fluorescence

Micro X-ray fluorescence (μXRF) is an elemental analysis technique which allows for the examination of very small sample areas. Unlike conventional XRF, which has a typical spatial resolution ranging from several hundred micrometers up to several millimeters, μXRF uses polycapillary optics generate small focal spots with high X-ray flux on the sample surface with a spatial resolution on the micrometer scale (see Figure 2.8) [48,66,67].

In the last three decades, micro X Ray Fluorescence (micro- XRF) analysis has become more easily accessible for routine analysis. The selection of the incident beam energy is in the range of 15 kV to 40 kV, which provides the excitation of at least one measurable characteristic X-ray peak for all elements of the periodic table with an atomic number greater than 11 (sodium) in various media. The said spectra can be collected either in low vacuum or at atmospheric conditions. The method allows a high flux of photons, adjustable wavelengths and advanced X-ray focusing techniques, which are needed for high spatial resolution chemical imaging. The X-ray beam is excited using a rhodium (Rh) target, and this allows the detection of major and minor constituents of complex materials (e.g. cement paste) [66,67].

In this thesis, the instrument that was used for the micro XRF analysis is an EDAX (Mahwah, NJ, USA) ORBIS μ XRF spectrometer, for which the setup is illustrated in Figure 2.8. The system uses a Silicon Drift Detector (SDD) and focuses the X-rays from a rhodium target anode with a polycapillary focusing optic, which allows for a beam diameter of roughly 30 μm (FWHM at molybdenum Kα line, 17.5 keV). The SDD has an active area of 30 mm^2 and an 8 μm beryllium window with an energy resolution of less than 165 eV at manganese Kα line (5.9 keV). The acquisition system is the ORBIS Vision Software by EDAX.

1. Tube
2. Emergent X-rays
3. Polycapillary focusing optic
4. Incident X-rays
5. Sample
6. Emitted characteristic X-rays from sample
7. Si(Li) detector
8. Data analysis and collection
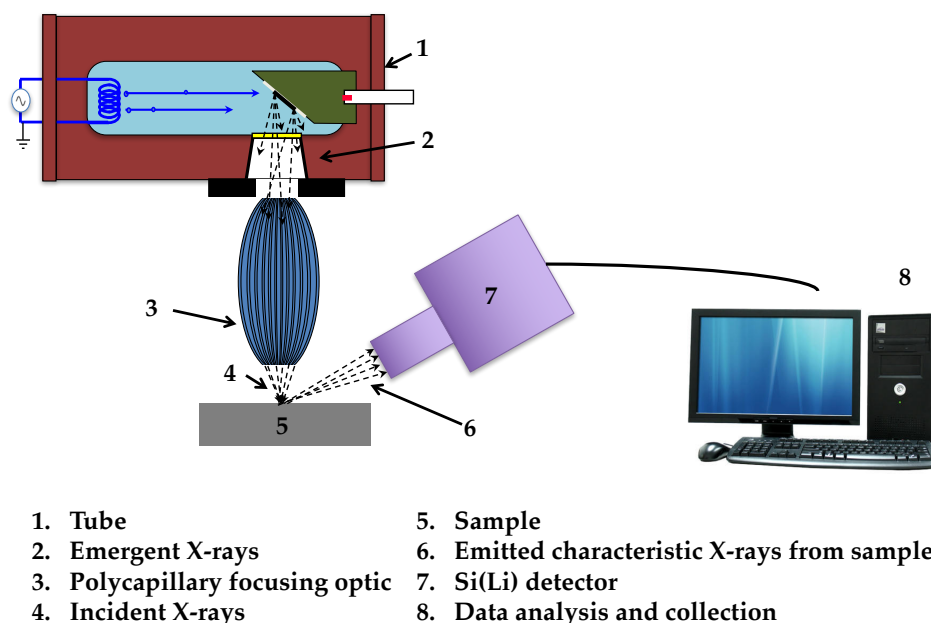
Figure 2.8: Simple schematic depicting the components of a micro XRF instrumentation.

The piezo-electric stage of the ORBIS micro XRF spectrometer allows for fast sample movements in the X and Y axes, and uses a stepper motor on the Z axis to handle large samples. The advantage of this design for benchtop micro XRF analyzers is that the X-ray beam is incident to the sample at a 90° angle (see Figure 2.8). This allows for an easier qualitative analysis that can be done beyond the designed working distance range of the instrument and for a broader range of sample geometries. Additionally, and more importantly for our study, it prevents shadowing of the X-ray beam, which represents an important limitation for samples that do not have a completely smooth surface [48,50,51].

*μ*XRF has been successfully used for applications including small feature evaluation, elemental mapping, film thickness measurement, evaluation of multi-layered coatings for advanced circuit boards, small particle analysis, and forensics [48,50].

2.5. Data processing using Support Vector Machines

The support vector machine (SVM) is a high-performance classification algorithm or a supervised learning model used in different fields of research. SVMs are learning systems that originated in Vapnik's statistical learning theory [68]. In other words, such systems learn from a set of data and predict an outcome based on that training data.

As SVMs were originally developed for classification purposes, the simplest way in which they can be used is for linearly separable binary classification. Linear learning machines are the simplest form of SVMs; however, they can efficiently perform non-linear classifications since they work with any number of dimensions as will be explained later in this section.

2.5.1. Linearly separable binary classification

Suppose one has a set of data points (training data) that lie in one of two classes. In short, the end goal of a support vector machine is to find the optimal hyperplane that divides the (in this case) linearly separable training data by maximizing the margin (See example in Figure 2.9) between both data sets. This allows it to predict or decide to which class a new point will belong to. The optimal margin is defined by the largest separation of the two classes.
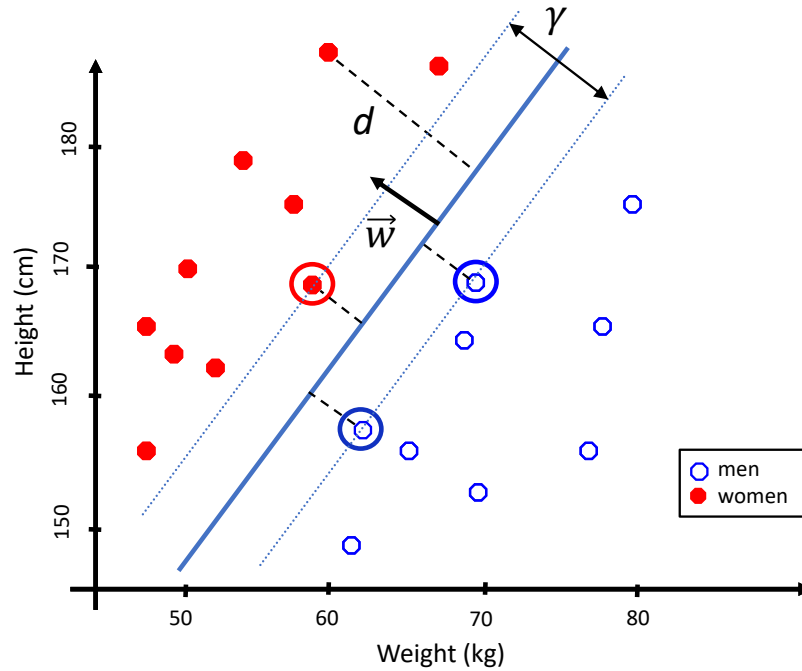
Figure 2.9: Binary classification example. A set of data points (training data) lie in one of two classes, men or women. Each data point contains information of the person's height and weight. The classes can be divided by a line (or hyperplane), or by an infinite number of hyperplanes. The hyperplane that has the maximum distance from the closest data point from each data set is shown in this Figure. The circled data points are the support vectors (adapted from [68]).

2.5.1.2. The mathematics

A real valued function $f : X \subseteq \mathbb{R}^D \to \mathbb{R}$ is typically used to perform binary classification. The input $\vec{x}_1, \dots, \vec{x}_n \in \mathbb{R}^D$ where each input $\vec{x}_i$ has D attributes and is assigned in one of two classes, y_j =-1 or +1. This allows us to define the training data as $\{\vec{x}_i, y_j\}$ where $i = 1, \dots, n$; $y_j \in \{-1, 1\}$ and $\vec{x}_i \in \mathbb{R}^D$ [69]. In the case where $f(\vec{x})$ is a linear function of $\vec{x} \in X$, one can write

$$f(\vec{x}) = \langle \vec{w} \cdot \vec{x} \rangle + b \tag{2.6}$$

$$= \sum_{i=1}^{n} w_i x_i + b$$

where $(\vec{w}, b) \in \mathbb{R}^D \times \mathbb{R}$ are the parameters that control the function, and the decision rule is given by the sign of $f(\vec{x})$. The sign of $f(\vec{x})$. will determine whether the vector belongs to class one or class two. The geometric interpretation of this hypothesis is that the input space X is split into two parts by a line (when $D = 2$, or by a hyperplane when $D > 2$) defined by the equation $\langle \vec{w} \cdot \vec{x} \rangle + b = 0$ (See Figure 2.9) [69]. The vector $\vec{w}$ defines the direction perpendicular to the hyperplane, and given this vector, the value of b moves the hyperplane parallel to itself.

The data points or the examples closest to hyperplane are the Support Vectors, and as was mentioned earlier the purpose of the SVMs is to position this hyperplane as far as possible form the closest examples of both classes [68].

Selecting the variables $\vec{w}$ and b requires to maximize the margin by means of the training set. In general, the training set can be described as

$$S = \left((\vec{x}_i, y_i), \dots, (\vec{x}_n, y_n) \right) \subseteq (X \times Y)^n \tag{2.7}$$

where X denotes the input space and Y denotes the output domain. Usually $X \subseteq \mathbb{R}^D$, whereas for binary classification $Y = \{-1, 1\}$, for m-class classification $Y = \{1, 2, \dots, m\}$, and for regression $Y \subseteq \mathbb{R}$ [69]. The functional margin of an example $(\vec{x}_i, y_i)$ with respect to a hyperplane $(\vec{w}, b)$ is defined by

$$\gamma_i = y_i(\langle \vec{w} \cdot \vec{x}_i \rangle + b) \tag{2.8}$$

Using equation (2.8), the training data can also be described by

$$y_i(\langle \vec{x}_i \cdot \vec{w} \rangle + b) - 1 \geq 0 \; \forall_i \tag{2.9}$$

Equation (2.9) gives the constraint for the optimal margin, which in other words means that no points (or data) shall lie within this margin. This information is useful in the calculations below. The optimization problem becomes:

$$maximize \; \gamma \quad such \; that \; y_i(\langle \vec{x}_i \cdot \vec{w} \rangle + b) - 1 \geq 0 \; \forall_i, \; and \; \|\vec{w}\| = 1 \tag{2.10}$$

The $\|\vec{w}\| = 1$ constraint ensures that the functional margin is also the geometric margin, thus the solution of this problem will result in $\vec{w}$ an b with the largest possible geometric margin with respect to the training set. However, solving this optimization problem with this constraint is difficult, since it is a non-convex problem, and it is not in a format that can be plugged into any standard optimization software.

Using vector geometry one can find that the distance from the hyperplane to the closest example. In other words, the margin is $1/\|\vec{w}\|$, and so maximizing the margin given the constraint $y_i(\langle \vec{x}_i \cdot \vec{w} \rangle + b) - 1 \geq 0 \; \forall_i$ is the same as minimizing $\|\vec{w}\|$. Another trick that can be used to make this problem simpler to solve is to consider that the variables $\vec{w}$ an b can be scaled without changing the geometric margin. With this, one can impose an arbitrary scaling constraint without

changing anything important. Working this into the problem above and noting that minimizing $\|\vec{w}\|$ is the same as minimizing $\|\vec{w}\|^2$, one can write [70]:

$$min \frac{1}{2}\|\vec{w}\|^2 \quad such\ that \quad y_i(\langle \vec{x}_i \cdot \vec{w}\rangle + b) - 1 \geq 0\ \forall_i \tag{2.11}$$

The use of Equation (2.11) makes it possible to efficiently solve this optimization problem since it takes a convex quadratic objective with only linear constraints [68]. This type of optimization problem is called a Quadratic Program.

In order to generalize the solution for the optimal margin, one has to consider the dual property of the optimization problem in question. To do so, the Primary Lagrangian formulation must be applied so as to accommodate for the inequality constraints in this minimization. The Lagrange multipliers $\alpha_i \geq 0\ \forall_i$, are allocated as follows:

$$\mathcal{L}_P(\vec{w}, b, \alpha) = \frac{1}{2}\|\vec{w}\|^2 - \sum_{i=1}^{n} \alpha_i[y_i(\vec{x}_i \cdot \vec{w} + b) - 1] \tag{2.12}$$

$\mathcal{L}_P$ needs to be minimized with respect to $\vec{w}$ and b and maximized with respect to α_i [68]. This is achieved by computing the partial derivatives with respect to $\vec{w}$ and b and setting them to zero:

$$\frac{\partial \mathcal{L}_P}{\partial \vec{w}} = 0 \implies \vec{w} = \sum_{i=1}^{n} \alpha_i y_i \vec{x}_i \tag{2.13}$$

$$\frac{\partial \mathcal{L}_P}{\partial b} = 0 \implies \sum_{i=1}^{n} \alpha_i y_i = 0 \tag{2.14}$$

By substitution, the new Lagrangian formulation becomes:

$$\mathcal{L}_D(\alpha) = \sum_{i=1}^{n} \alpha_i - \frac{1}{2} \sum_{i,j=1}^{n} y_i y_j \alpha_i \alpha_j \vec{x}_i \cdot \vec{x}_j \;\; s.t. \;\; \alpha_i \geq 0 \; \forall_i, \sum_{i=1}^{n} \alpha_i y_i = 0 \tag{2.15}$$

Equation (2.15) is referred to as the Dual form of the Primary Lagrangian, $\mathcal{L}_D$. It is now only dependent on α, and needs to be maximized. It is important to note that the Dual form requires only the calculation of the dot product of each input vector, and it does not explicitly depend on the dimensionality of the vector $\vec{x}$ [68,69]. This particularity will be crucial for the Kernel Trick, which allows for the construction of separating hyperplanes in high dimensional spaces, as described in the next subsection.

The already stated convex optimization problem can be solved by a Quadratic Programing solver, which returns the parameters α_i. Plugging these results in Equation 2.8 delivers the optimal vector $\vec{w}$. What remains is to solve for the intercept term b, which can be done by going back to the primary problem (Equation 2.6) and solving for b. In short, b is determined by finding the indices where $\alpha_i > 0$ (i.e. the Support Vectors, as α_i will be zero except for the SVs), and computing the dot product of the corresponding training vectors.

$$b = -\frac{1}{2}\left(max_{i:y_i=-1}\langle \vec{w} \cdot \vec{x}_i \rangle + min_{i:y_i=1}\langle \vec{w} \cdot \vec{x}_i \rangle\right) \qquad (2.16)$$

Significant insight has been gained by inspecting the dual form of the optimization problem. Moreover, it was possible to write the entire algorithm in terms of only inner dot products between input vectors. The variables $\vec{w}$ and b define the separating hyperplane's optimal orientation and hence this is the Support Vector Machine. In the next subsection, this dot product dependability is exploited in order to apply the kernels to a classification problem.

2.5.2. Nonlinear Support Vector Machines

On top of executing linear classification, SVMs can efficiently execute non-linear classifications using the kernel trick, which implicitly maps the input space X into a new higher dimensional feature space $H = \{\Phi(\vec{x})|\vec{x} \in X\}$ [69]. This is significantly helpful when the data is not linearly separable in the input space. The learning takes place in the feature space [71]. In other words, if a projection $\Phi: X \longmapsto H$ is used, the functions can be mapped into a higher dimensionality feature space by some non-linear mapping function $\Phi(\vec{x})$, where only inner products of the mapped vectors need to be determined (see example in Figure 2.10). This is computationally simpler than explicitly projecting $\vec{x}$ into the feature space H (i.e. without explicitly calculating Φ) and this trait is referred to as the Kernel Trick. The step is equivalent to $\vec{x} = (x_1, ..., x_n) \longmapsto \Phi(\vec{x}) = (\Phi_1(\vec{x}), ..., \Phi_N(\vec{x}))$, which will be further explored in the next part of this subsection.
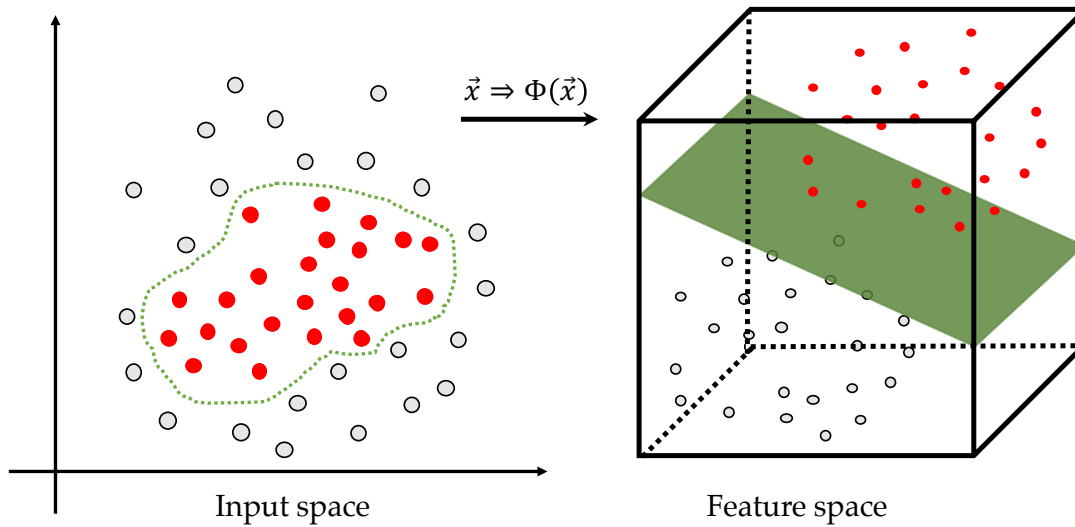
Figure 2.10: Kernel trick example. A Kernel is basically a similarity function, that is a real value function that quantifies the similarity between two objects. The input data is mapped into a feature space by the map Φ(x). This figure illustrates this graphically with one simple mapping from 2D to a 3D feature space. The data sets in the input space are not separable by a straight line, so the Kernel trick needs to be applied to make a simpler case and compute the SVM. The 2 classes need to be separated by a hyperplane. The input data sets are mapped into the new feature space, where the two classes can be separated by a hyperplane. In the case of a 3D space the hyperplane is a plane. Once the SVM is computed, it is possible to go back to the original data and work in the input space.

2.5.2.2. The Kernel Trick

A Kernel is basically a similarity function, that is a real value function that quantifies the similarity between two objects. Given the algorithm that was constructed earlier, and because it can be written entirely in terms of the inner products $\langle \vec{x}_i \cdot \vec{x}_j \rangle$, it is equivalent to writing it in terms of $\langle \Phi(\vec{x}_i) \cdot \Phi(\vec{x}_j) \rangle$. Specifically, given a feature mapping function Φ, the corresponding kernel is defined as

$$K(\vec{x}_i, \vec{x}_j) = \langle \Phi(\vec{x}_i) \cdot \Phi(\vec{x}_j) \rangle \qquad (2.17)$$

In this way, the SVM can learn in very high (even infinite) dimensions. As mentioned before, an important consequence to the dual representation that was worked out in the previous subsection, is that the dimension of the feature space does not affect the computation. As the feature vectors are not explicitly represented, the number of operations required to compute the inner product is not necessarily proportional to the number of features, i.e. computation is feasible regardless of the dimension of the feature space [69].

As an example, consider the following illustration, and recall that the feature map can be any linear transformation $\vec{x} \mapsto \vec{A}\vec{x}$, for some matrix $\vec{A}$, where the kernel function is given by $K(\vec{x}, \vec{z}) = \langle \vec{A}\vec{x} \cdot \vec{A}\vec{z} \rangle = \vec{x}'\vec{A}'\vec{A}\vec{z} = \vec{x}'\vec{B}\vec{z}$. Here, the construction $\vec{B} = \vec{A}'\vec{A}$ makes this a square symmetric positive semi definite matrix. A simple illustration of this example is the following nonlinear map:

$$\langle \vec{x} \cdot \vec{z} \rangle^2 = \left(\sum_{i=1}^{n} x_i z_i \right)^2 = \left(\sum_{i=1}^{n} x_i z_i \right) \left(\sum_{i=1}^{n} x_i z_i \right)$$

$$= \sum_{i=1}^{n} \sum_{j=1}^{n} x_i x_j z_i z_j = \sum_{i,j=1}^{n} (x_i x_j)(z_i z_j) \qquad (2.18)$$

which is equivalent to an inner product between the feature vectors

$$\Phi(\vec{x}) = \left(x_i x_j \right)_{i,j=1}^{n} \qquad (2.19)$$

43

Ultimately, the kernel trick is simply the option of computing the dot products in (very) high dimensional feature spaces, by using functions defined in pairs of input patterns. The trick allows the formulation of nonlinear variants of any algorithm that can be represented in terms of dot products [71].

Some of the commonly used kernels include:

. The linear kernel

$$K(\vec{x}, \vec{z}) = \langle \vec{x} \cdot \vec{z} \rangle \tag{2.20}$$

. The polynomial kernel

$$K(\vec{x}, \vec{z}) = (\langle \vec{x} \cdot \vec{z} \rangle + c)^d \tag{2.21}$$

. The Gaussian kernel

$$K(\vec{x}, \vec{z}) = exp\left(-\frac{\|\vec{x} - \vec{z}\|^2}{2\sigma^2}\right) \tag{2.22}$$

On the whole, support vector machines are a very useful tool for many applications. In a digital world, machine learning is becoming more and more useful and convenient for different applications (e.g. [72,73]). However, the perspective that the SVMs could offer in the field of concrete durability, was not as expected as it will be shown in the following chapter. The following chapter entails the said development of the method, and the results of the SVM are not

in line with the simpler case of a linear calibration line between net intensities

and chloride concentrations.

Chapter 3 - Method Development and Validation

Part of this chapter is based on a paper published in the Microchemical Journal:

"Standard and sample preparation for the micro XRF quantification of chlorides in hardened cement pastes"

By P. Bran-Anleu, F. Caruso, T. Wangler, E. Pomjakushina, R. J. Flatt [1]

3.1. Introduction

An important phase in the development of a reliable analytical procedure is sample preparation [74–77]. Homogeneity, a flat surface, and an appropriate thickness are a few aspects that must be considered to maximize the accuracy of X-ray fluorescence (XRF) measurements [48,51]. Although this is true for the conventional XRF technique, micro XRF offers the possibility to have minimal sample preparation, to measure in air, and – most importantly – to locally and non-destructively analyze areas over the surface of samples of up to 10 x 10 cm^2 [48,78]. Indeed, a quantitative analysis of any material requires a robust

procedure, especially if there is a large variety of elements present in the samples [52], as is the case for cement. Typically, samples to be analyzed are in the form of solids, powders, or fusion products, and the sample treatment can generally be kept to a minimum. However, in the case of inhomogeneous samples, such as geological or cementitious materials, the required preparation is usually more elaborate whilst trying to preserve the quickness and reproducibility of X-ray spectrometry analyses [48,51,52].

The largest potential error source in an XRF analysis is an inadequately prepared specimen [48,51,52,54]. Practice dictates that, for solid samples, there needs to be a sample preparation procedure that includes machining or polishing to obtain a flat surface [48]. The thickness of the surface layer that contributes to the signal will be determined by the absorption of fluorescence radiation in the matrix. This absorption depends both on energy of the radiation and on the matrix of the sample, and is referred to as the information depth. Hence, the surface structure has to be smaller than the information depth [48]. In practice, the lower the radiation energy, the stronger is the influence of the surface roughness, thus one of the most obvious sample preparation procedure is to fuse the sample into pellets. Micro XRF offers the option of direct measurements on as-is samples [54,79], and, accordingly, these effects have to be taken into account, for example, by choosing a surface that is as perpendicular as possible to the incident beam.

In the last three decades, micro XRF has become more easily accessible for routine analysis. The method allows a high flux of photons, adjustable wavelengths and advanced X-ray focusing techniques, which are all needed to achieve high spatial resolution chemical imaging [67]. Micro XRF gives access to the elemental composition of a sample in addition to the related elemental spatial distribution.

The X-ray optics restrict the excitation beam size to a small spot on the sample surface so that small features can be analyzed, enabling a high-resolution mapping of elements in samples. This is particularly important for the concrete and cement research as the technique may help improve the current knowledge regarding a reactive solute (e.g. chloride) and its transport mechanisms in heterogeneous, porous media [80]. Additionally, obtaining a high resolution chemical map is a significant application that can be implemented not only on concrete but on different building materials for which chloride ingress is a relevant issue. In materials such as stone, or earthen materials, salt crystallization plays a significant damaging role, and chloride distribution is an important factor [81].

This chapter presents the method development that enables using micro-XRF for the spatial and quantitative mapping of chlorides in cementitious materials. For the purpose of this method development, the calibration was done for cement paste, but it can be extended to concrete samples given that the cement paste can be singled out from the analyzed cross section. Additionally, the method was tested with a different water to cement ratio to assess the effect of matrix variability. It was also tested with a range of different cements including three blended cements in order to assess the method's performance concerning variable compositions. Moreover, samples with three different chloride contents were prepared for a validation analysis in support of this method. The proposed procedure can ultimately be faster than other established ones [25,33,38], and it facilitates a higher spatial distribution analysis and characterization of chlorides in concrete.

3.2. Experimental

3.2.1. Materials

A 25 kg-bag of fresh Portland cement (Normo 5R, certified CEM I 52.5 R, after Standard SN EN 197-1) (C1) provided by LafargeHolcim (LafargeHolcim Group Services Ltd/Holcim Technology Ltd, Zurich, Switzerland) was purposely stored in a barrel to prevent any change in composition due to possible hydration or carbonation. Portland cement was mixed with deionized water (conductivity of 3.5 ± 0.7 µS/cm) with a water-to-cement ratio (w/c) of 0.45 for the standards and samples with different cements, and a w/c of 0.60 for one set of samples to test the calibration curve against a different water-to-cement ratio. To stabilize the paste, a suspension of modified amorphous silica with an average size of 35 nm and a content of silica of 50% (w/w) was used (CEMbinder W8, AkzoNobel Specialty Chemicals, Moosleerau, Switzerland). Sodium chloride (NaCl for analysis EMSURE ®, ACS ISO, reag. Ph. Eur., Merck KGaA, Darmstadt, Germany), as chloride source, was added during mixing and had previously been weighed to the nearest mg.

The method was tested against different cements as well. For this, two commercial cements were used: a cement with a similar composition (Normo 4, certified CEM I 42.5 N, after Standard SN EN 197-1) (C2) provided by LafargeHolcim (LafargeHolcim Group Services Ltd/LafargeHolcim Technology Ltd, Zurich, Switzerland), and another CEM I (Jura, certified CEM I 52.5 R, after Standard SN EN 197-1) (C3) provided by Jura Cement (Jura-Cement-Fabriken AG, Wildegg, Switzerland). Table 3.1 shows the chemical composition of the cements and the amorphous colloidal silica.

Additionally, three blended cements were tested, namely B1, B2, and LC3. The blends were self-made, by substituting the OPC by fly ash and limestone in the case of B1 and B2. The fly ash was Hydrolent (LafargeHolcim) according to the European Standard EN 450 with a density of 2.2 g cm^{-3}. The limestone was also provided by LafargeHolcim. The chemical composition of the limestone and the fly ash used are shown in Table 3.1. LC3 was mixed based on the specifications of Limestone Calcined Clay Cements being investigated in the Laboratory of Construction Materials at EPFL, Switzerland in conjunction with the Physical Chemistry of Building Materials group at ETHZ, Switzerland [82]. Such cements contain a high clinker substitution and incorporates calcined clays. Half a kg of each blend was prepared, and they were blended using a Turbula (Turbula Shaker Mixer (ESKENS Tinting Solutions B.V., Netherlands)), for 26 hours. The proportions are presented in Table 3.2. Figure 3.1 summarizes the range of chemical compositions covered with the selected blended cements and supplementary cementitious materials by using a ternary diagram of SiO_2, Al_2O_3 an CaO content.

Table 3.1: Chemical composition of the cements, supplementary cementitious materials, and the amorphous silica used in the method development and application. The chemical composition was obtained by X-ray fluorescence. LOI = loss on ignition.

	Chemical composition (% (w/w))					
	C1	**C2**	**C3**	**Silica Suspension**	**Fly Ash**	**Limestone**
CaO	64.1	66.1	63.5	-	3.2	52.5
SiO_2	20.1	20.1	20.0	96.4	51.3	1.12
Al_2O_3	4.9	4.8	4.9	0.1	24.1	0.58
MgO	2.2	1.9	1.8	-	1.9	0.3
MnO	0.1	0.1	0.1	-	-	-
SO_3	2.2	*	3.2	*	0.3	0.01
Fe_2O_3	3.3	3.0	3.3	-	14.7	0.44
Na_2O	0.2	0.1	0.2	0.5	0.97	0.01
K_2O	0.9	1.0	0.7	-	2.79	0.04
TiO_2	0.4	0.3	0.3	-	-	-
P_2O_5	0.3	0.2	0.2	-	0.33	0.01
LOI	1.6	2.2	2.0	2.4	NA	NA
Sum	100.3	99.8	100.2	99.4	99.6	55.0

* SO_3 is not quantifiable by the method used. NA = Data not available.

Table 3.2: Proportions of blended cements shown in mass percentages.

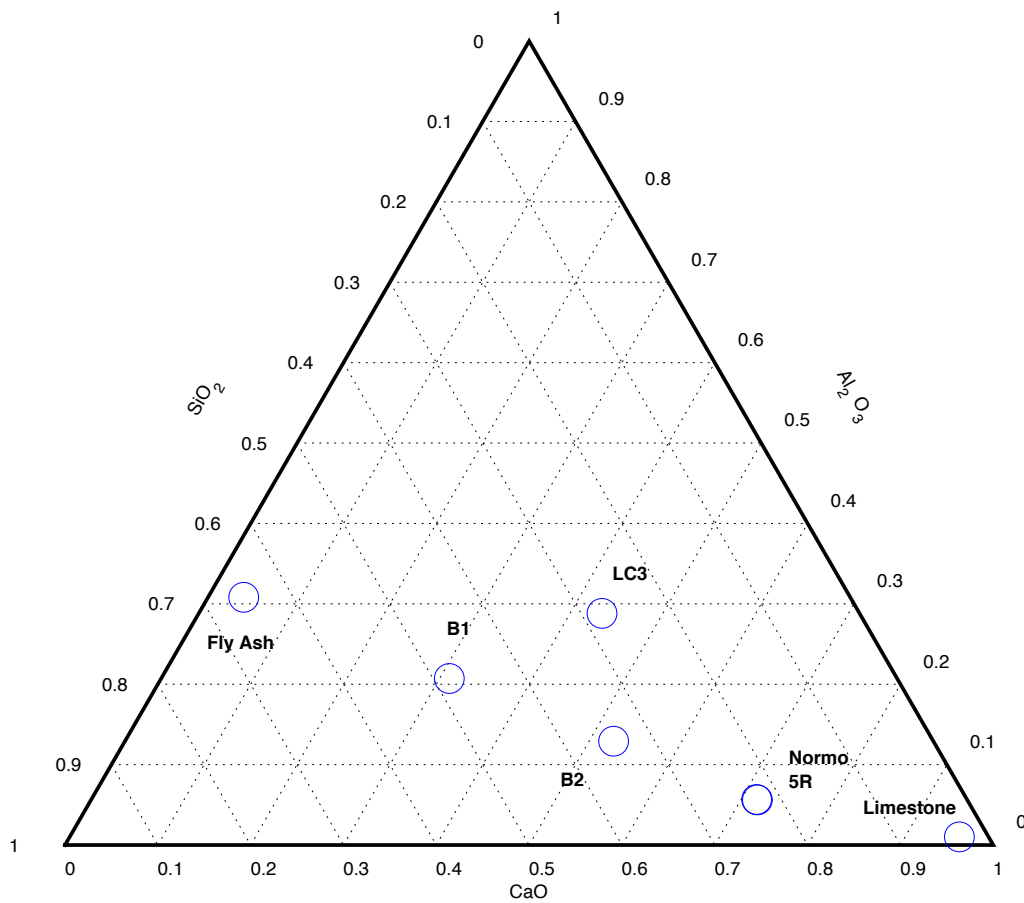| Proportions of blended cements (%)					
Blend	**CEM I**	**Limestone**	**Fly Ash**	**Gypsum**	**Calcined Clay**
B1	40	-	60	-	-
B2	65	5	30	-	-
LC3	54	15	-	2	29

Figure 3.1: Ternary plot depicting the three main oxide contents (SiO$_2$, CaO, Al$_2$O$_3$) of the blended cements, where the three variables are conveniently mapped.

3.2.2. Standard and sample preparation

Cement paste standards with known chloride content were used for the calibration. These standards were produced in the laboratory to match the matrix of the samples ultimately intended to be used. The scattering effect strongly depends on the composition of the sample [50]. Therefore, standards were made with accurately known contents of chloride. Additionally, as photon count rates are distinct functions of the matrix [50], the same composition was used for both the standards and the samples for statistical analysis.

The content of amorphous silica suspension was chosen after testing the paste with different dosages to have a good compromise between bleeding[1] prevention and workability[2] of the paste. The ratio of amorphous silica to cement of 1:10 gives an adequate value for the purposes of making the cement paste standards and the samples containing the Normo 4 and Jura cements. In the case of the blended cements, the ratio that had been used proved to be too high, as the workability of the pastes were compromised. For this reason, the pastes were tested with different contents of nano silica to find the best compromise. The nano silica to cement ratios were chosen to be 1:100 and 1:20 for the LC3 and the B cements, respectively. The water content of the mix was appropriately corrected considering the amount present in the amorphous silica suspension.

---

[1] Bleeding is a term that refers to the gravity driven consolidation of particles and the migration of water to the top of a mould after fresh concrete (or cement paste) has been cast. It influences the long-term permeability and strength of concrete [83].

[2] Workability is a term that refers to the property of a fresh concrete to be more or less easily placed or cast [83].

Chloride content values were chosen so that its determination was within a range that represents the chloride threshold values for pitting corrosion initiation in reinforced concrete, as reviewed by Angst et al. [4].The chloride content values for the calibration are 0.1, 0.4, 0.5, 0.6, 0.75, 1.0, 1.5, and 2.0% by mass of cement. The chloride content of the samples for the rest of the analyses, are discussed in the 'Results and Discussion' section.

The mixing procedure for all samples prepared for this chapter, was as follows. The different components were weighed separately with as much accuracy as possible. The cement, the water and the colloidal silica were weighed to the nearest tenth of a gram, and the sodium chloride was weighed to the nearest mg. The dry components (cement and sodium chloride) were thoroughly mixed by hand for 1 minute in a clean PE container using a clean spatula. A mixture of water and amorphous silica suspension was then slowly added to the dry components and mixed at a speed of 500 rpm for 2 minutes using a IKA Eurostar power-b mixer (IKA-Werke GmbH & Co. KG, Staufen, Germany). After that, the mixed paste was left to rest for 2 to 3 minutes, and then the mixing continued for another 2 to 3 minutes at a speed of 1100 rpm. The fresh cement paste was cast in 75 cm^3, sealed plastic cylinders that were kept in a climatic room at 95% RH for at least 28 days to allow curing of cement without any leaching of the chlorides. After the curing time, the samples were split by applying a force along the longitudinal side of the cylinder as in a splitting test also known as Brazilian test. This was done the morning before the micro XRF measurements were performed on the relatively fresh fractured surface. Other cements, and blended cement samples were prepared in the exact same way as the standards.

3.2.3. Instrumentation

The instrument used for the micro XRF analysis is an EDAX (Mahwah, NJ, USA) ORBIS µ XRF spectrometer. A more detailed description of the instrument can be found in Chapter 2, section 2.4.5.

3.2.3.1. Detectors

A very important point that needs to be addressed is the fact that during this thesis, the detector in the XRF spectrometer had to be sent for repairs, and a replacement detector was installed in its place. This had an impact on the calibration curves and is something that is important to keep track of. Thus, for the rest of the thesis, the detectors will be referred to as D1 for the starting detector, and D2 for the replacement.

3.2.3.2. Measurement protocol

The final measurement protocol for the standards was the following: The relatively fresh split surfaces of the samples were measured in a 2.5×2.5 mm^2 area using a matrix of 15×15 points. The size of the area represents the distance over which the cumulative average of the measured chloride content becomes stable. This was assessed by measuring consecutive points in a line scan on several samples and calculating the cumulative average, which stabilized on average at 2.5 mm. The area was cautiously chosen in the middle of the samples on a reasonably flat surface. The applied acceleration potential and current were 35 kV and 950 µA, respectively. At each point, a spectrum was acquired for 30 s ($26\% \pm 1\%$ dead time). Measurements were carried out in air with a built-in 25-µm thick aluminum filter to eliminate the rhodium Lα radiation and, therefore,

preventing it from reaching the sample. This is necessary because this radiation overlaps with the chlorine Kα X-ray line and increases its limit of detection.

3.2.4. Method Validation

The method was validated using 3 reference sets, and 4 independently prepared blanks that were created and measured under the same conditions as the standards. (performed using detector D2.) The reference set correspond to samples with known chloride content that are not used for calibration, and the blanks are samples that do not contain any chlorides. The chosen chloride concentrations were within the calibration range: between 0.3 and 1.3 % (w/w) of cement. Each set consists of 8 independently prepared samples.

We evaluated parameters associated with the following analytical characteristics: i) calibration; ii) limit of detection (LOD) and limit of quantification (LOQ); and iii) trueness and precision. Trueness represents the agreement between the analytical result of a reference material, when applying the method, and the accepted value [49,84]. Trueness can be expressed as a measure of closeness of agreement [85]. Precision can be expressed as a measure of the standard deviation [86].

As a way of comparison and corroboration, additional measurements were planned to compare our method with what is used in practice. For this purpose, three samples of each chloride content of the reference sets were chosen to be measured in a different laboratory using a certified method readily used in practice. That laboratory (TFB AG; Wildegg, Switzerland) implements the ISO standard for chemical analysis in cement with XRF [38], in which samples are grinded, and fused into pellets in preparation for the measurements.

In this case, the results are expressed as a mass percentage with respect to ground powder, which includes water bound in the crystal structure of the cement hydrates, but not unbound water that is lost during the drying step of the sample preparation. With this in mind, the mass of the anhydrous cement corresponding to the dried powder of the samples measured at TFB needed to be determined. The samples were ground and preconditioned at 105°C for one day to remove physically adsorbed water, after which the amount of bound water was estimated via thermogravimetric analysis (TGA). The TGA weight-loss measurements were made from room temperature to 1000°C at a heating rate of 10°C/min. The XRF results were corrected accordingly, and subsequently compared to our measurements using a paired t-test to assess if there is a significant difference in the two methods. The paired t test looks at the difference between each pair of results given by two methods on the same set of samples [49].

3.2.5. Support Vector Machines

As explained in Chapter 2, there are different possible procedures for data analysis. One of these involves the use of Support Vector Machines (SVMs) that theoretically could offer a more robust and reliable results.

Implementations of SVMs are available in almost every popular programming language, since SVMs are among the most popular and efficient classification methods available today [87]. A detailed description of what SVMs is given in Chapter 2, section 2.5. The presently described method uses the language R [88] which implements SVMs via the kernlab package. The kernel used was the polynomial kernel (equation (2.21), see Chapter 2, section 2.5.2).

$$K(\vec{x}, \vec{z}) = (scale\langle \vec{x} \cdot \vec{z} \rangle + offset)^{degree} \tag{3.1}$$

where *degree* is a positive integer that stands for the degree of the polynomial, *scale* is the scaling parameter which is convenient for normalizing patterns without the need to modify the data itself, and *offset* is the offset used in the polynomial function.

The *degree*, *scale* and *offset* were chosen as 1, 1 and 0 respectively. Some additional parameters required in the code include the type of formulation (eps-svr: epsilon regression), with an epsilon (insensitive-loss function) value of 0.1, and the constant of the regularization term in the Lagrange formulation C, which was chosen as 1. These values were chosen using the cross validation function (trial and error) within the kernlab function in R. The goal is to get as few support vectors as possible. Of course, there is a systematic way to do this, which consists on manually doing the cross validation, but due to time constraints and limited knowledge of the filed, this was done automatically using the option in R.

3.3. Results and discussion

3.3.1. Calibration curve for D1

The net count rates, or net intensities, for chloride were calculated with the ORBIS Vision software built-in calculator in which the background is subtracted, and the spectrum is deconvoluted. The resulting least squares regression equation calculated from the measurements is:

$$I_{Cl} = 33.13\ C_{Cl,\ w/w} + 1.79 \tag{3.2}$$

where I_{Cl} is the mean value of the calculated net intensities for chloride expressed in counts per second, and $C_{Cl,\ w/w}$ is the concentration of the sample in percentage by mass of cement. The calibration line is presented in Figure 3.2.

Possible outliers were checked using Cook's squared distance, which measures the effect of omitting a calibration point on the regression coefficients [49]. No data was omitted.
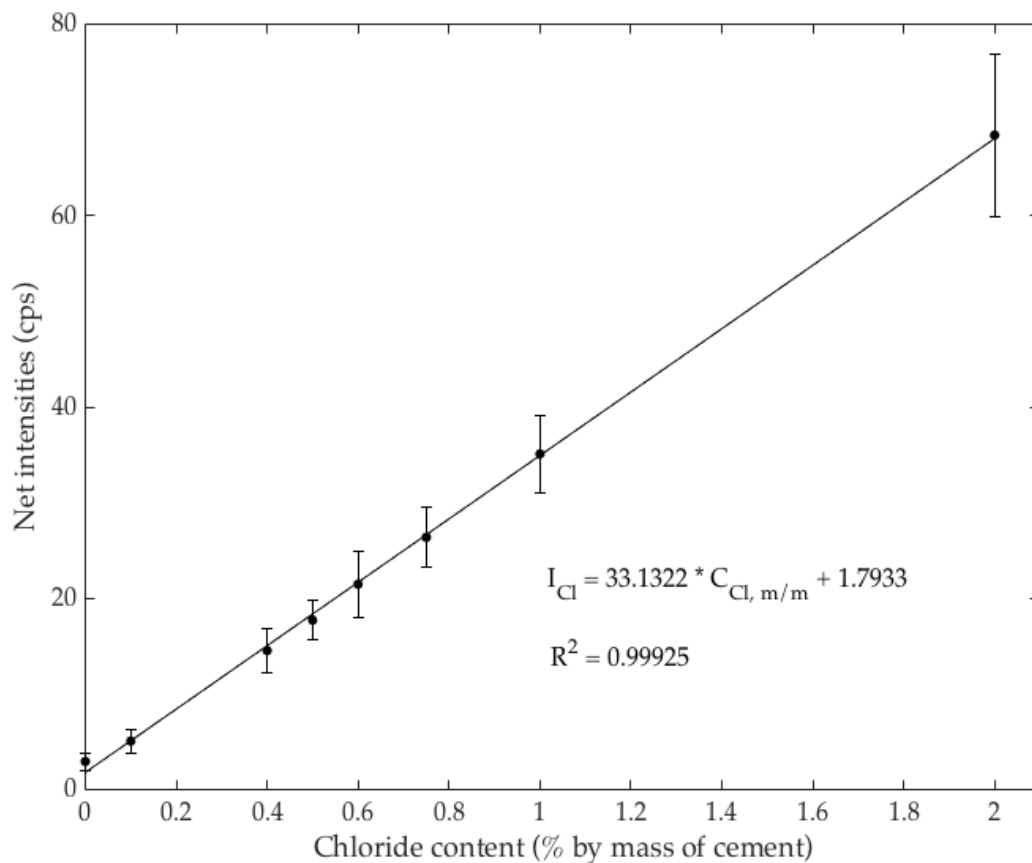

Figure 3.2: Calibration line for D1. Intensities as a function of chloride dosage by volume of cement paste. The results are presented as the mean values and the standard deviations. Standard deviations for the dosed chloride contents result only from sample preparation. They are too small to be displayed in this figure.

3.3.2. Calibration curve for D2

The net count rates, or net intensities, for chloride were calculated with the ORBIS Vision software built-in calculator in which the background is subtracted, and the spectrum is deconvoluted. The resulting least squares regression equation calculated from the measurements is:

$$I_{Cl} = 62.63 \; C_{Cl, \, w/w} + 0.22 \tag{3.3}$$

where I_{Cl} is the mean value of the calculated net intensities for chloride expressed in counts per second, and $C_{Cl, \, w/w}$ is the concentration of the sample in percentage by mass of cement. The calibration line is presented in Figure 3.3. As expected the calibration constants are detector dependent, so that values reported here cannot be used on other instruments directly. An instrument specific calibration is always needed. However, a linear response appears to be a characteristic feature in this chloride concentration range.

Possible outliers were checked using Cook's squared distance, which measures the effect of omitting a calibration point on the regression coefficients [49]. No data was omitted.
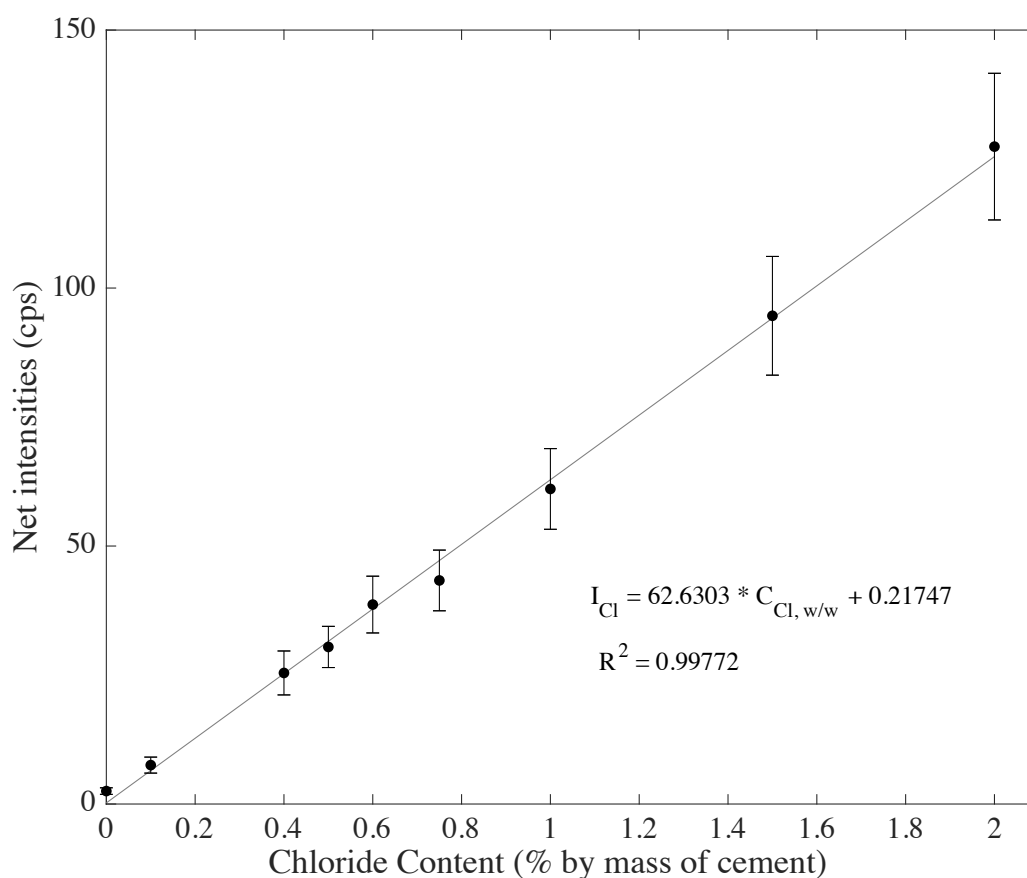
Figure 3.3 Calibration line for D2. Intensities as a function of chloride dosage by volume of cement paste. The results are presented as the mean values and the standard deviations. Standard deviations for the dosed chloride contents result only from sample preparation. They are too small to be displayed in this figure.

3.3.3. Limits of detection and quantification

The working limit of detection (LOD) and quantification (LOQ) of chloride were calculated respectively as three and ten times the standard deviation of the mean chloride concentrations of four independently prepared blanks [49]. The measurements and quantifications were performed the same way as with the standards (see section 3.2). Of course, the limits of detection and quantification are also affected by the use of different detectors. The method LOD is 0.009%

(w/w) of cement and the LOQ is 0.028% (w/w) of cement for detector D1. The method LOD is 0.003% (w/w) of cement and the LOQ is 0.011% (w/w) of cement for detector D2.

The chloride content threshold for pitting corrosion initiation in reinforced concrete is reported in literature to range between about 0.4% and 0.7% [4,5]. Researchers have not yet come to an agreement on a single critical chloride content, most probably because there is no single value since it should vary with different factors, including the state of the steel rebar surface and the carbonation degree of concrete [2]. Despite this and from a pragmatic point of view, we can state that chlorides contents of at least 0.4% ought to be detectable by any method intended to be used to study chloride induced corrosion.

Taking this into account, our approach with micro XRF is a suitable method. The method can detect contents of chloride – at least – 100 times lower than the above-mentioned thresholds. This makes our approach a very sensitive one for laboratory monitoring of chloride contents close to the reinforcement in concrete. In particular, it offers the needed resolution to establish diffusion fronts of chlorides, with a good resolution in the low concentration range, something important for accurately predicting the evolution of chloride ingress.

3.3.4. Method performance

Prior to analyzing the reference sets, calibration was carried out with standards, as described above. Each sample in the three reference sets was analyzed using the same procedure as the standards. Using the regression equation (Equation (3.2)) shown in section 3.3.1, the content of chloride in the eight replicate samples

were calculated. Figure 3.4 shows a 1:1 comparison of the expected concentration values versus the calculated concentrations.
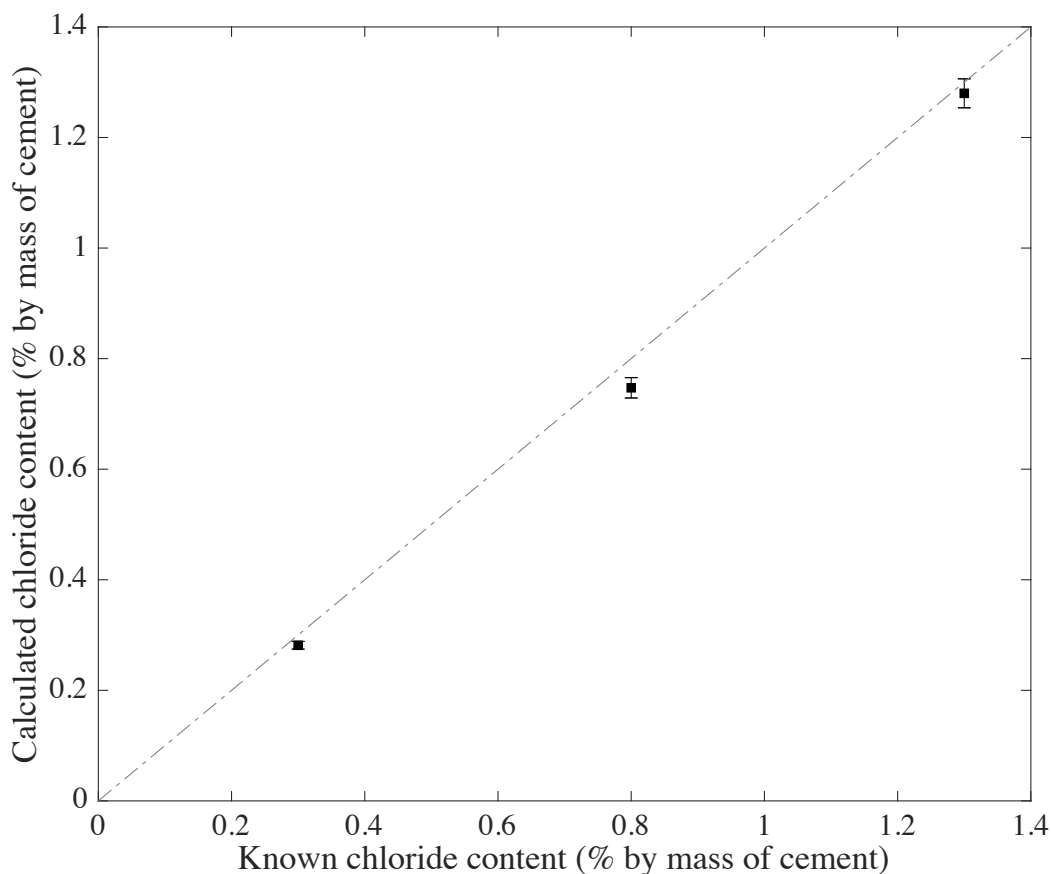

Figure 3.4: Expected contents versus the calculated contents. The dashed 1:1 line is included for reference. The results are presented as the mean value for each set (squares), and the standard error of the mean at the 95% confidence limit, $n_{samples}$ = 8. Suspected outlying values were checked with and passed the ISO-recommended Grubbs' test with P = 0.05 [49]

To compare the calculated chloride contents against known values, the closeness of agreement for each sample in each reference set was calculated. Figure 3.5 illustrates said values as box plots. The box plot for the reference set with 0.3% (w/w) chloride content shows that many samples in the set have similar relative errors, but in others the errors are more variable. The long upper whisker means

that relative errors are varied amongst the higher quartile group, and very similar for the lower quartile group. These data together with the box plots for the other two sets suggest that the errors are independent of the concentration, and thus, these are random and not systematic errors.
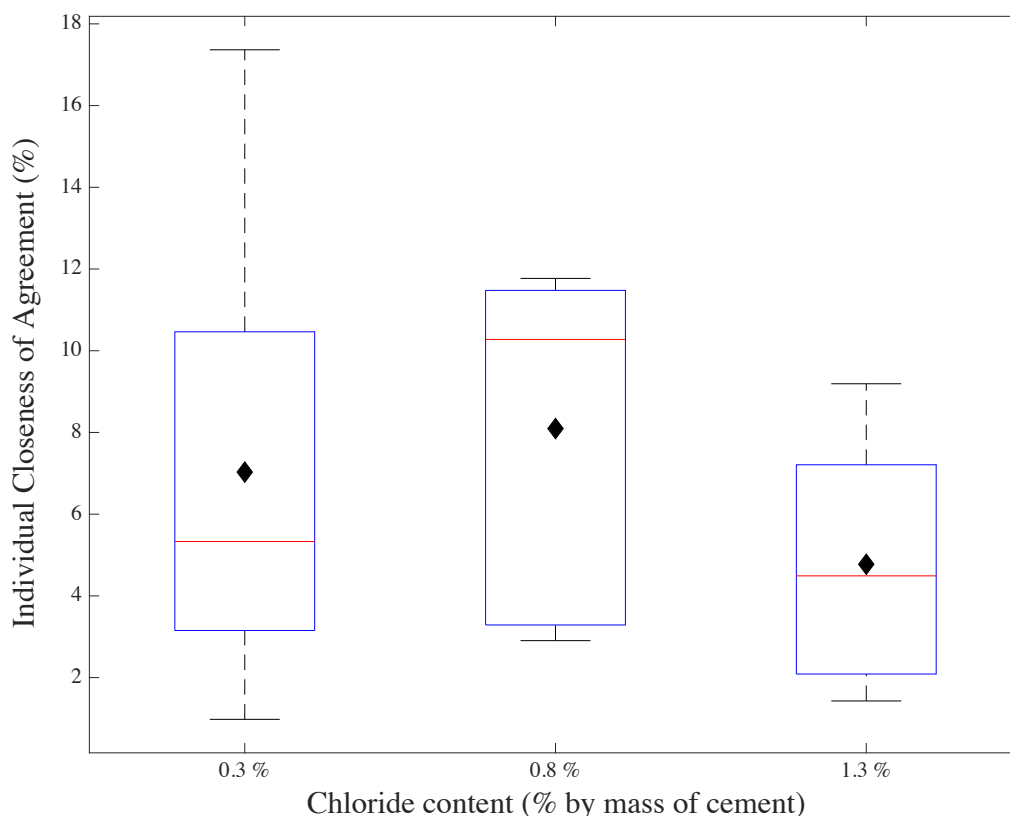
Figure 3.5: Individual closeness of agreement shown as a boxplot for each reference set. The central rectangles span the first quartile to the third quartile. The segment inside the rectangle shows the median and the "whiskers" above and below the box show the locations of the minimum and maximum values, respectively. The black diamonds represent the mean. Suspected outlying values were checked with and passed the ISO-recommended Grubbs' test with P = 0.05 [49].

The trueness of our method was evaluated as the mean of the absolute percentage deviation of our measurements from the real concentration of eight repetitions of independently prepared reference samples with three different chloride

concentrations. The measures of closeness of agreement for each concentration are shown in Table 3.3.

Table 3.3: Measures of closeness of agreement obtained with our method for the chosen concentrations. The value was computed as the mean (the measurement of the reference samples was repeated on eight samples) of the percentage deviation from the real concentration values.

Chloride content (% (w/w))	Closeness of agreement
0.3	6.2%
0.8	6.6%
1.3	1.5%

The results for the closeness of agreement, correspond with what is shown in Figure 3.5, where the method's performance when applied on the set corresponding to 0.8% (w/w) chloride content performs slightly poorer than for the other two content values. The values of closeness of agreement obtained with our method are comparable to the required values according to the international standard (ISO) for chemical analysis with XRF [38]. The vast difference between our method and the ISO method needs to be stressed in that the measurements are performed on completely different matrices. However, we obtain comparable values of closeness of agreement. These data further indicate an adequate method performance.

3.3.5. Comparison with established quantification technique used in practice

As already discussed, our results are comparable with other methods in terms of limits of detection and quantification, but also in terms of closeness of agreement. After the appropriate corrections were made, the chloride contents obtained from TFB did not significantly differ from the results obtained with our method. As a reminder, this correction was done because TFB data are reported with respect to a dry hydrated sample, while ours use the mass of the starting sample. The conversion of 1.30 used TGA data and does not involved any fitting parameter. The results both before and after correction are summarized in Table 3.4

The good agreement between both methods was confirmed with the results of a paired t-test that was performed on each set (of 3). In brief, the two methods do not differ significantly at $P = 0.10$ (t=2.92, n=3).

TFB's calibration range is targeted to concrete samples, and given that our samples are cement paste, it is evident that our contents are higher than what they usually expect and measure. Thus, some of our samples were far out of their working calibration range, and so their results were affected by a $20 - 30\%$ error. Indeed, some of the values we chose for our calibration are higher than the ones one considers the realistic chloride contents an actual structure may contain. However, critical chloride values (for corrosion initiation) have been reported to be up to 2% by binder in some cases [4].

Table 3.4: Comparison of chloride contents obtained with our method for the chosen concentrations and the values obtained with a different method. The critical t-values are given for the paired t-test (n=3).

| Sample | t-value | Chloride Content (% (w/w)) | | | |
		Known	μ-XRF	XRF	XRF (corrected)
R3S02		0.3	0.27	0.227	0.294
R3S03	2.26	0.3	0.30	0.233	0.302
R3S05		0.3	0.26	0.230	0.298
R8S01		0.8	0.82	0.576	0.767
R8S02	0.55	0.8	0.71	0.578	0.749
R8S04		0.8	0.77	0.579	0.750
R13S01		1.3	1.37	0.905	1.173
R13S07	2.58	1.3	1.23	0.915	1.186
R13S08		1.3	1.32	0.932	1.208

3.3.6. Method performance with a different w/c

In order to compare the method's performance with a different w/c, but using the same calibration curve, the following facts must be taken into consideration.

What the XRF truly measures is a chloride count in a given surface area. This chloride count is proportional to the chloride dosage with respect to cement and to the surface fraction of cement in any cross section.

For random heterogeneous materials, the surface area fraction of a phase in a cross section is equal to the volume fraction of that phase in a sample volume. Thus, chloride count should be proportional to the chloride dosage and to the volume fraction of cement in the sample. So, the determined chloride content, using a calibration curve established for a first water to cement ratio WC_1 has to be corrected by the ratio of cement volume fractions as follows:

$$\frac{\emptyset_1}{\emptyset_2} = \frac{\dfrac{1/\rho_C}{\dfrac{1}{\rho_C} + WC_1 + \dfrac{c_{s1}}{100 \cdot \rho_S}}}{\dfrac{1/\rho_C}{\dfrac{1}{\rho_C} + WC_2 + \dfrac{c_{s2}}{100 \cdot \rho_S}}} = \frac{1/\rho_C + WC_2 + \dfrac{c_{s2}}{100 \cdot \rho_S}}{1/\rho_C + WC_1 + \dfrac{c_{s1}}{100 \cdot \rho_S}} \qquad (3.4)$$

to obtain the concentration of chloride by mass of cement in a sample with another water to cement ratio WC_2. Where ρ_C, ρ_S, c_{s1} are the density of cement, density if silicon oxide, and the dosage of Cem Binder in percentage.

The above equation corresponds to the ratio of the volumes of samples containing each one gram of cement. In the specific cases considered here, the two w/b used were 0.41, and 0.55, giving for 1 g of cement paste volumes of 0.76, and 0.90 cm^3, respectively. The samples used to examine the effect of w/c contained the following chloride contents, 0.1, 0.15, 0.4, 0.6, 1, and 2 % by mass of cement.

After the above-mentioned conversion, we determined the closeness of agreement for each sample. As shown in Figure 3.6, for lower chloride contents, the method performs well and is comparable to the closeness of agreements obtained in section 3.3.4, Table 3.3. However, higher chloride contents give closeness of agreements as high as about 40%. In general, this means that the technique is not very accurate, as can be clearly seen in Figure 3.7. This can be attributed to the higher porosity in a paste due to a higher water to binder ratio. Because of this, more moisture is available in the pores, and the higher chloride content allows for more free chlorides in the pore solution. Another contributor to the error is the matrix effect. As was mentioned in Chapter 2, the matrix will strongly influence the XRF results, and these results are evidence of this influence.
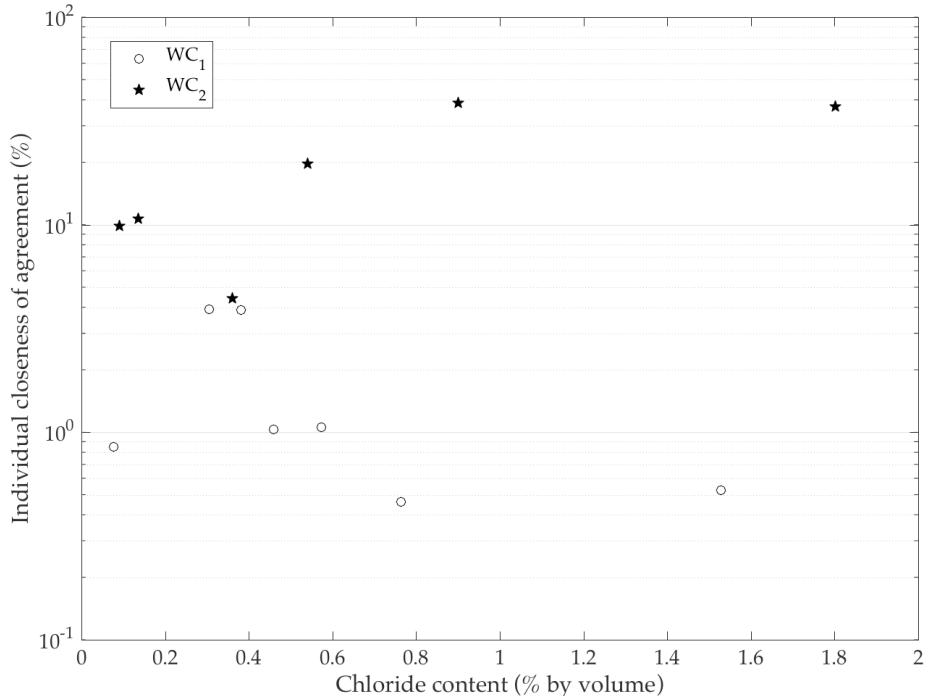

Figure 3.6: Individual closeness of agreement for each sample with a w/b of 0.55. Chloride contents were calculated using calibration line D1, after appropriately correcting for the volume of 1 g of cement in the paste.
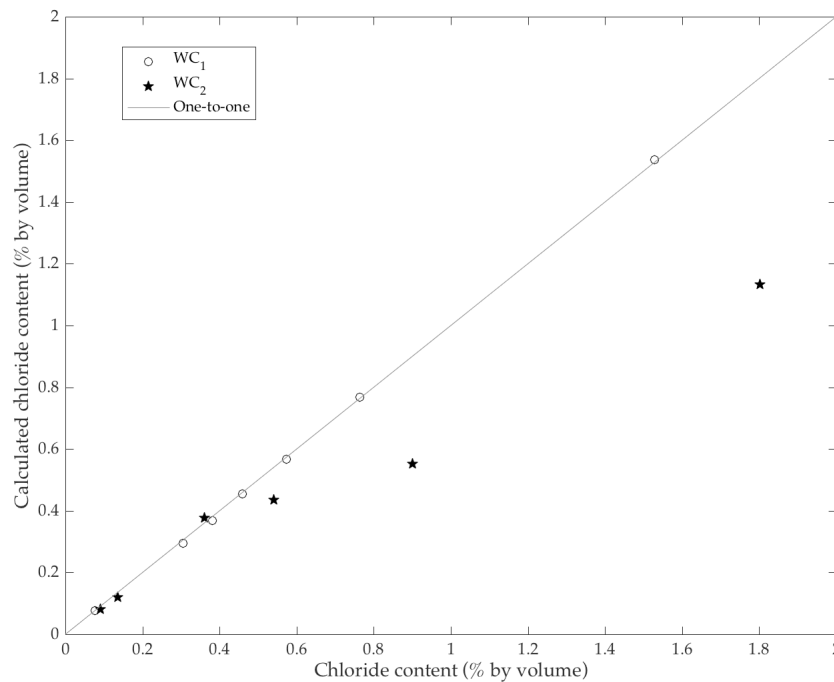
Figure 3.7: Expected contents versus the calculated contents. The 1:1 line is included for reference. Chloride contents were calculated using calibration line D1, after appropriately correcting for the volume of 1 g of cement in the paste.

3.3.7. Method performance regarding different cements

The method was also tested against different cements. It was not only tested with different commercially available CEM I cements, but also with three different blended cements. These types of cements are becoming more and more popular in an effort to reduce the carbon emission produced by the cement industry. An essential goal in the development of these cements with reduced environmental footprint is to achieve at least as good engineering properties as ordinary cement, and in particular comparable or better durability performance. It is therefore important to test any new proposed method applied to cementitious materials,

71

against the new trends in blended cements to see if the method can be easily applied to different cement types without having to recalibrate it each time.

The results of this investigation are summarized in Figure 3.8Figure 3.9. As it can be seen in Figure 3.8, the closeness of agreement for the different cements including the blended cements, lie in the same range as the method's validation set (as seen in Table 3.3, section 3.3.4). This shows that the slight variability in the composition does not strongly influence the results (see Figure 3.9). It is a very important result for practice since it means that only a limited calibration data set can be expected to be sufficient to characterize chloride content in a broad range of cement types. Particularly when analyzing concrete structures it means that reliable results can be obtained without having to a priori know the composition of the cement used.
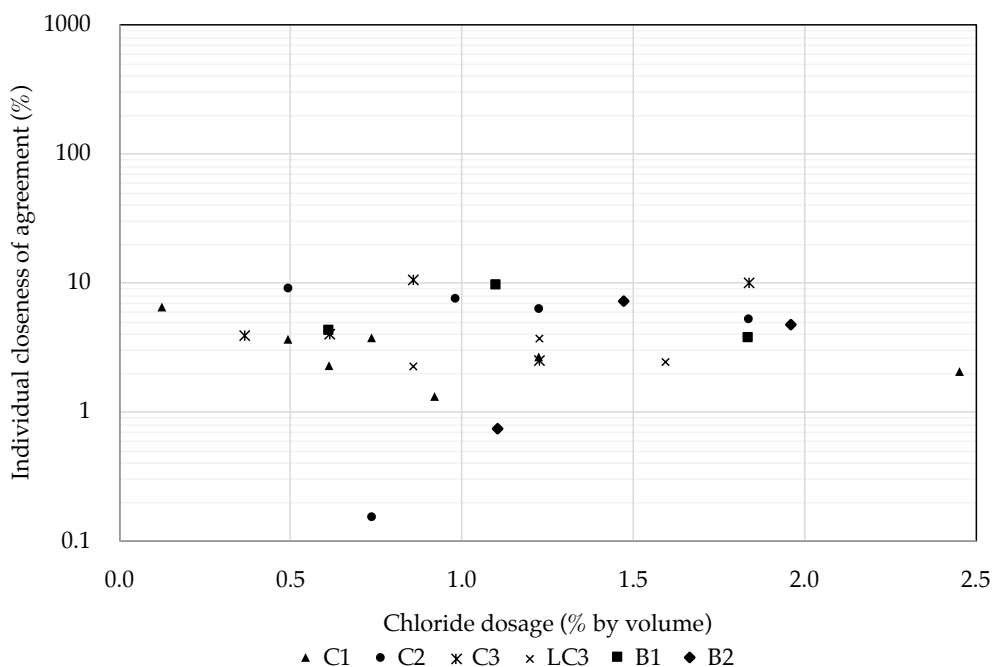

Figure 3.8: Individual closeness of agreement for each sample with of each cement. Chloride contents were calculated using calibration line D1 for all samples except B1 and B2 (and new Normo 5R), where D2 was used instead.
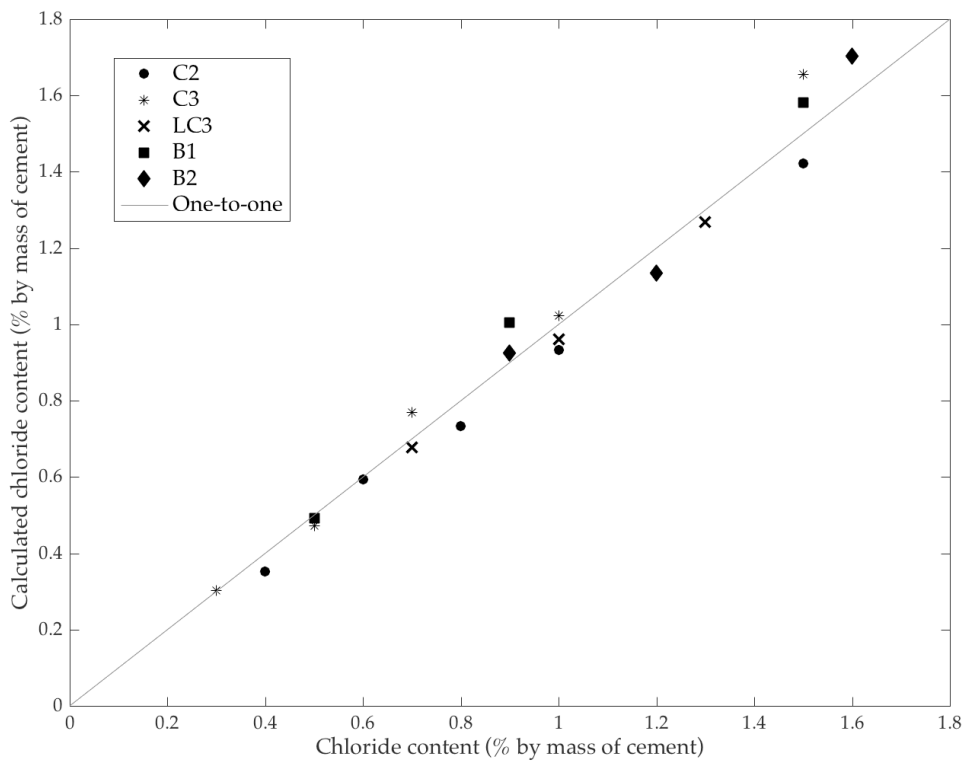
Figure 3.9: Expected contents versus the calculated contents. The 1:1 line is included for reference. Chloride contents were calculated using calibration line D1 for all samples except B1 and B2 (and new Normo 5R), where D2 was used instead.

3.3.8. SVM performance versus linear method

A great part of the project was focused on testing the potential value of the support vector machines to predict the chloride content in cement pastes. Although the performance was acceptable, it was not better than the linear calibration method described in this chapter. This section briefly presents the results of this study, in a very concise way.

The method consists on feeding the SVM with the spectra of the standards. The SVM learns from them and is able to predict the content in new samples. The

exact same samples and measurements were applied for this part of the study as in the previous sections.

As mentioned earlier, the replacement of the detector in the instrument affected the study, and the SVM was no exception. A new SVM was therefore trained with the new spectra to predict chloride contents in samples B1 and B2.

The method's performance in terms of closeness of agreement, with a different water cement ratio is shown in Figure 3.10. Values are between about 15 and 160 %. This is where the SVM shows its worst performance.
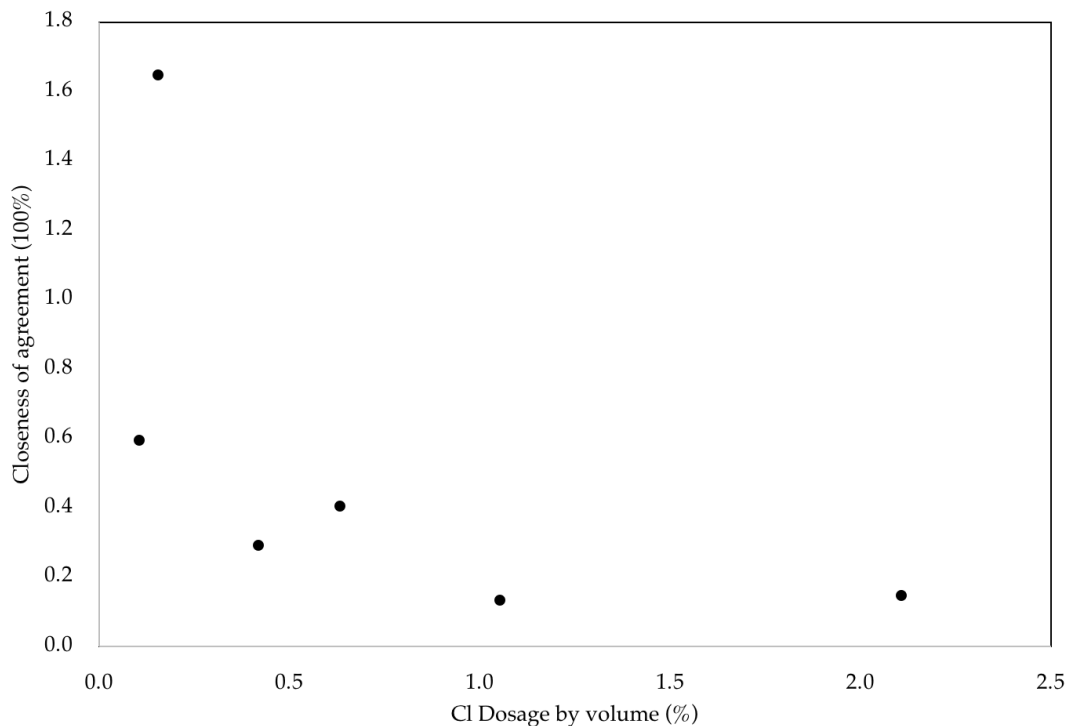

Figure 3.10: Individual closeness of agreement for each sample with a w/b of 0.55. Chloride contents were calculated using the SVM, after appropriately correcting for the volume of 1 g of cement in the paste.

The method's performance regarding different cements is shown in Figure 3.11. The results are slightly better than the comparison with a different w/c, however

it still performs poorly, in the sense that apart from some randomly selected spectra of the same standards used in the training, the prediction is clearly not better than the linear calibration method. The closeness of agreement in most of the results, is more than 10%.
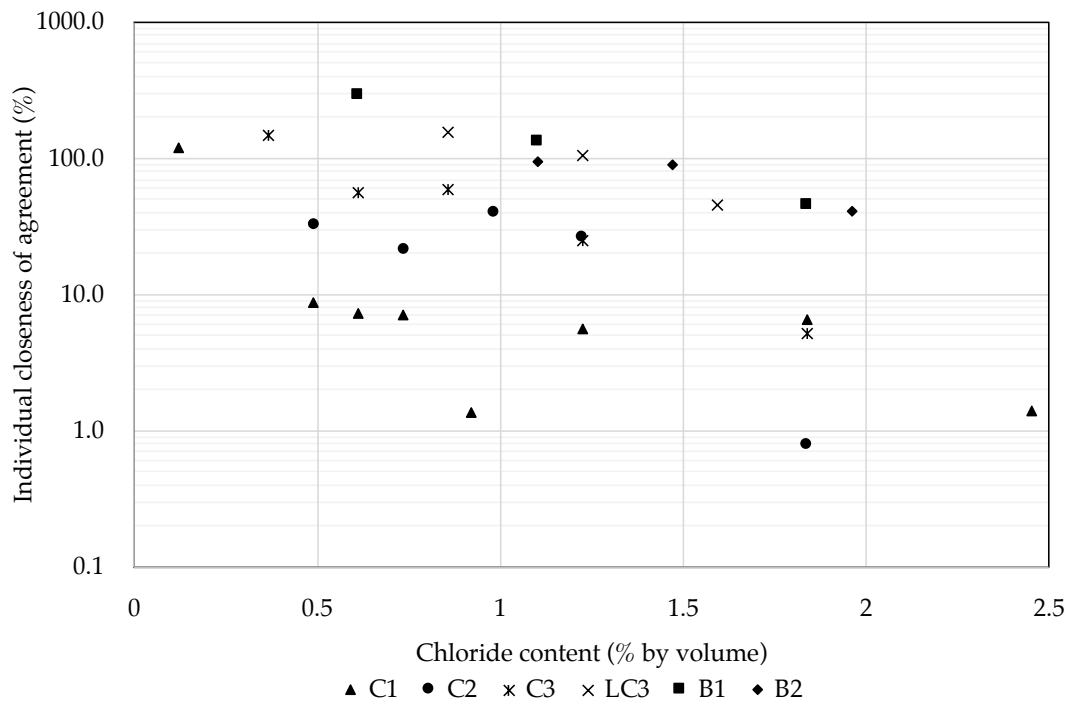
Figure 3.11: Individual closeness of agreement for each sample with of each cement. Chloride contents were calculated using the SVM for all samples.

The SVMs were being considered because one is able to feed the entire spectrum to train it, allowing for a supposedly more robust quantification method. Although it works, it still gives higher errors than a linear calibration procedure. Perhaps a deeper study and a better adjustment to the parameters of the SVM and the type, would result in a better method. However, our knowledge on the subject was limited, and after consulting with an expert in machine learning, it was concluded that having the entire spectrum was introducing many artifacts, thus over-riding the potential benefits of the approach. A suggestion was to

reduce the size of the spectrum to include less element peaks in the training set, but the problem was not fixed and the errors did not change much. All in all, the standard approach also delivers very reliable and accurate results, so that it is also difficult to improve an already very good situation. The SVM approach may therefore be better suited for other situation with more complex interactions that in our case.

3.3.9. Relevance of the method

The proposed method would be only partially destructive, since a core can be examined directly, but the core must nevertheless be taken and split. In fact, one of the most commonly used methods for determining chloride content in contaminated structures consists in taking sample cores followed by slicing the core at different depths, grinding the slices to collect the powder and finally analyzing the powder either by titration using nitric acid [25,33], or by XRF measurements [36].

Many practitioners prefer the XRF method as it allows them to directly test concrete and accurately determine the total chloride content [4,36]. However, this presents a few limitations. For instance, as it was mentioned earlier, the measured chloride content represents the average content over the volume being analyzed. Secondly, it is a time consuming and destructive method. But perhaps most importantly, XRF makes it impossible to distinguish between free and bound chlorides. Being aware of the difference facilitates the correct characterization of different features that are important in the concrete research field. Such features, for example, include the transport coefficient of chloride in concrete, the chloride binding capacity of cement, Friedel's salt formation kinetics and the critical chloride content for pitting corrosion initiation, among others.

This restriction regarding free and bound chlorides also affects the method described in this thesis. Even with a high spatial resolution, the measurement gives information only on the total chloride content. Consequently, it has to be combined with other methods to fully characterize the chlorides in the concrete.

A valid and convenient technique to measure and quantify free chlorides in concrete is the use of ion selective electrodes (ISE). These electrodes are embedded in the concrete specimens and allow for continuous monitoring of chloride contents in the pore solution (free chlorides) [4,36,40]. Specifically, silver/silver chloride (Ag/AgCl) electrodes have previously proven effective when measuring the chloride ion activity in concrete using highly localized point measurements with an accuracy on the microscopic scale [7,40,41].

3.4. Conclusions

On the whole, the method that we developed performs well on hardened cement pastes with different cements; different commercially available cements as well as cements with different compositions. This promises the option of using the method on samples obtained from the field where perhaps the composition of the cement is not known. In terms of different water-cement ratio, one has to be more cautious as it can introduce larger errors as the concentration of the chlorides increases.

The growing concern for the durability of reinforced concrete exposed to chloride-prone environments, makes further investigations on the behavior of chlorides in concrete particularly important. In this chapter, a micro XRF method for the quantitative analysis of chloride in hardened cement paste has been developed and validated to provide analytical support for such investigations.

Having spatial information on the chloride content is of great value for the field of concrete durability research. The technique is selective for chlorine in a cement paste matrix and provides a level of trueness comparable to the method suggested by the ISO for cement.

In the next chapter this method is applied to cement paste and mortar samples exposed to aggressive chloride environments. The method is used to quantify the chloride contents at certain depths after different times of exposure, and it is coupled with the method used by [40,41], which implements ion selective electrodes to quantify the free chloride contents. The results and limitations are discussed. Also in Chapter 4, the results of the application of the method to cement paste samples and mortar samples are discussed. Chapter 5 presents a case in which it is essential to have a spatial resolution of the chloride ingress. The formation of cold joints in digitally fabricated concrete, can pose a noteworthy problem for the material's durability.

Chapter 4 – Application: Insight into basic transport processes of chlorides

4.1. Introduction

As it was briefly reviewed in Chapter 2, there are two forms in which chlorides can be present in concrete, generally as free and bound chlorides. The free chlorides are dissolved in the pore solution, and they can be detrimental to the reinforcing steel in concrete. Once the free chlorides reach the reinforcement, the protective passivation layer on the steel can be damaged and corrosion occurs (*chloride induced corrosion*). The rest of the chlorides are either chemically bound into compounds such as Friedel's salt or physically adsorbed to the paste.

In order to accurately predict the service life of reinforced concrete structures that are exposed to aggressive chloride environments, both forms of chlorides must be identified. In addition, the spatial and temporal evolution due to diffusion and/or capillary suction must be accurately predicted.

In Chapter 3, the use of micro XRF as a means of obtaining the spatial distribution of total amount of chlorides at determined times is presented. While very valuable, this information is not sufficient and needs to be complemented by a reliable determination of the evolution of free chlorides.

An effective technique to do this in concrete is to use Ion Selective Electrodes (ISEs). These electrodes are typically embedded in the concrete specimens and allow for continuous monitoring of chloride contents in the pore solution (free chlorides) [4,36,40,89]. Specifically, silver/silver chloride (Ag/AgCl) electrodes have previously proven effective when measuring the chloride ion activity in concrete using highly localized point measurements with an accuracy on the microscopic scale [4,40,41].

The original intent of the work presented in this chapter was to couple the use of micro XRF with the chloride specific electrodes developed by Segui et al. [40,41,90] to gain insight into chloride transport by diffusion and capillary suction. Specifically, we aimed to use both methods to quantify the chlorides in specimens subjected to one or the other of these transport modes.

Unfortunately, it turned out that a number of "negative results" compromised this original objective. Nevertheless, a number of important conclusions were reached, that can help improve future experimental procedures. These are highlighted as results and are discussed in a separate section.

4.2. Experimental

4.2.1. Materials

A 25 kg-bag of fresh Portland cement (Normo 5R, certified CEM I 52.5 R, after Standard SN EN 197-1) provided by LafargeHolcim (LafargeHolcim Group Services Ltd/Holcim Technology Ltd, Zurich, Switzerland) was purposely stored in a barrel to prevent any change in composition due to possible hydration or carbonation. To stabilize the paste, a suspension of modified amorphous silica with an average particle size of 35 nm and a content of silica of 50% (w/w) was used (CEMbinder W8, AkzoNobel Specialty Chemicals, Moosleerau, Switzerland). Sodium chloride (NaCl for analysis EMSURE ®, ACS ISO, reag. Ph. Eur., Merck KGaA, Darmstadt, Germany) was used as chloride source. Sodium hydroxide (Sodium hydroxide pellets, analytical reagent grade, conforming to BP, EP; $\geq$ 98.3%; Fisher Chemicals, New Hampshire, USA), and calcium hydroxide (calcium hydroxide for analysis, puriss. p.a., Reag. Ph. Eur., 96%, Sigma-Aldrich, Missouri, USA) were used for the chloride solution to which the samples were exposed. The sand for the mortar samples was sieved through a No. 18 sieve, discarding the retained material.

The sensors used for this work were Ag/AgCl ion selective electrodes (ISE) (Metrohm AG, Zofingen, Switzerland). The sensors consist of a silver wire coated with AgCl deposited by anodizing. The final diameter of the sensor's tip is approximately 1.5 mm. In order to achieve a more stable membrane, approximately 5 mm of ISE tip was dipped in a melt of AgCl [40,41] (see Figure 4.1).
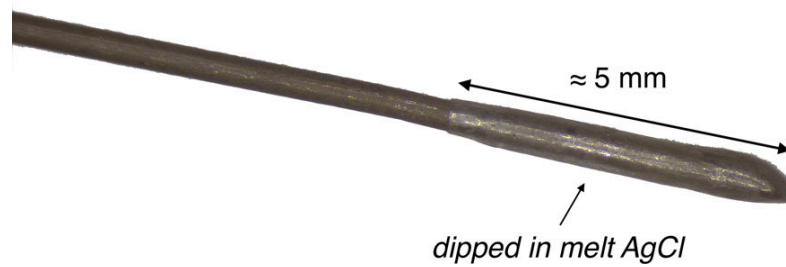
Figure 4.1: Ag/AgCl Ion selective Electrode. It consists of a AgCl coated silver wire. The diameter of the sensor's tip is about 1.5 mm [41].

Further preparation of the sensors consisted in isolating the rest of the sensor so that only the 5 mm tip is in contact with the cement paste or mortar. For this purpose, the sensors were first inserted in a tight plastic tube, then placed into a stainless steel hollow cylinder, with an outer diameter of 3.5 mm. Epoxy was carefully placed at the edges in order to seal the sensors.

4.2.2. Diffusion experiments

4.2.2.1. Sample preparation

Portland cement was mixed with deionized water (conductivity of 3.5 ± 0.7 μS/cm) with a water-to-cement ratio (w/c) of 0.60 (WC1) for a set of samples, and 0.45 (WC2) for another set. The ratio of amorphous silica to cement of 1:10 was used, which gives adequate fresh cement paste properties for the purposes of making the cement paste samples. Apart from the addition of sodium chloride, the mixing protocol was the same as the one used for the standards, which is described in Chapter 3. Samples were then cast in air tight, cylindrical molds with a diameter of 65 mm and height of 35 mm (see Figure 4.2). Four ISEs were embedded into the samples at the time of casting. Sensor 1, 2, 3, and 4 were placed 3, 6, 10, and 15 mm, respectively, from the edge on the sample as shown in Figure

4.2. The tips of the sensors were inserted 20 mm deep into the sample as shown in Figure 4.3. After casting, the samples were placed in an oven at 40° C for 14 days. The samples were then demolded and placed in a 95 % RH chamber at 20° C for 6 days. In the meantime, epoxy was placed on both the top and bottom of each cylinder in order to have a radial migration of chlorides into the sample.
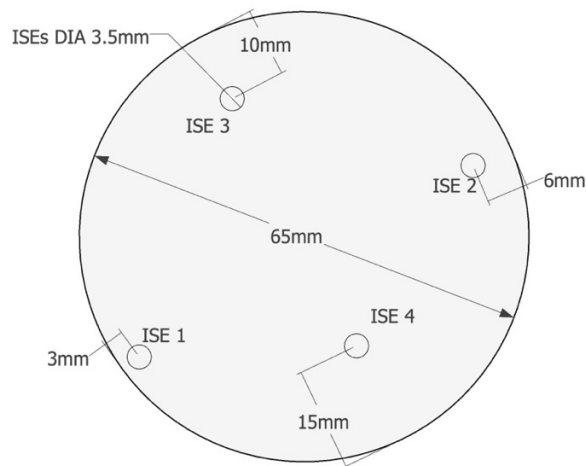
Figure 4.2: Top view of cylinders with the inserted sensors. The sensor were placed in the configuration shown in this figure. Sensor 1, sensor 2, sensor 3, and sensor 4 are at 3, 6, 10, and 15 mm from the edge of each sample, respectively.
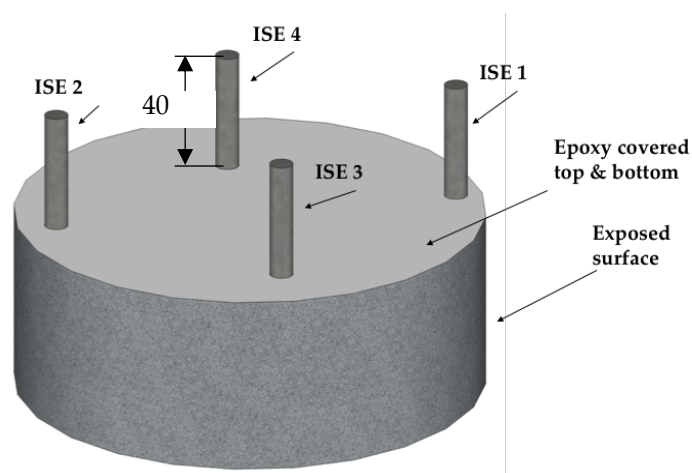

Figure 4.3: Samples for the diffusion experiments. The steel hollow cylinders were about 40 mm out for the samples. At the time of submersion, the steel tubes were well out of the solution.

4.2.2.2. Method

After the 20 days of sample conditioning, the samples were submerged in a chloride solution inside an air tight plastic box. The exposure solution consisted of 3 M NaCl + 0.1 M NaOH + sat. $Ca(OH)_2$, which was regularly stirred and monitored on a daily basis to maintain a constant pH, and chloride concentration. If necessary, the solution was changed for a newly prepared one. The samples were kept in the solution for the duration of the experiment. Measurements were taken for up to three different times for each w/c during this experiment (see Table 4.1). Samples were removed from the solution and split perpendicularly to the circular face the morning right before starting the micro XRF mapping. The potential difference of the ISEs was measured regularly during the time of the experiment. The measurement methods will be discussed with more detail in section 4.2.5 below.

Table 4.1: Time (in days) for which samples were submerged in the chloride solution.

Submersion time (days)		
Sampling time	**WC1**	**WC2**
t1	51	98
t2	98	118
t3	118	144

4.2.3. Capillary rise

4.2.3.1. Sample preparation

Two mortars were prepared for these experiments (M1 and M2, see Table 4.2). Portland cement was manually mixed with the sand, to which deionized water (conductivity of 3.5 ± 0.7 µS/cm), mixed with the amorphous silica was added to obtain a water-to-cement ratio (w/c) of 0.4 (WC3) for M1, and 0.5 (WC4) for M2. A different ratio of amorphous silica to cement was used for each mortar (See Table 4.2). Samples were cast in 50 mm cubic molds (see Figure 4.4). Three ISEs were embedded into the samples at the time of casting. The configuration can be seen in Figure 4.4. The tips of the sensors were all at the same depth, namely 25 mm from the side. A set of 3 samples was prepared for M1, and two sets of 3 samples were prepared for M2. After casting, the samples were placed in a 95 % RH chamber at 20° C for 48 hours after which they were demolded and kept in the same chamber for 4 weeks. After this curing time, the samples were placed in a climatic chamber at 30 % RH and 10° C for drying. The samples were kept in the chamber until a constant mass was achieved. No further conditioning was performed before the experiments.

Table 4.2: Mix composition for M1 and M2. Values are given as a mass ratio with respect to mass of cement.

Mortars compositions (ratio w.r.t cement by mass)

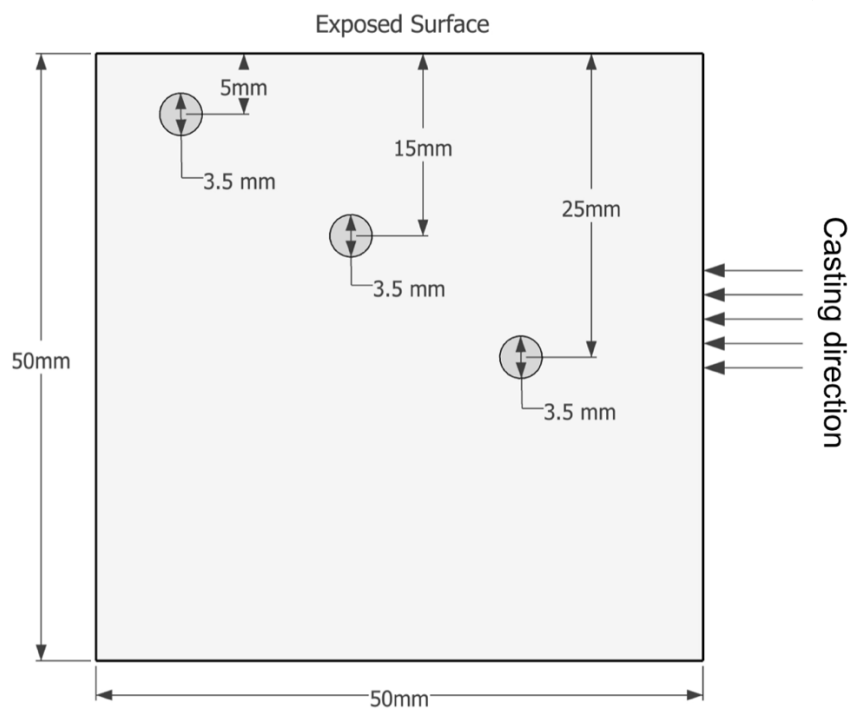| Component	M1	M2
w/c	0.4	0.5
CemBinder	1:100	1:20
Sand (0-1 mm)	1:3	1:3

Figure 4.4: Side view and dimensions of the mortar samples. The cubes are 50 x 50 x 50 mm. The distances shown in the figure represent the distance of each ISE from the surface exposed to the chloride solution. Casting direction is from the right side as shown in the figure.

4.2.3.2. Method

The samples were exposed to chlorides by means of capillary rise. The samples were suspended from a balance, so that one of the faces was in contact with the solution containing the chlorides, as shown in Figure 4.5. The exposure solution 1 (S1) consisted of 1 M NaCl + 0.1 M NaOH + sat. $Ca(OH)_2$, and exposure solution 2 (S2) consisted of 2 M NaCl + 0.1 M NaOH + sat. $Ca(OH)_2$. The experiments were run for their respective time (see Table 4.3 for a summary of the experimental procedure), after which the samples were dry cut, perpendicularly to the exposed surface. Stopping the experiment and cutting the sample was done the morning right before starting the micro XRF mapping.

The potential difference of the ISEs was measured every hour during the time of the experiment. The measurement methods will be discussed with more detail in section 4.2.5 below.

Table 4.3: Experimental plan for capillary suction experiments.

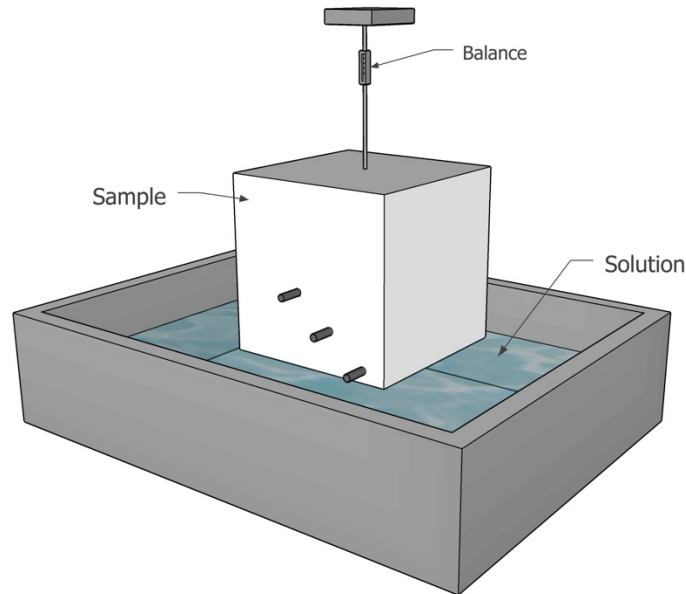| Sample	Mix	Exposure solution	Time (hours)
M01-1			48
M01-2	M1	S1	24
M01-3			36
M02-1			48
M02-2	M2	S2	24
M02-3			36
M03-1			24
M03-2	M2	S1	48
M03-3			36

Figure 4.5: Schematic representation of the surface exposed to chlorides. The samples were suspended from a balance that recorded the mass increase of the specimen resulting from absorption of water.

4.2.4. Ion selective electrodes

The Ag/AgCl ISE used for this chapter belongs to the category of ion-selective electrodes with solid ion exchangers [40,41,91]. Since the AgCl coating has a low solubility, the electrolyte around the ISE is easily saturated with it and the ISE's measured potential E is given by the Nernst equation [92]:

$$E_{meas} = E^0_{Ag/AgCl} - \frac{RT}{F} ln a_{Cl^-} \tag{4.1}$$

where R is the gas constant, F is the Faraday constant, T is the absolute temperature, a_{Cl^-} is the activity of the chloride, and $E^0_{Ag/AgCl}$ is the standard potential of the Ag/AgCl electrode. The electrode standard potential is 27 mV vs. Ag/AgCl/sat. KCl at 20 °C [41]. Equation (4.1) has been simplified assuming

the diffusion potential is negligible, which means that no carbonation has occurred. In other words, it is assumed that there is no pH gradient within the sample [90].

The potential of the ISEs was measured against the Ag/AgCl/sat. KCl reference electrode. Using Equation (4.1), the chloride activity is obtained. The chloride activity can then be converted to a concentration following the procedures presented in [40,41,90], where they use the activity coefficients of chloride ions in cement paste obtained in reference [93,94]. A correlation can be obtained by plotting the logarithm of the chloride concentration versus the logarithm of the chloride activities as shown in Figure 4.6.
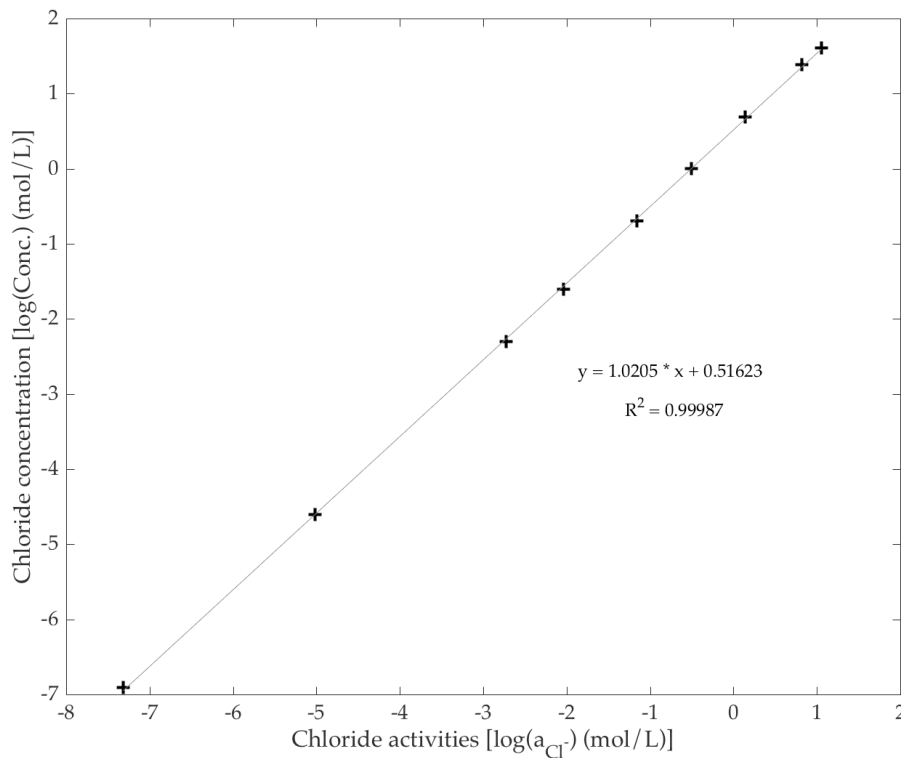

Figure 4.6: The logarithm of the chloride concentrations (mol/L) as a function of the logarithm of the chloride activity (mol/L). The values are obtained from [94].

4.2.5. Micro XRF

4.2.5.1. Diffusion samples

The measurement protocol was the following: The relatively freshly cut surfaces of the samples were mapped with a 80 μm resolution. The applied acceleration potential and current were 35 kV and 950 μA, respectively. At each point of the map, a spectrum was acquired for 300 ms. Measurements were carried out in air with a built-in 25-μm thick aluminum filter to eliminate the rhodium Lα radiation and, therefore, preventing it from reaching the sample. This is necessary because this radiation overlaps with the chlorine Kα X-ray line and increases its limit of detection. Calibration curve for detector D1 was used for this experiment (see Chapter 3, Figure 3.2).

4.2.5.2. Capillary suction samples

The measurement protocol was the following: The relatively freshly cut surfaces of the samples were mapped with a 45 μm resolution. The applied acceleration potential and current were 35 kV and 950 μA, respectively. At each point, a spectrum was acquired for 150 ms. Measurements were carried out in air with a built-in 25-μm thick aluminum filter to eliminate the rhodium Lα radiation and, therefore, preventing it from reaching the sample. Calibration curve for detector D2 was used for this experiment (see Chapter 3, Figure 3.3).

The spectral maps were not processed due to proprietary issues with the way the data was saved during spectra collection. However, the grey scale maps, which

are proportional to the intensities of chlorides, were retrieved and a very rough image analysis was done to study and understand the results. Additionally, the ORBIS Vision software (see Chapter 2, section 2.4.5) was used to calculate the net intensities (needed for the conversion to % Cl by mass of cement) of areas around the sensors (see discussion).

4.3. Results

4.3.1. Diffusion transport

4.3.1.1. High water cement ratio (WC1= 0.6)

The results of the experiment at W/C = 0.60 (WC1) are summarized in this section. Figure 4.7 shows the chloride concentrations calculated using Equation 4.1 as a function of time for different ISE depths. ISE 1, ISE 2, ISE 3 and ISE 4 are at a depth of 3, 6, 10 and 15 mm, respectively. Samples 1, 2, and 3 are the samples that were removed from the solution after t1 = 51 days. As expected, the concentrations increase with time and decrease with depth.
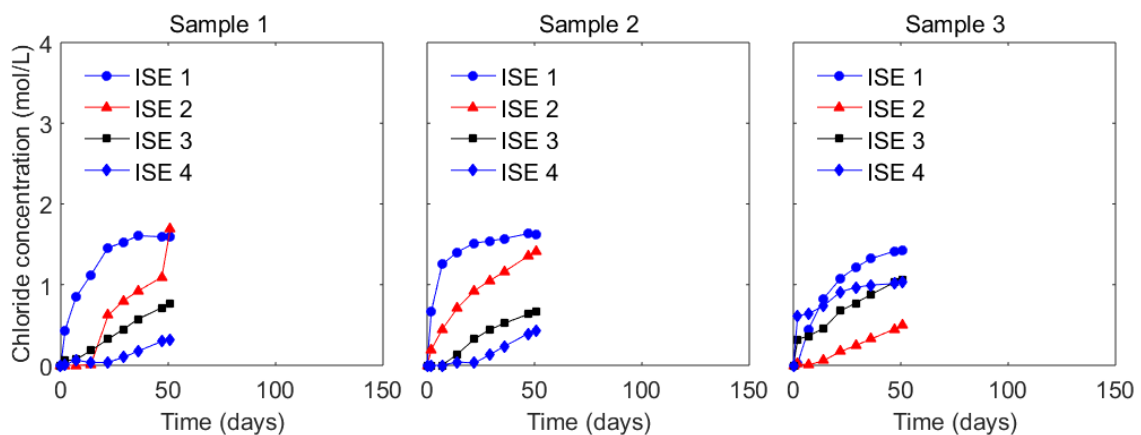

Figure 4.7: Chloride concentration as a function of time for each Ag/AgCl ISE in the WC1 samples set for sampling time t1 (51 days). Depths for ISE 1, ISE 2, ISE 3 and ISE 4 are 3, 6, 10 and 15 mm, respectively.

Figure 4.8 shows similar results obtained over a longer time period (sampling time t2 = 98 days) for samples 4, 5, and 6. For comparison ease, the scale of the axes is kept constant for all graphs. One observation that can be made is that several samples exhibit a discontinuity in the evolution of the ISE measurements at around 50 days. This happened when samples 1, 2 and 3 were removed for micro-XRF analysis, and the solution was replenished. This discontinuity is attributed to a modification of the diffusion potential as explained in the discussion section.

Figure 4.8: Chloride concentration as a function of time for each Ag/AgCl ISE in the WC1 samples set for sampling time t2 (98 days). Depths for ISE 1, ISE2, ISE 3 and ISE 4 are 3, mm, respectively.

Figure 4.9 presents chloride sensor data obtained on samples 7, 8, and 9, which were in the solution for t3 = 118 days. From Figure 4.8 to Figure 4.9, it can be seen that the concentration of chlorides continues to increase as time passes. As before, we observe sudden jumps in the concentration at the same well defined times. Moreover for samples 7 and 9 there is an additional discontinuity at 118 days. Again, this change is attributed to the change of the storage solution and its impact on the diffusion potential.

The free chloride concentrations are also plotted as a function of depth in the samples, and are presented in Figure 4.10. Each data point corresponds to the specific depths of ISE 1, 2, 3, and 4. Apart from the significantly lower concentration in ISE 2 (ISE = 6 mm) in sample 3, the time evolution of chloride concentration in the samples are as expected. At sampling time t3, the concentration in the samples is somewhat constant and it approaches the concentration of the exposure solution (i.e. 3 M NaCl).
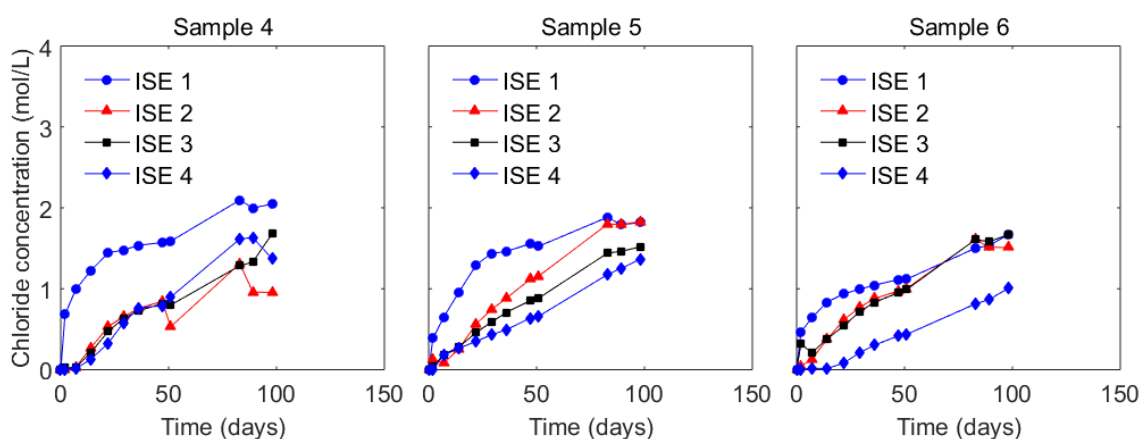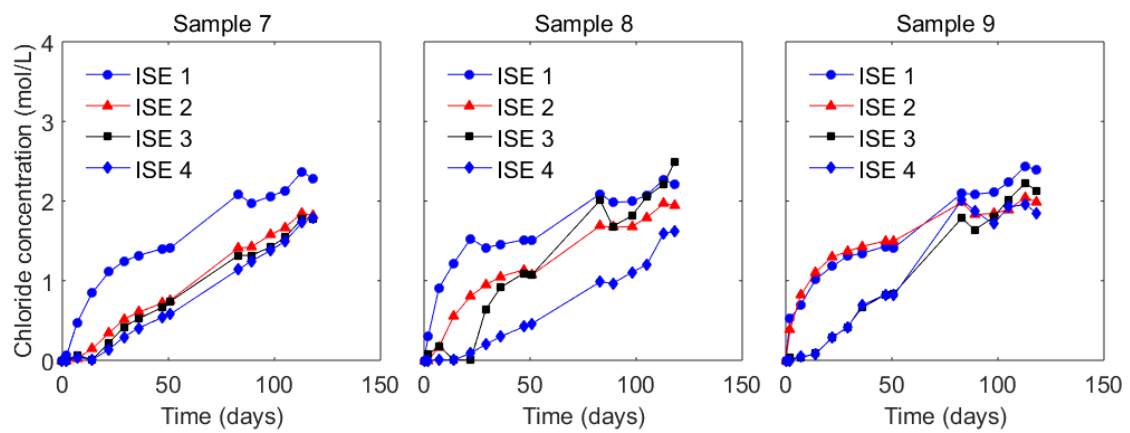

Figure 4.9: Chloride concentration as a function of time for each Ag/AgCl ISE in the WC1 samples set for sampling time t3 (118 days). Depths for ISE 1, ISE 2, ISE 3 and ISE 4 are 3, 6, 10 and 15 mm, respectively.
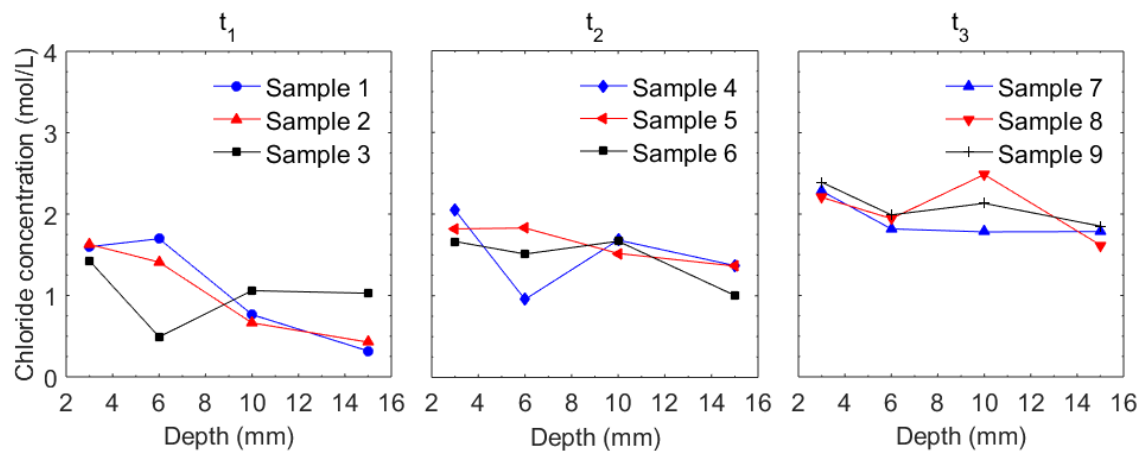

Figure 4.10: Chloride concentration as a function of depth for the WC1 sample set at sampling times t1, t2, and t3.

With respect to the total chloride ingress, a map was obtained for one of the three samples at each sampling time (t1, t2 and t3). The general orientation of the maps is presented in Figure 4.11. The samples (in Figure 4.3) were split, and one of the freshly split surfaces was mapped. Because of fractures, or time constraints, it was not always possible to map the entire cross section. However, the position of the area and the scale of each map was always recorded for further analysis.
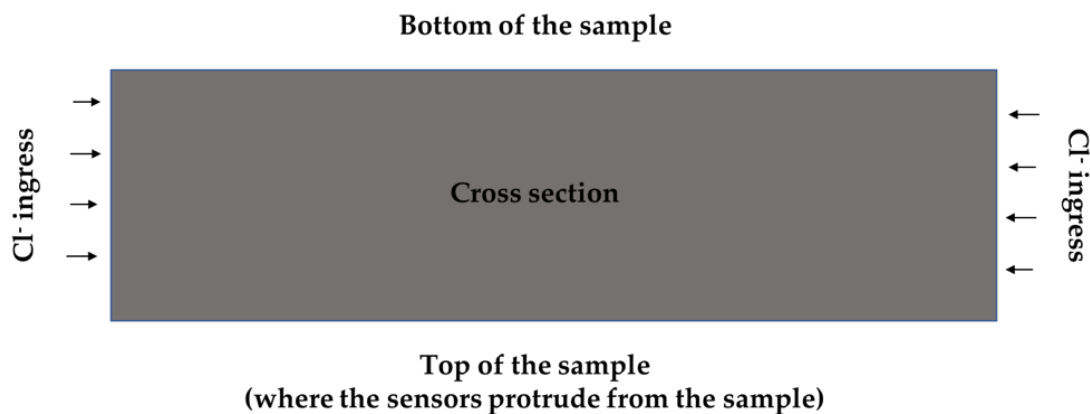
Figure 4.11: General orientation of the maps for diffusion-experiment-samples (unless otherwise stated). One of the edges was always fully mapped. It was assumed that the chloride front was homogenous, and that the chloride front moved radially into the sample. Given this assumption, the chloride concentrations at the depth of each ISE, were mined with respect to on side only. As a reminder the top and bottom of the sample were covered with an epoxy to prevent chloride ingress from those sides.

Figure 4.12 to Figure 4.14 show the chloride quantitative maps of samples 3, 6 and 7 respectively. Each graph is accompanied by its color bar, which represents the range of the chloride concentrations expressed in % by mass of cement. Notably, the quantitative analysis was performed using the calibration line for detector 1 (D1, see Chapter 3, section 3.3.1).

The maps show quite some variability from sample to sample. However, they all show a preferential ingress of the chlorides on the top of the images, which

corresponds to the bottom of the sample. This suggests some segregation during casting and curing, which affects the chloride ingress throughout the sample (see discussion section). In addition to the variability in the chloride ingress, the scatter can affect the sensitivity of the sensors.

Figure 4.12: WC1 sample 3 at time t1. The color bar indicates the chloride concentration in % by mass of cement. The area is 63.2 mm by 18.5 mm (0.08 mm per pixel). The left edge was used for the analysis.

The chloride map in Figure 4.12, is downscaled by a few measurement points (at around pixel {410, 210}). Nonetheless, it is still somewhat visible that the chloride contents at the edges are higher than in the middle. Another visible feature is the brighter band at about pixel row 200 in the y direction. Next, the map in Figure 4.13, shows a slighter deeper penetration of chlorides. In this case, the difference of the chloride penetration between the top/bottom and the middle of the sample is more obvious. Finally, the map in Figure 4.14, exhibits an even more obvious difference between top/bottom and the middle. The crack was inflicted when the sample was split.
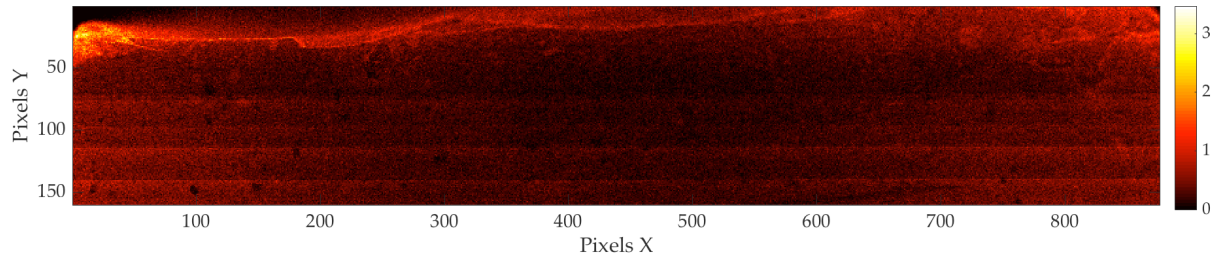
Figure 4.13: WC1 sample 6 at time t2. The color bar indicates the chloride concentration in % by mass of cement. The area is 65.5 mm by 12.3 mm (0.08 mm per pixel). The right edge was used for the analysis.
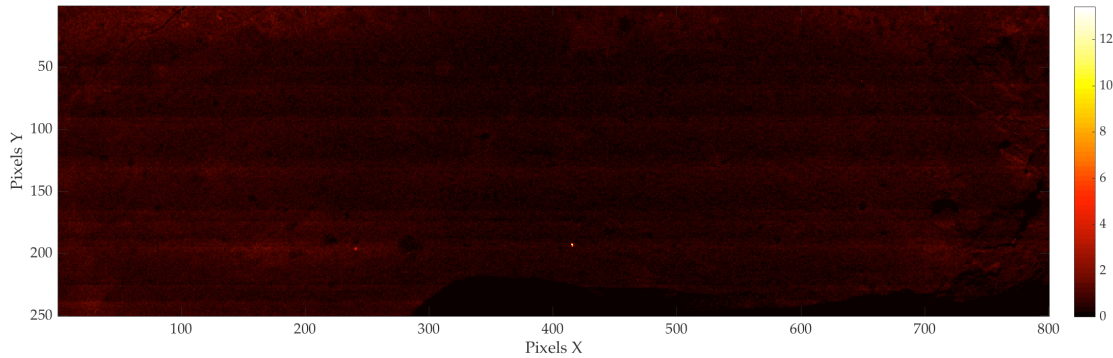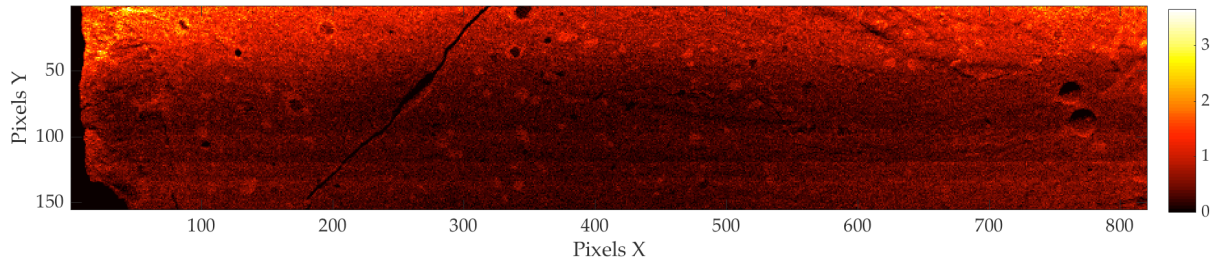

Figure 4.14: WC1 sample 7 at time t3. The color bar indicates the chloride concentration in % by mass of cement. The area is 65.6 mm by 12.4 mm (0.08 mm per pixel). The left edge was used for the analysis. (Unlike the general orientation of the maps, this map's top represents the top of the sample).

The chloride contents at the depth of the ISEs were determined in an area around the sensor, where the location of the sensor was calculated given the resolution of the maps. The areas consist of 19 by 19 pixels (1.5 by 1.5 mm^2), and the total area matrix was a 9 x 9 matrix around the sensor. However, because of the sample inhomogeneity (not visible before mapping the chlorides), the data of the sensors cannot be reliably compared to that of the maps. Instead, a range of chloride concentrations in an area around the sensors is given in Table 4.4

Table 4.4: Summary of chloride concentrations as per each of the two methods at hand for WC1. Results for the µXRF is presented as a range within an area of 4.5 mm by 4.5 mm. Times t1, t2 and t3, are 51, 98 and 118 days respectively.

Sensor	t1		t2		t3	
	µXRF (% w/w)	Nernst Eq. (mol/L)	µXRF (% w/w)	Nernst Eq. (mol/L)	µXRF (% w/w)	Nernst Eq. (mol/L)
ISE 1	0.2 - 1.2	1.4	0.1 – 1.0	1.7	* - 1.1	2.3
ISE 2	0.2 - 1.2	0.5	0.1 - 0.9	1.5	0.1 - 0.9	1.8
ISE 3	0.2 - 1.2	1.1	0.1 - 0.8	1.7	0.1 - 0.9	1.8
ISE 4	0.1 - 1.1	1.0	* - 0.7	1.0	* - 0.8	1.8

* Values are below the limit of quantification

4.3.1.2. Low(er) water cement ratio (WC2= 0.45)

The results of the diffusion experiment on samples with the lower water to cement ratio WC2 (0.45) are summarized in this section. Figure 4.15 shows the free chloride concentrations measured in samples 10, 11, and 12 up to sampling time t1 = 98 days. As for WC1, the behavior is as expected with concentrations increasing with time and decreasing with depth within the samples. As before also, some potential discontinuities were observed at about 50 days when the solution was replenished.

Figure 4.15: Chloride concentration as a function of time for each Ag/AgCl ISE in the WC2 samples set for sampling time t1 (98 days). Depths for ISE 1, ISE 2, ISE 3 and ISE 4 are 3, 6, 10 and 15 mm, respectively.

Figure 4.16 extends the time scale for the measurements of free chlorides, showing data obtained on samples 13 and 16 up to sampling time t2 = 113 days. For comparison's ease the axes were kept constant for all graphs. Here the discontinuity at 50 days is even more obvious and an additional one can be seen at about 90 days.
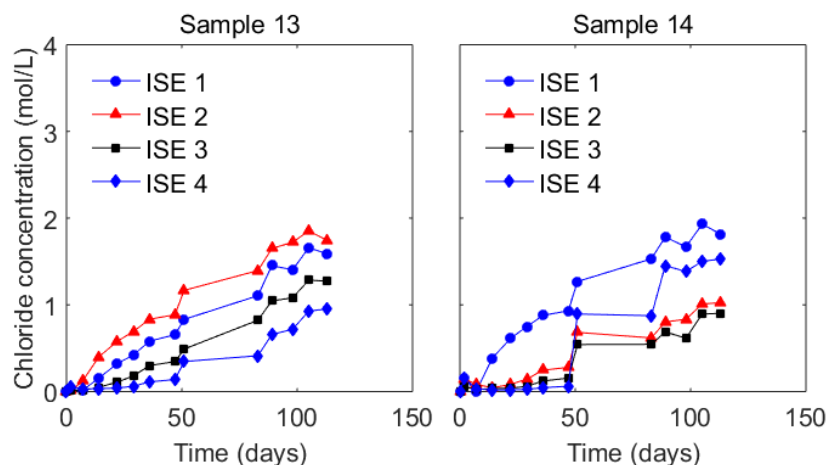
Figure 4.16: Chloride concentration as a function of time for each Ag/AgCl ISE in the WC2 samples set for time t2 (113 days). Depths for ISE 1, ISE 2, ISE 3 and ISE 4 are 3, 6, 10 and 15 mm, respectively.
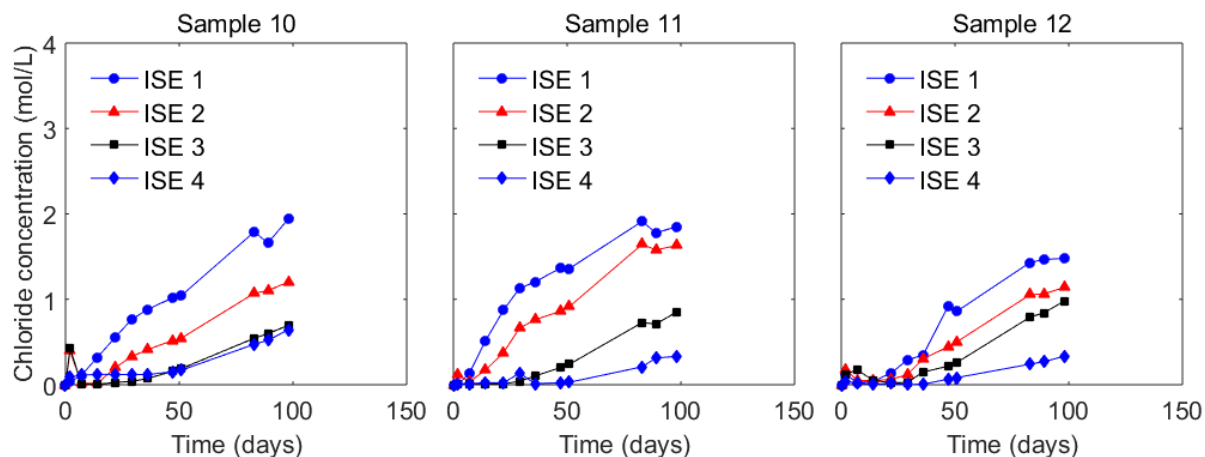
98
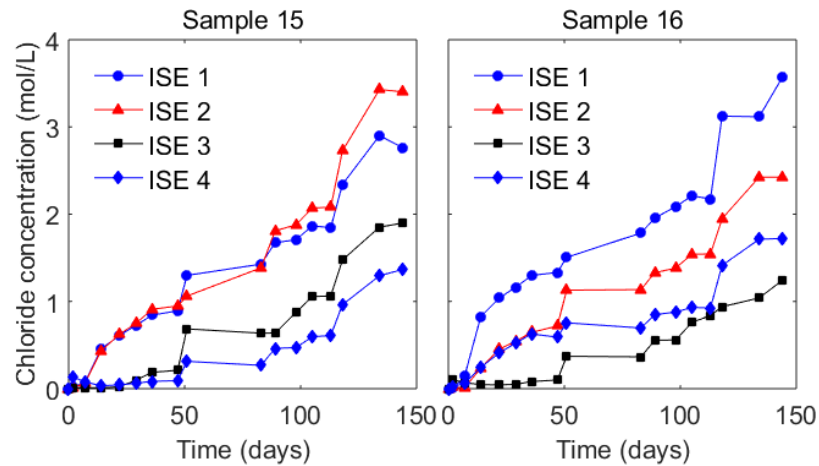
Figure 4.17 : Chloride concentration as a function of time for each Ag/AgCl ISE in the WC2 samples set for time t3 (144 days). Depths for ISE 1, ISE 2, ISE 3 and ISE 4 are 3, 6, 10 and 15 mm, respectively.

The last representation of the evolution of free chlorides is given in Figure 4.17 for samples 15, and 16 until sampling time t3 = 144 days. From Figure 4.16, and Figure 4.17, it can be seen that, unsurprisingly, the concentration of chlorides continues to increase as time passes by.

The above results are also shown as a function of depth in Figure 4.18 for sampling times t1, t2 and t3. The chloride profiles for sampling time t1 show an expected decreasing chloride content with increasing depth. At sampling time t2, the profiles are leveled out, while they are once again developed at sampling time t3. The reason for this "reactivation" of the chloride ingress is not clear. It could be that chlorides in the vicinity of the sample were depleted between t1 and t2 and that the solution replacement at t2 reactivated chloride diffusion into the samples.
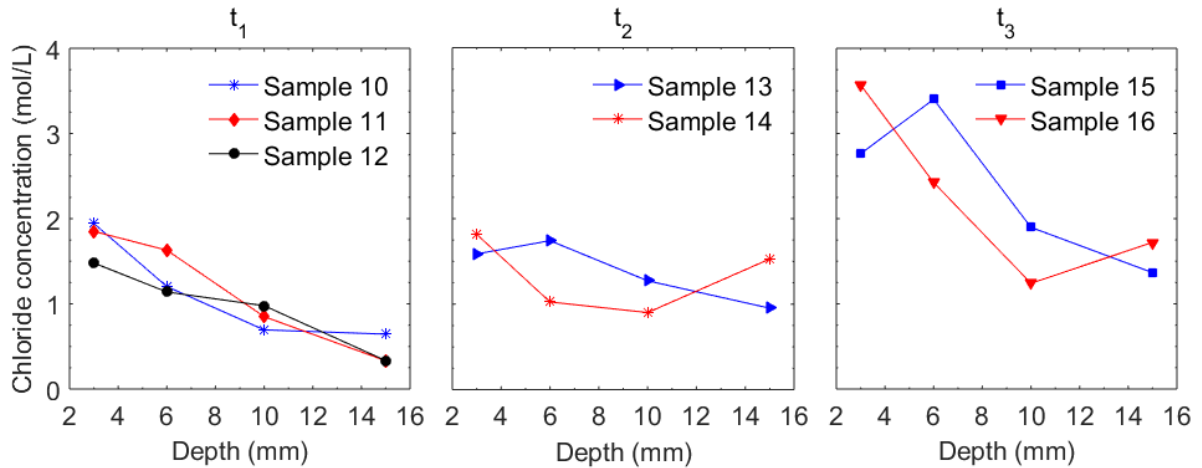
Figure 4.18: Chloride concentration as a function of depth for the WC2 sample set at time t1, t2 and t3.

Figure 4.19 to Figure 4.21, show the chloride quantitative maps of samples 12, 13, and 15, respectively. Each graph is accompanied by its color bar, which represents the range of the chloride concentrations expressed in % by mass of cement. It is important as well to note that the quantitative analysis was performed using the calibration line for detector 1 (D1, see Chapter 3, section 3.3.1).

The maps show less variability than the samples with higher W/C, and the chloride concentrations are visibly higher at the edges than in the center. However, there is still a visibly favored path at the top of the image, respectively at bottom of the samples. However, this feature is much less pronounced compared to the samples with the higher W/C.
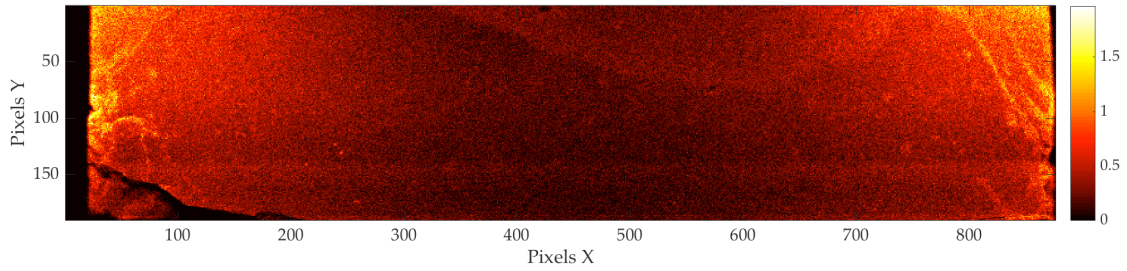
Figure 4.19: WC2 sample 12 at time t1. The color bar indicates the chloride concentration in % by mass of cement. The area is 68.3 mm by 17.9 mm (0.08 mm per pixel). The left edge was used for the analysis.
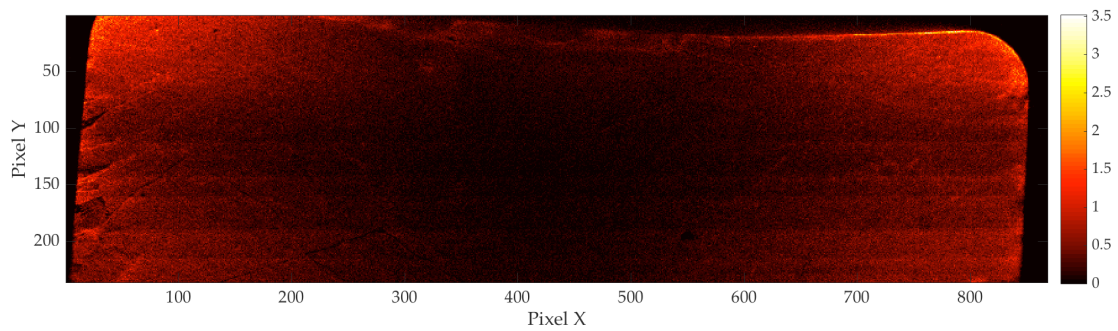
Figure 4.20: WC2 sample 13 at time t2. The color bar indicates the chloride concentration in % by mass of cement. The area is 69.4 mm by 18.9 mm (0.08 mm per pixel). The right edge was used for the analysis.
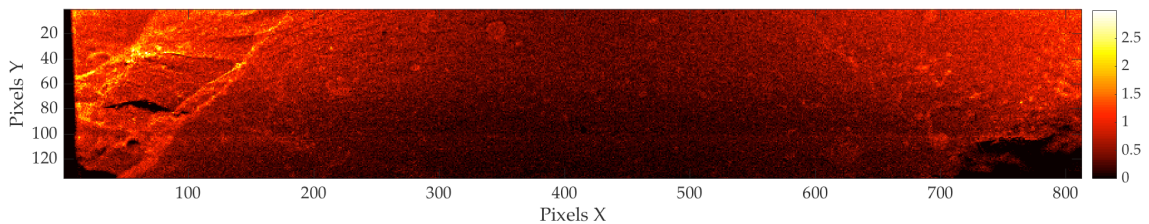
Figure 4.21: WC2 sample 15 at time t3. The color bar indicates the chloride concentration in % by mass of cement. The area is 65.0 mm by 10.8 mm (0.08 mm per pixel). The left edge was used for the analysis.

The chloride concentrations at the depth of the ISEs were calculated in the same way as for the WC1 set. An area around the sensor was evaluated. The areas also consist of 19 by 19 pixels (1.5 by 1.5 mm^2), and the area matrix was a 9 x 9 around each sensor.

Table 4.5: Summary of chloride concentrations as per each of the two methods at hand for WC2. Results for the µXRF is presented as a range within an area of 4.5 mm by 4.5 mm. Times t1, t2, and t3, are 98, 118, and 144 days, respectively. The data related to the sensors was obtained from the corresponding samples (referenced in the quantification maps above).

Sensor	t1		t2		t3	
	µXRF (% w/w)	Nernst Eq. (mol/L)	µXRF (% w/w)	Nernst Eq. (mol/L)	µXRF (% w/w)	Nernst Eq. (mol/L)
ISE 1	0.2 - 1.2	1.4	0.1 – 1.0	1.7	* - 1.1	2.3
ISE 2	0.2 - 1.2	0.5	0.1 - 0.9	1.5	0.1 - 0.9	1.8
ISE 3	0.2 - 1.2	1.1	0.1 - 0.8	1.7	0.1 - 0.9	1.8
ISE 4	0.1 - 1.1	1.0	* - 0.7	1.0	* - 0.8	1.8

4.3.2.Capillary rise

The results of the capillary rise experiments are summarized in this section. Figure 4.22 summarizes the chloride concentrations that were calculated using Equation (4.1), for all mortar samples. Figures on each row represent analogous samples that were analyzed by micro-XRF at different times. Thus, the

comparison of each row can be used to judge the reproducibility of these experiments and this turns out to be very poor. Additionally, we note that the concentrations measured are extremely high, much higher than the solution in contact with the samples. As explained in the discussion section, this is not related to evaporation and crystallization of salts during the capillary rise. Rather, these problems are attributed to streaming potentials, which arise from the flow of a salt solution in porous materials that have charged pore walls (see discussion section). This issue unfortunately means that the chloride sensor measurements in capillary rise are inconclusive, but nevertheless it was important to document this issue within the current chapter.

A chloride map was obtained for each sample; however, once the maps were complete, there was some clear evidence of cracks in some samples. Because of this some representative maps were selected with which the rest of the analysis was made. Figure 4.23 through Figure 4.26 show the qualitative chloride maps of samples M01-1, M01-2, M02-1, and M03-1, respectively. Each graph is accompanied by its color bar, which represents the range of grey intensity of the maps. For illustration purposes Figure 4.27 depicts the chloride map of a cracked sample. Other samples exhibited similar maps and were therefore discarded because as it is well known, the presence of cracks can dramatically affect the chloride ingress into a cementitious material [95–97], and those effects are out of the scope of this thesis. The cracks were most likely present before the experiment was run, and not caused by salt crystallization.
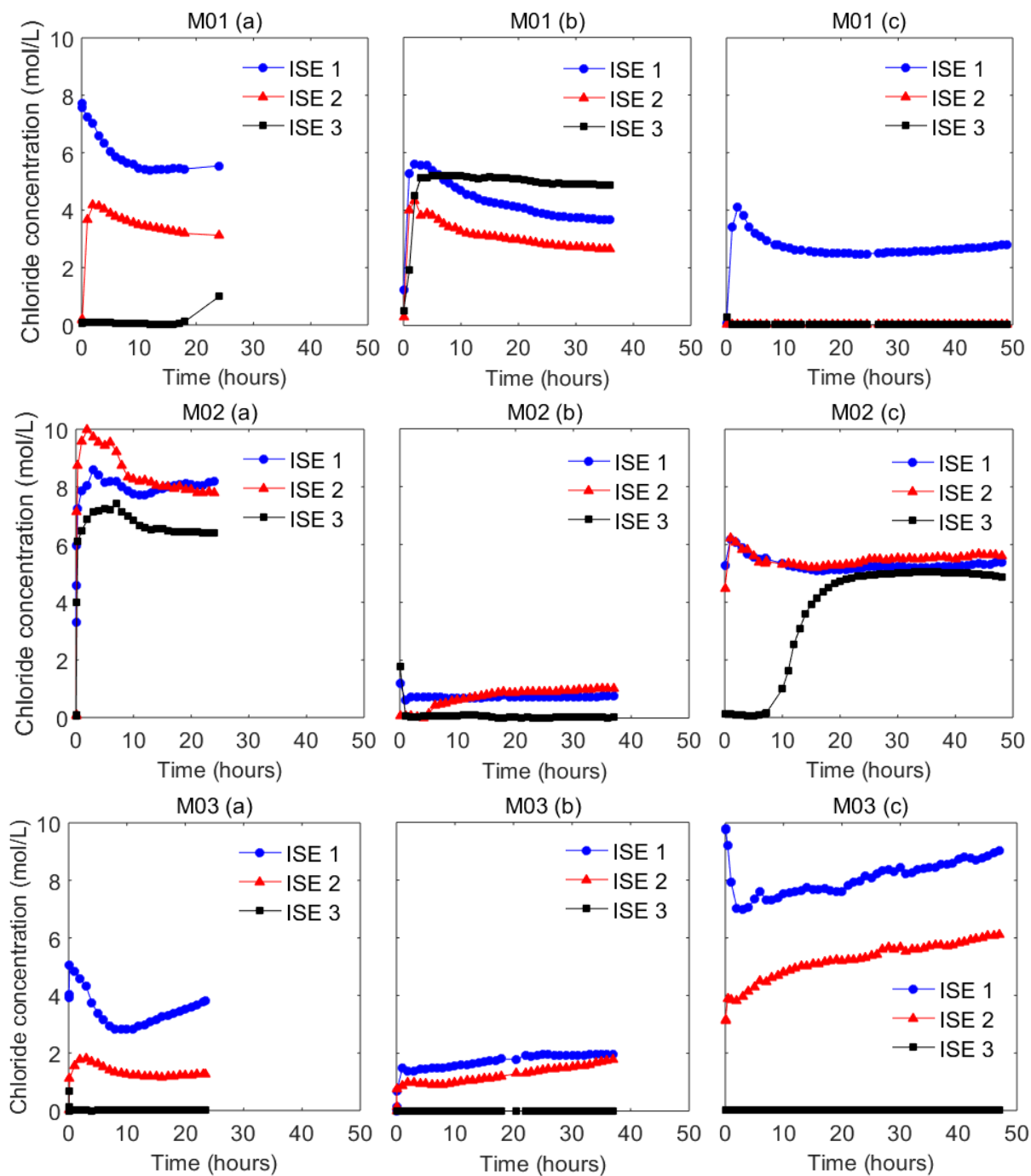
Figure 4.22: Chloride concentrations as a function of time for the Ag/AgCl ISE at each depth. Depths for ISE 1, ISE 2, and ISE 3 are 5, 15 and 25 mm, respectively. The letter (a) represents the samples that were exposed to the solution for 24 hours, (b) for 36 hours, and (c) for 48 hours.
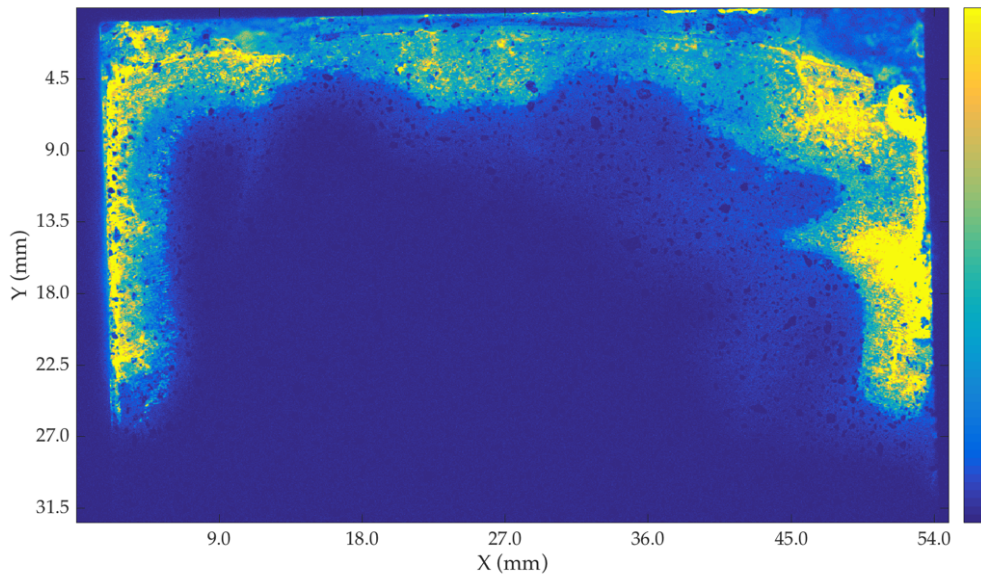
Figure 4.23: Qualitative chloride map of sample M01-1 (M01(c) in fig. 4.22). The chloride ingress is from the top of the picture (0.045 mm per pixel). The color bar represents the intensity of the grey scale, meaning this map is only qualitative (blue means no chlorides, whereas yellow means the highest chloride contents).
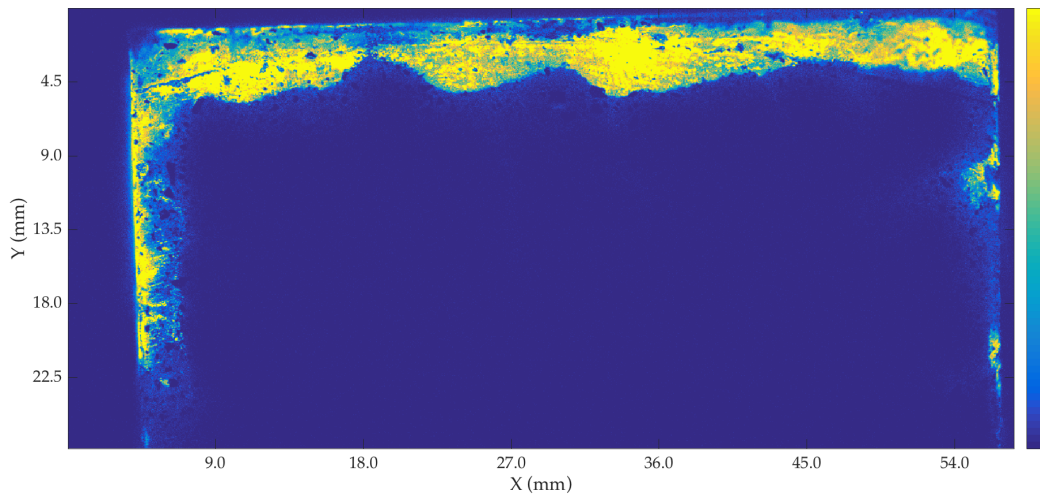
Figure 4.24: Qualitative chloride map of sample M01-2 (M01(a) in fig. 4.22). The chloride ingress is from the top of the picture (0.045 mm per pixel). The color bar represents the intensity of the grey scale, meaning this map is only qualitative (blue means no chlorides, whereas yellow means the highest chloride contents).
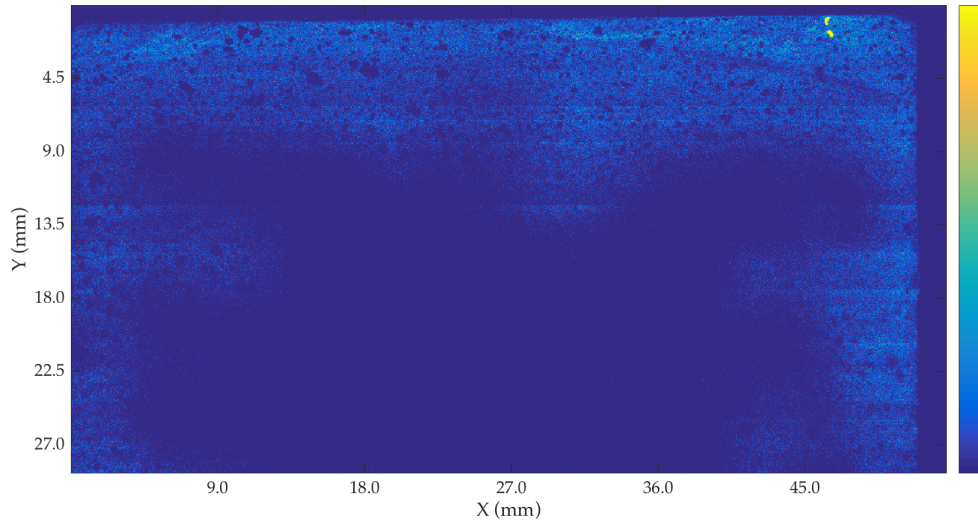
Figure 4.25: Qualitative chloride map of sample M02-1 (M02(c) in fig. 4.22). The chloride ingress is from the top of the picture (0.045 mm per pixel). The color bar represents the intensity of the grey scale, meaning this map is only qualitative (blue means no chlorides, whereas yellow means the highest chloride contents).
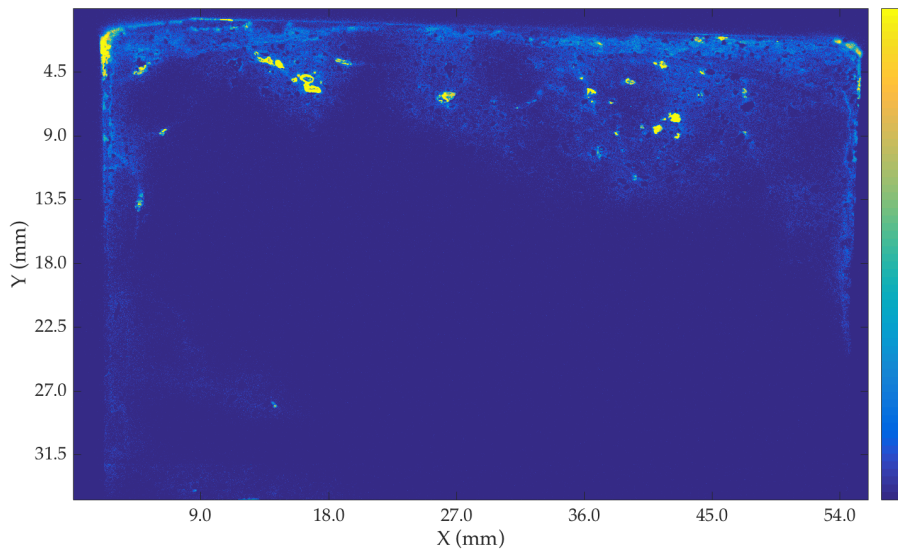
Figure 4.26: Qualitative chloride map of sample M03-1 (M03(a) in fig. 4.22). The chloride ingress is from the top of the picture (0.045 mm per pixel). The color bar represents the intensity of the grey scale, meaning this map is only qualitative (blue means no chlorides, whereas yellow means the highest chloride contents).
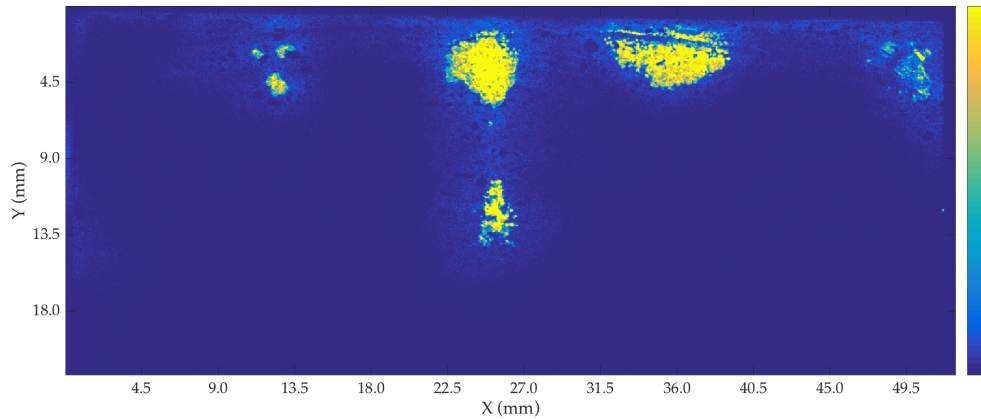
Figure 4.27: Qualitative chloride map of sample M02-3 (M02(b) in fig. 4.22). The chloride ingress is from the top of the picture (0.045 mm per pixel). The color bar represents the intensity of the grey scale, meaning this map is only qualitative (blue means no chlorides, whereas yellow means the highest chloride contents).

4.4. Discussion

4.4.1. Diffusion experiment

The results of the diffusion experiment make qualitative sense in terms of measurements by the sensors since they show:

- Decreasing concentrations from the outer to the inner parts of the samples

- Maximum concentrations that do not exceed the concentration of the storage solution

- Faster ingress in the high w/c than in the low w/c samples

However, different issues in the experiment prevent a more quantitative analysis of these results and a connection thereof to the total amount of accumulated chlorides through a transport model.

107

The first issue is due to the discontinuities in the free chloride measurements after the storage solutions were replenished. These jumps are tentatively attributed to diffusion potentials, which result from differences in ionic concentrations, such as chloride concentration or pH gradients, and from differences in ionic mobility of the ions present [40,98,99]. Even small pH differences have strong influences on these diffusion potentials [99]. Diffusion potentials are rapidly felt throughout the measuring circuit (that is between the reference and the ion selective electrode) before mass transport is really affected. In other words, through this phenomenon, the sensor measurement is instantaneously affected when concentration gradients suddenly change during the experiment. Here, such changes in exposure solution chemistry occurred every time when the exposure solution was replaced with a new one. This explains that the potential drop (or jump in the concentration) occurs at the same time throughout the sample, independently of their radial positions. As it is shown in these results, the magnitude of the potential drop increases with decreasing w/c ratios, which may be explained by differences in permselective properties of the porous matrices [40,99]. Temperature is excluded as a possible cause of this, because the samples were stored at room temperature.

Unfortunately, the effect of the diffusion potential means that there are some concerns about how to quantitatively analyze these results, thus compromising their use in any transport model.

Another limitation in these experiments is segregation, which is most apparent in the samples prepared at the highest W/C. These effects are attributed to segregation and bleeding, but it is emphasized that the bleeding layers were not visible until the maps were created. As the maps show, the segregation greatly

affects the results and can produce highly misleading results if the free chloride sensors are affected by those fast chloride transport channels. To support this interpretation, electron microscope images have been obtained of the bottom and top parts of these samples (Figure 4.28 and Figure 4.29 respectively). Based on their average grey scales, these images show that the porosity is relatively similar on the top and bottom of these samples. However, they also show bands of higher porosity, which are present both at the top and the bottom of the samples, although somewhat more pronounced at their top. Unlike the findings in the study by Massousi et al [100], these bands correspond to horizontal layers in the samples. They may represent collapse events of the flocculated microstructure between casting as final setting.
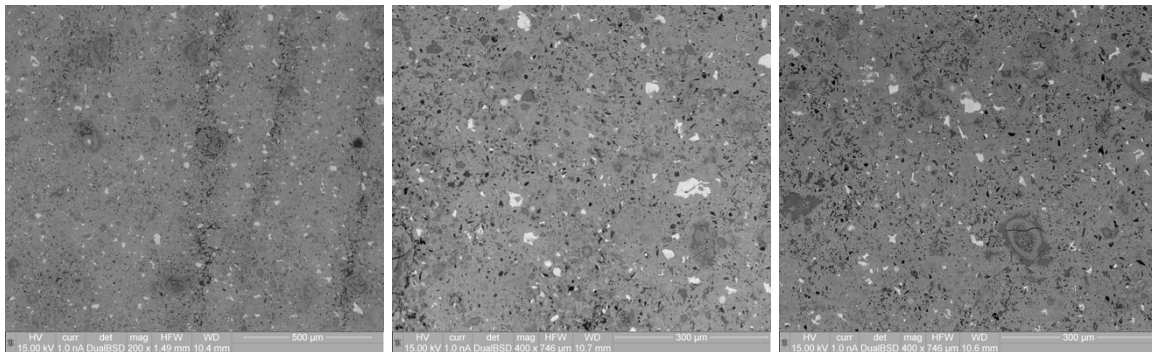
Figure 4.28: SEM images for a sample taken from the bottom portion of a WC1 specimen. The orientation of the "porosity bands" is perpendicular to the casting direction.
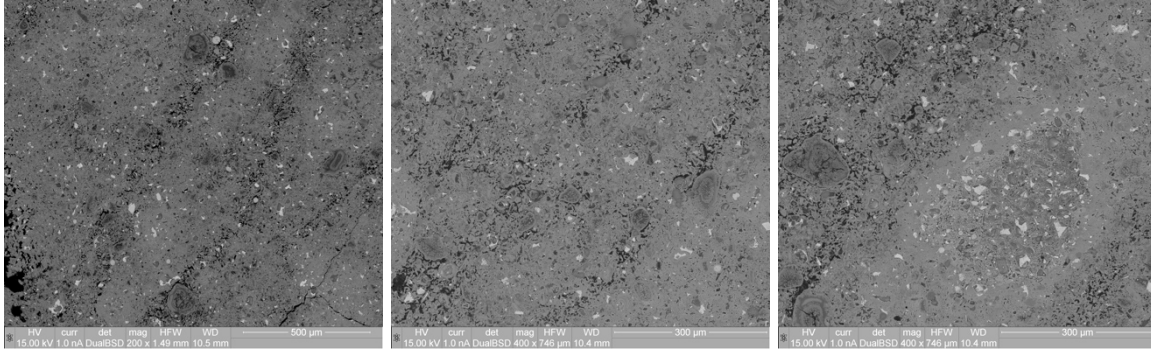
Figure 4.29: SEM images for a sample taken from the top portion of a WC1 specimen. The orientation of the "porosity bands" is perpendicular to the casting direction.

Though more analyses and characterization are required to confirm the reason for the formation of these bands, we can already say that these channels of higher porosity explain the faster ingress of chlorides that has been observed in these samples. They act as "chloride diffusion highways". While interesting and far reaching, this result also compromises the initial objective of using these a priori simple experiments to test or refine chloride transport models.

We are not aware that the type of segregation reported here has already been reported elsewhere and believe that it can potentially have major implications for the durability of cementitious systems, particularly pastes or grouts. In a broader sense, this result has important implications for the next chapter in which the role of cold joints in 3D extrusion based printing is studied.

4.4.2. Capillary rise experiment

As already indicated, the reproducibility of the free chloride measurements in the capillary rise experiments was not achieved. Additionally, the free chloride concentrations obtained were much higher than those in the exposure solutions. These issues are attributed to streaming potentials, which, in this setup, acted as

a major error source for the potentiometric chloride measurement. In this case, interaction between the pore wall surface charge and the charges of the ions moving through the pore system, gives rise to an additional potential difference in the measuring circuit, that is, in addition to the cell voltage and diffusion potentials mentioned previously [98,99,101]. The diffusive part of the double layer is rather mobile and therefore moves when the solution is forced through the sample, resulting in a potential difference, referred to as a streaming potential. This can seriously perturb the potentials measured by the ion selective electrodes and thus compromises their reliability in capillary rise experiments. This should be considered if such ion selective electrodes are to be used in situations where the level of water saturation in concrete changes rapidly over time, and where the reference electrode is positioned relatively far from the ion selective electrode.

In terms of micro-XRF on these samples, we have attempted to examine whether the mapping was consistent with the measurement of mass of solution entering the sample. For this, different approaches have been taken and are described below.

First, the micro-XRF mapping was examined to separate out the sample in zones containing chlorides and zones not containing chlorides. Then the volume was geometrically defined using objects with axial symmetry. An example is illustrated in Figure 4.30. Taking the difference with the considered sample volume gives us the volume in which solution has entered.
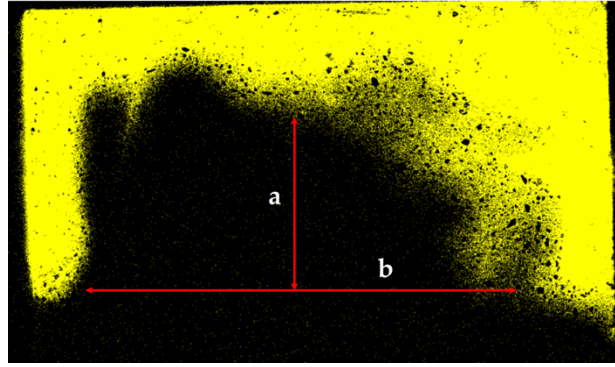
Figure 4.30: Example of the volumetric subtraction approach. The image represents the chloride map of sample M01-1, where the brightness of the gray scale was enhanced to reveal all the points where chlorides were mapped. The chosen volume was a half prolate ellipsoid with axes a and b, where the volume was calculated with formula: $V_e = \frac{2}{3}\pi a^2 b$. The total considered sample volume is calculated using known dimensions and the distance to where chlorides are visible.

Using this volume of sample in which solution entered, and together with the non-bound water measurement used to determine the porosity of the mortar, the amount of solution that entered the sample was calculated. Results compared very advantageously with volumes inferred from the sorptivity experiments as shown in Table 4.6. Considering the rough estimate of the volumetric difference, this good agreement indicates that even if Friedel's salt formation may take place in the sample as the solution ingresses, the liquid front is not fully depleted of chlorides (see especially Figure 4.23). In other words, with respect to rates of capillary ingress, the rate of Friedel's salt formation is slow. This result has potentially far reaching implications for the prediction of service life of reinforced concrete structures because many transport models are often coupled with chemical equilibrium models that assume a very fast formation rate of Friedel salt. In cases of diffusion transport however, we expect the situation to be different. There, the rate of Friedel's salt formation ought to be much faster than

diffusion transport. Because of the potential major implication of this result, further investigations on this issue would are needed.

Table 4.6: Summary of the calculated volumes of the solution in selected samples. The volume that was calculated using the volume subtraction described earlier is denoted as $V_{S,vol}$, and the volume calculated from the sorptivity experiments is denoted as $V_{S,sorp}$. For comparison reasons, the percent difference is calculated and presented in the table.

Sample	$V_{S,vol}$ (cm^3)	$V_{S,sorp}$ (cm^3)	% difference
M01-1	14.8	13.1	11.4
M01-2	12.0	7.6	36.4
M02-1	14.8	18.3	23.9
M03-1	13.1	10.2	22.0

The other approach to compare the solution ingress with the micro-XRF measurements was to determine the total amount of chlorides from the maps. Because the quantitative maps were not fully retrievable, the grey scale images were used as follows. First a baseline grey scale was determined in an area where it could be assumed that there were no chlorides. Second, the grey scale sum was determined over the whole image and was corrected for the baseline signal. Third, the corrected grey scale was determined at a specific location for which local quantification was also carried out using the instrument software. Using the corresponding proportionality, the amount of chlorides over the whole sample area could quantitatively be assessed. With this, the solution volume could be calculated using its concentration, the samples' dimensions, and the cement volume fraction in the mortar.

Here in contrast to the previous approach, the estimated solution volume was in some cases up to 8 times higher than the values calculated in Table 4.6. We still

suspect that some instrumental issue may explain this, but so far any issues have not been identified. Our most probable interpretation is that the sample surface may have been enriched by the drying that it underwent during the measurement in the micro-XRF, which could last > 40 hours. The fact that mortars are used here rather than pastes, unlike for the calibration, most probably explains this discrepancy. Further research on this issue would be needed, in particular to determine the most appropriate drying protocols to avoid such artifacts on concrete cores. Despite this shortcoming, the fact that the chloride containing zone was consistent with solution ingress indicates that the mapping reliably determines the chloride ingress front. However, the quantitative reliability of the maps in terms of absolute chloride contents is a topic that still needs further research.

4.5. Conclusions

The original intent of the work presented in this chapter, was to get a deeper insight into chloride transport mechanisms using the method described in Chapter 3 coupled with measurements of free chlorides using the chloride specific electrodes developed by Segui et al. [40,41,90]. A series of inconclusive prevented us from achieving this goal. Nevertheless, in the spirit of promoting an unbiased scientific community, and as precaution for future research, these negative results were presented.

The diffusion experiment makes qualitative sense, but various experimental issues prevented from uniting results from micro XRF and free chloride sensors. The micro XRF mapping revealed inhomogeneities in the samples that would otherwise not be visible nor detected. The odd movement of chlorides at the

top/bottom of the samples revealed that porous bands formed, probably as a consequence of segregation. This result can have major implications for the durability of cementitious systems, in particular, the detection of preferential pathways that can arise in the formation of cold joints in 3D extrusion based printing of concrete, which are discussed in the next chapter.

In the case of the capillary rise experiment, the original intention was to use the fast process of capillary rise to perhaps help characterize the kinetics of Friedel's salt formation. While a quantification was not possible, our experiments do however suggest that Friedel salt formation is not faster than capillary ingress. This result is important because many transport models implicitly assume a very fast formation rate of Friedel salt [102]. Because of the potential major implication of this result, further investigations on this issue would be needed.

Chapter 5 – Chloride Ingress Through Cold Joints in Digitally Fabricated Concrete

5.1. Introduction

The Economist magazine deems digital fabrication a revolutionary step in manufacturing [42,103]. Unlike the digitization of the virtual world, in which communication and computation were implicated, digital fabrication refers to the digitization of the physical world. In recent years, it has been gaining more and more popularity in the manufacturing field, as it provides an easy and convenient technique to apply digital modeling and technologies to the production of custom, tangible objects on demand [42,104]. One of the newest applications gaining popularity in the last few years for this technology has been developed in the field of architecture and construction, since it promises faster construction, lower costs in terms of labor and formwork, and also better worker safety [42,105]. This is because the technique allows for a more precise material placement, and more efficient construction practices. Moreover, because

formwork is not needed for digital fabricated concrete, it could also contribute to a reduction in waste generation in the construction field.

The above described technique has also been called digital construction [43]. As is discussed in detail in [42], this can be divided into two categories: form filling and additive manufacturing. This chapter focuses on a subcategory within additive manufacturing, namely 3D printing or extrusion printing. This represents the most popular digital fabrication technique [42,104,106]. A brief description of how concrete is 3D printed is found in Chapter 2, section 2.3 (see Figure 2.5,).

Extrusion-based 3D printing is a layered process, and it is a well-established manufacturing process in fields such as aerospace and medical fields [104] that works well for polymeric materials in which material is extruded in the liquid or plastic state that later hardens, analogous to concrete. Although 3D printing of polymer composites has undergone significant developments in recent years, several limitations still prevail [104]. Firstly, material properties play a significant role in the capacity to 3D print an object. The technique also introduces some mechanical properties issues, in that voids can be present in the 3D printed parts. Third, the manufacturing of the appropriate printing machines poses another limiting factor. These limitations and challenges are of course inherited by concrete 3D fabrication, and as a consequence they are being widely investigated by several researchers [42,44,104–108].

Although it is true that digital fabrication in the construction field has great potential, some questions are still open and are yet to be thoroughly explored. One aspect that has only recently been looked at, is the effect of the quality of the layered concrete interfaces. Nerella et al [43], are some of the first researchers to

look at the effect of a weak interface or the formation of cold joints between printed layers, on the mechanical performance of 3D printed cementitious materials. The layer interface was investigated on micro and macro scales, where material composition and time intervals between placements of subsequent layers showed an obvious influence on the quality of the interfaces, which in turn influenced the mechanical properties of the material [43].

The time intervals between layers is finite and variable depending on printing speed and contour length. This, together with the material structuration rate, potentially has a clear effect on the interface between layers [42]. This was proven in [43] in terms of the mechanical properties of 3D printed concrete. However, the importance of such phenomenon and its impact on durability remains an open question. As previously mentioned, the material composition is known to have a strong influence on concrete's durability [2–4,6,89,109], and in the case of digital fabrication, this is no exception. Rather the sensitivity to the material is probably exacerbated. Thus, on top of concrete's identifiable issues in terms of durability, the additional effect of formation of cold joints needs to be addressed and investigated for digital fabrication.

In this chapter, the issue of layer interfacial effects on moisture and chloride ingress is studied in a qualitative way. The ingress of chlorides is qualitatively compared to moisture ingress. For the first time, we show the great importance of the method presented in Chapter 3, for an application to a relevant case where it is crucial to obtain a spatial resolution of the chloride distribution in a sample's cross section. The chloride ingress is qualitatively considered in 3D printed mortar samples.

The work was part of a collaboration with TU Dresden who produced 3D printed samples, a parallel study of moisture ingress was conducted as well and is partially reported in [109]. The work carried out for this PhD specifically related to analyzing chloride ingress. The moisture ingress measurements were led by Dr. Timothy Wangler from ETH Zurich (same group) in the context of this collaboration. Because both contributions are closely linked to the work produced for this thesis, their experimental details are also reported, and clearly identified. A paper is in planning for which the author of the present thesis is planned to be the first author.

5.2. Materials and Methods

5.2.1. Materials for the 3D printed samples[3]

Portland cement (certified CEM I 52.5 R, after Standard SN EN 197-1) was provided by OPTERRA (OPTERRA GmbH, Leipzig, Germany). Aggregates were provided by Kieswerk Ottendorf-Okrilla (Kieswerk Ottendorf-Okrilla GmbH & Co. KG, Laußnitz, Germany). Micro silica suspension (50 wt % aqu. Suspension, EM-SAC 500 SE, Elkem), fly ash (class F, Steament H-4, STEAG), and a high range water reducing admixture (SKY 593, BASF) were also used. The mix proportions are presented in Table 5.1

---

[3] Information provided by TU Dresden

Table 5.1: Mix proportion for all 3D printed samples [kg/m3].

Material	Content
Portland cement	378.4
Micro silica	206.4
Fly ash	206.4
Fine sand (0.06-0.2 mm)	316.3
Sand (0 – 1 mm)	278.0
Sand (0 – 2 mm)	717.3
Water (w/c = 0.42)	133.7
Water reducing admixture	10.32

5.2.2. Materials for the chloride exposure

Sodium chloride (NaCl for analysis EMSURE ®, ACS ISO, reag. Ph. Eur., Merck KGaA, Darmstadt, Germany), as chloride source. Sodium hydroxide (Sodium hydroxide pellets, analytical reagent grade, conforming to BP, EP; $\geq 98.3\%$; Fisher Chemicals, New Hampshire, USA), and calcium hydroxide (calcium hydroxide for analysis, puriss. p.a., Reag. Ph. Eur., 96%, Sigma-Aldrich, Missouri, USA) were used for the chloride solution to which the samples were exposed.

5.2.3. Preparation of 3D Printed samples[3]

3D printed samples were received ready for exposure as it is shown in Figure 5.1. They were mixed and cured by a group of researchers from the Institute of Construction Materials at the Technical University of Dresden in Germany. The mortar specimens were mixed according to DIN 12390-2 [110]. The water to

binder ratio was 0.42 for all samples. The mortar was used to print wall elements, which was constructed by layered extrusion 3D printing, in which a digitally controlled nozzle extruded concrete layer by layer [43,111]. The samples were then obtained from these walls, by cutting them into $4 \times 1 \times 2.5 \text{ cm}^3$ pieces, giving each sample 2 interfaces (3 layers) along the 4-cm edge (see Figure 5.1).
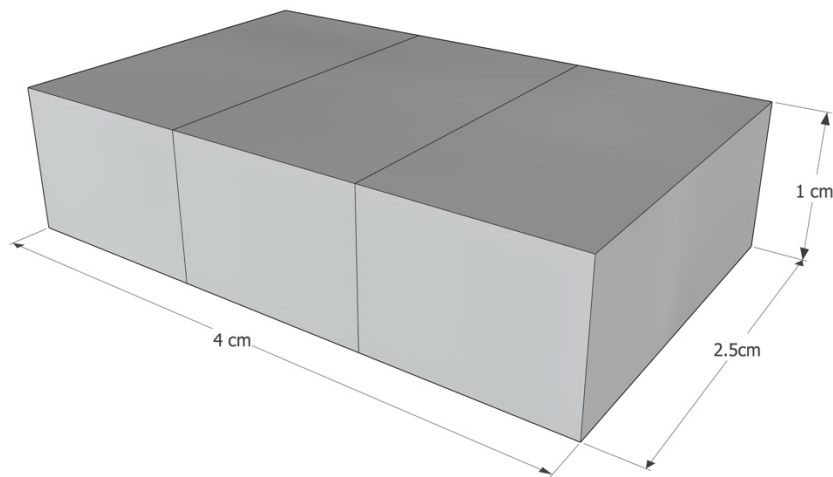
Figure 5.1: Dimensions of printed elements. Layer-interfaces are shown as lines in the figure. The face to be exposed to chlorides is the long face (4 by 1 cm^2).

Three groups of samples were prepared, where the printing interval was varied to study its effect. The first group has a 13-minute interval between layers. The second group has a 2-minute interval, and the last group has a 2-minute interval for the first interface (1st layer – 2nd layer), and a 24-hour interval for the second interface (2nd – 3rd layer). A summary of the time intervals for each sample is presented in Table 5.1.

Table 5.2: Summary of sample classification. For each sample the time interval between interfaces and the curing conditions are given. Condition P, has no drying conditions during the last week, whereas condition Q includes a 3-day drying condition at 40 ℃ at the end.

Sample	Interface time interval [min]	Curing conditions
A29	13	P
A30	13	P
A35	13	Q
A36	13	Q
A44	2	P
A45	2	P
A50	2	Q
A51	2	Q
A59	1440	P
A60	1440	P
A65	1440	Q
A66	1440	Q

Another varying parameter was the curing condition. The curing of the printed elements was carried out according to DIN 12390-2 [110]. Two options were chosen for the last week of curing (see Table 5.1). The curing process of the samples included a week of underwater curing, 2 to 3 weeks of high relative humidity curing, and in the case of a group of samples, 76 hours of curing at 40°C. See Figure 5.2 for a graphical representation of the curing process.

Production	Curing under water	Curing (20°C, 65% RH)	Curing (40°C)
• P: 0-100 min • Q: 0-100 min	• 2nd day - 8th day • 2nd day - 8th day	• 8th day - 28th day • 8th day - 21st day	• - • 21st day - 24th day
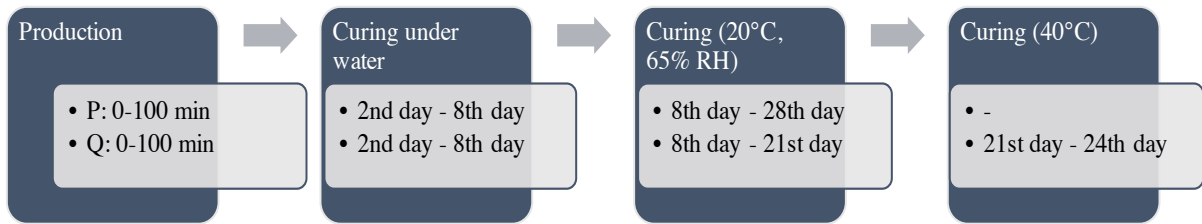
Figure 5.2: Graphical representation of the curing process for the printed specimens. Process P, has no additional drying conditions during the last week, whereas process Q includes a 3-day drying condition at 40 °C.

As a comment to this experimental description provided by TU Dresden, we underline that the stage 3 curing at 20°C and 65% RH also should be considered as a drying stage leading to a loss of capillary water. This is important for what follows as the samples are not further dried before capillary rise experiments for chloride ingress or water mapping by neutrons.

5.2.4. Chloride exposure

The samples were exposed to chlorides by means of capillary rise. They were not further dried than as received, since the curing steps described include such a stage (see comment at end of in section 5.2.3). The experimental setup is basically the same as for a sorptivity experiment. The samples were suspended from a balance, and one of the faces with the two interfaces was in contact with a solution containing the chlorides schematically shown in Figure 5.3. The exposure solution consisted of 1 M NaCl + 0.1 M NaOH + sat. $Ca(OH)_2$. The experiment was run for 24 hours, after which time the samples were dry cut,

perpendicularly to the exposed surface. Stopping the experiment and cutting the sample was done the morning right before starting the micro XRF mapping.
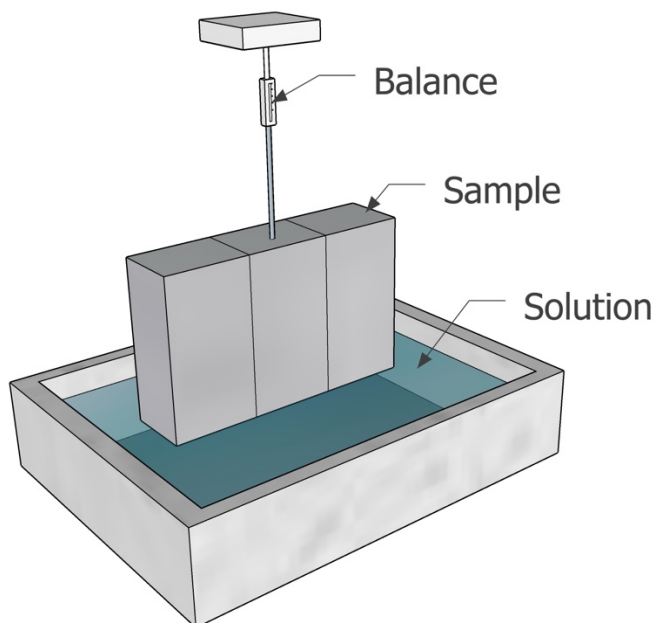
Figure 5.3: Schematic representation of the surface exposed to chlorides. The samples were suspended from a balance that recorded the mass increase of the specimen resulting from absorption of the solution. No preconditioning was performed on the specimens prior to chloride exposure.

5.2.5. Moisture ingress by neutron imaging

Similarly to the chloride ingress, samples were not further dried than as received, since the curing steps described include such a stage (see comment at end of in section 5.2.3). Samples from the same sample group were measured at the NEUTRA beamline, at the SINQ spallation neutron source in the Paul Scherrer Institute, Villigen Switzerland [112]. The Swiss ring cyclotron produces a proton beam which strikes a lead target and produces a steady neutron beam, and the high absorption capacity of hydrogen allows for qualitative and quantitative

moisture distribution imaging. A protocol similar to that seen in [111] was used, except position 2 was used for higher resolution in the small samples. Samples were oriented similar to Figure 5.3, with moisture ingress occurring parallel to the layer interfaces, and the neutron beam passing through the sample in the same plane that they were mapped for chlorides. Samples were run for 3-8 hours, depending on scheduling and strength and consistency of the proton beam that determined the strength of the neutron source. This time is generally adequate to see high differences in capillary sorption of moisture along these layer interfaces. Only four samples were able to be imaged during the time due to the inconsistency of the beam: those corresponding to the 2 minute layer interval and the 24 hour layer interval, with both curing conditions. Details of the measurement setup and post-processing are provided in the following section.

5.2.6. Instrumentation

5.2.6.1. Micro XRF

The measurement protocol was the following: The relatively freshly cut surfaces of the samples were mapped with a 45 μ m resolution. The applied acceleration potential and current were 35 kV and 950 μ A, respectively. At each point, a spectrum was acquired for 150 ms. Measurements were carried out in air with a built-in 25-μ m thick aluminum filter to eliminate the rhodium L α radiation and, therefore, preventing it from reaching the sample. This is necessary because this radiation overlaps with the chlorine K α X-ray line and increases its limit of detection.

5.2.6.2. Neutron imaging and analysis

The samples were held within an aluminum receptacle (as aluminum is comparatively transparent to neutrons), laid on two small wires. The sample and frame were placed in measurement position 2 at the NEUTRA beamline [113]. Neutrons that pass through the sample strikes a scintillation screen, where it is transformed into visible light, which is directed to a CCD camera. The sample was first imaged with no moisture to get a baseline; approximately 10 images were taken. Then an automatic titration system deposited water in the aluminum frame until it touched the bottom of the sample, and the wetting experiment started. During these experiments, images were taken every 12 seconds. The duration of an experiment was usually between 3-8 hours.

Images were analyzed in the open source image analysis program ImageJ [114]. Before any analysis took place, all images were treated to reduce noise by first removing bright outliers, then using the despeckle feature in ImageJ to smooth out any other noise as much as possible. The first 10 images of the dry sample were then averaged to form a dry reference image. Next, the difference between this reference image and all images taken after the initiation of wetting was taken, and towards the end of the wetting an image with comparatively low noise was selected as a representative image of the end of the wetting experiment. Within this time frame, this was adequate to see if there was preferential uptake along the layer interfaces. In the NEUTRA beamline, for the conditions of this experiment, resolutions would be on the order of 50 microns.

5.3. Results

5.3.1. Chloride maps

Chlorides maps were collected for all samples, however due to time constraints, not all maps are of the same size. In order to keep the same resolution for all maps, some maps needed to be smaller than others. Still, if it deemed necessary, the area of the map was chosen to include all regions of interest. Figure 5.4 shows the chlorine maps for samples A29 through A51, corresponding to the 2 and 13 minutes time interval samples (also refer to Table 5.1).

As seen in Figure 5.4, no clear cold joint is visible even though the layer interfaces are somewhat recognizable in some of the samples (e.g. A29, A30, and A50 and A51). Another visual evidence is the difference in chloride penetration depth. In samples A29, A30, A44 and A45, the penetration depth is visibly smaller than for the rest of the samples.

Figure 5.5 shows the chlorine maps for the rest of the samples. These samples represent the four cases in which one of the layered-interface had a time interval of 24 hours. These samples show the worst conditions in terms of penetration depth of chlorides. Also, apart from sample A66, they all exhibit a clear cold joint. Sample A65, even contained a large cavity in the interface to the left, which was not visible until the sample was cut. And sample A60 shows by far the worst conditions. The chloride solution went all the way through the cold joint, and it showed some efflorescence after the experiment was stopped (see Figure 5.6).
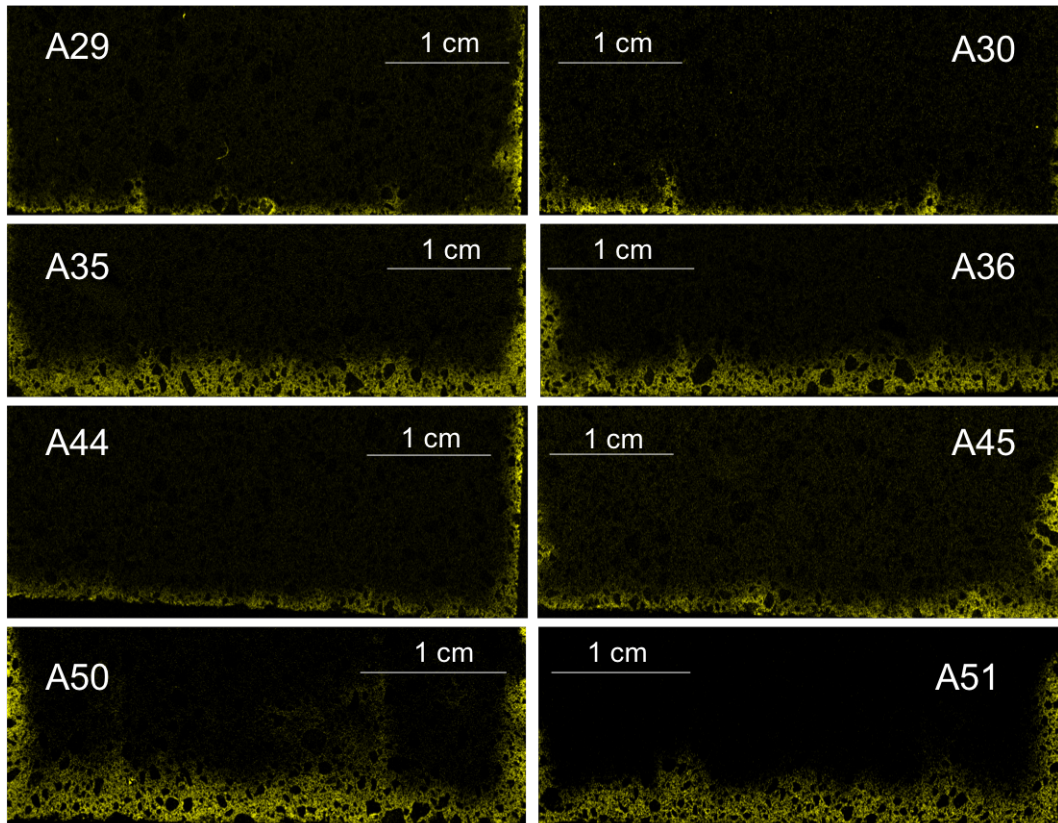
Figure 5.4: Micro XRF chlorine maps for samples A29 through A51. The bottom of each image represents the direction in which the chloride solution penetrated. Each map has a slightly different size, thus each of them has its own scale.
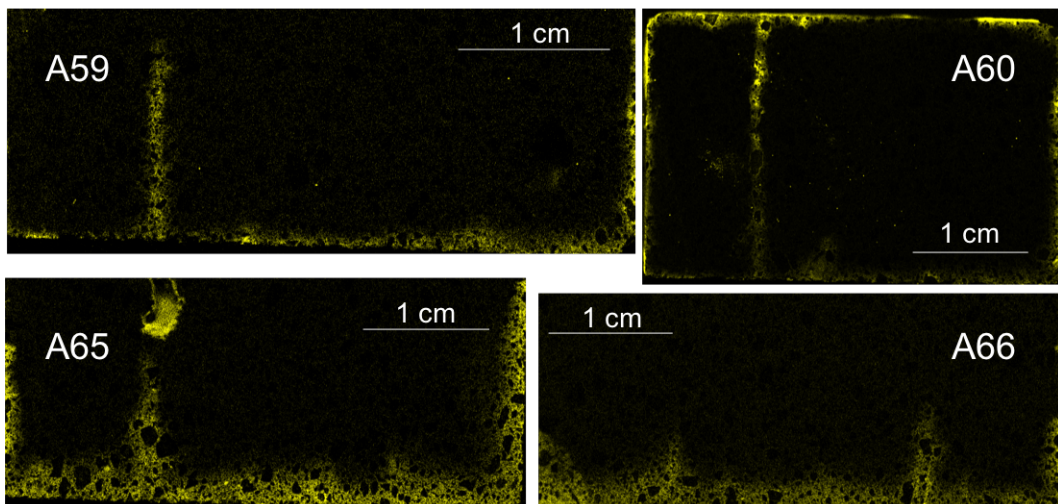
Figure 5.5: Micro XRF chlorine maps for samples A59 through A66. The bottom of each image represents the direction in which the chloride solution penetrated. Each map has a slightly different size, thus each of them has its own scale.
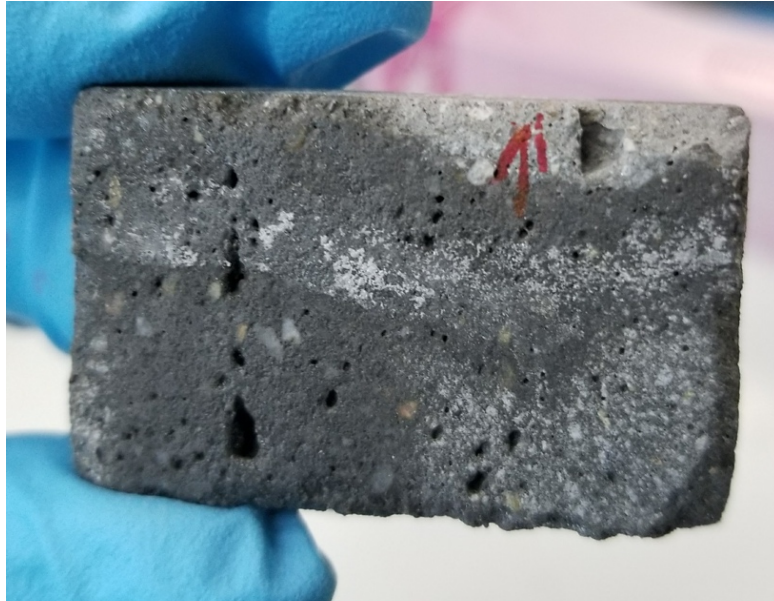
Figure 5.6: Efflorescence in sample A60, as it was after the sorptivity experiment was stopped. The red arrow indicates the top of the sample. After visual inspection, it was decided to make a chemical map of the entire sample.

5.3.2. Neutron imaging of moisture

Figure 5.7Figure 5.8 give qualitative results of the moisture ingress. Each set of images shows the dry reference image for a particular sample on the bottom, and the projection difference image on the top. Figure 5.7 corresponds to both curing conditions for the samples with the 24 hour delay (on one interface, the other interface had 2 minutes delay). Figure 5.8 corresponds to both curing conditions for samples with only a 2 minute delay.
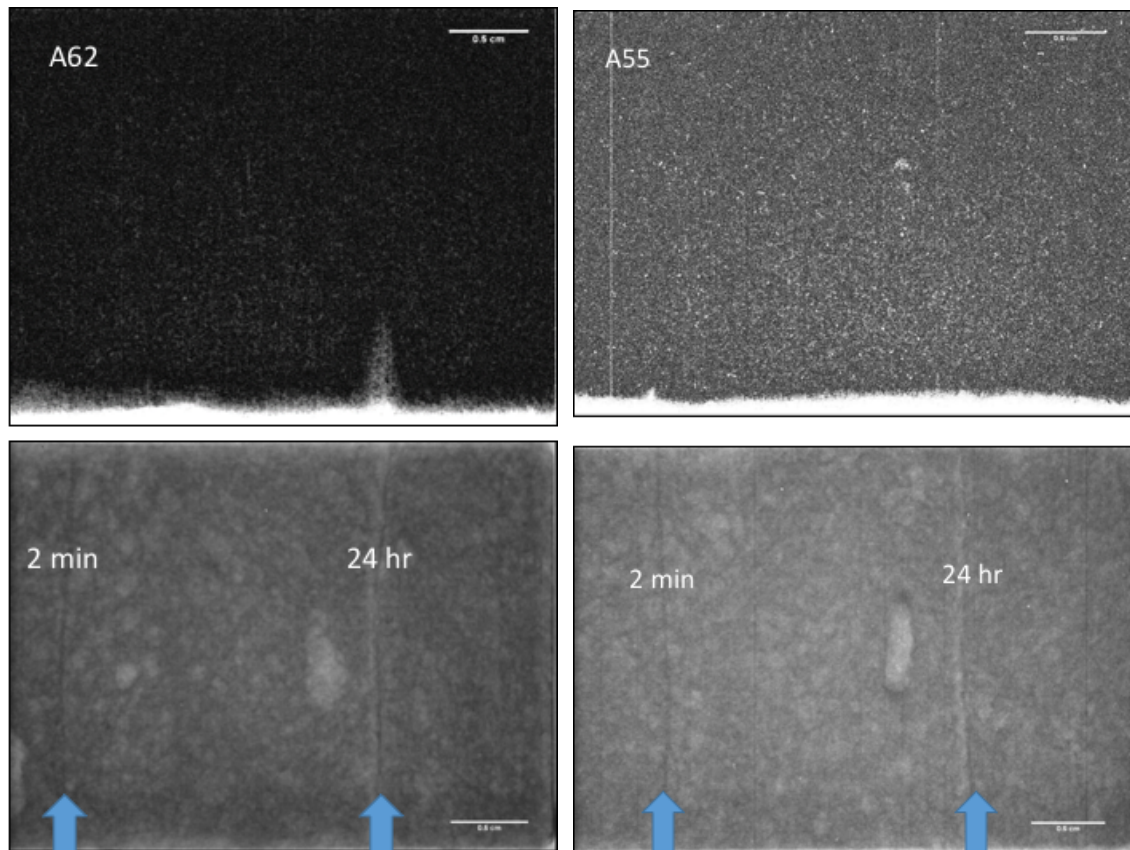
Figure 5.7: Image projection difference profiles (top) and dry reference images (bottom) for samples A62 and A55, which correspond to dry curing and wet curing, respectively. White areas in projection difference profiles correspond to areas of high moisture ingress. Blue arrows on dry reference images indicate location of layer interfaces, and waiting time between layers is indicated on image. Scale bars are equal to 0.5 cm on all images.
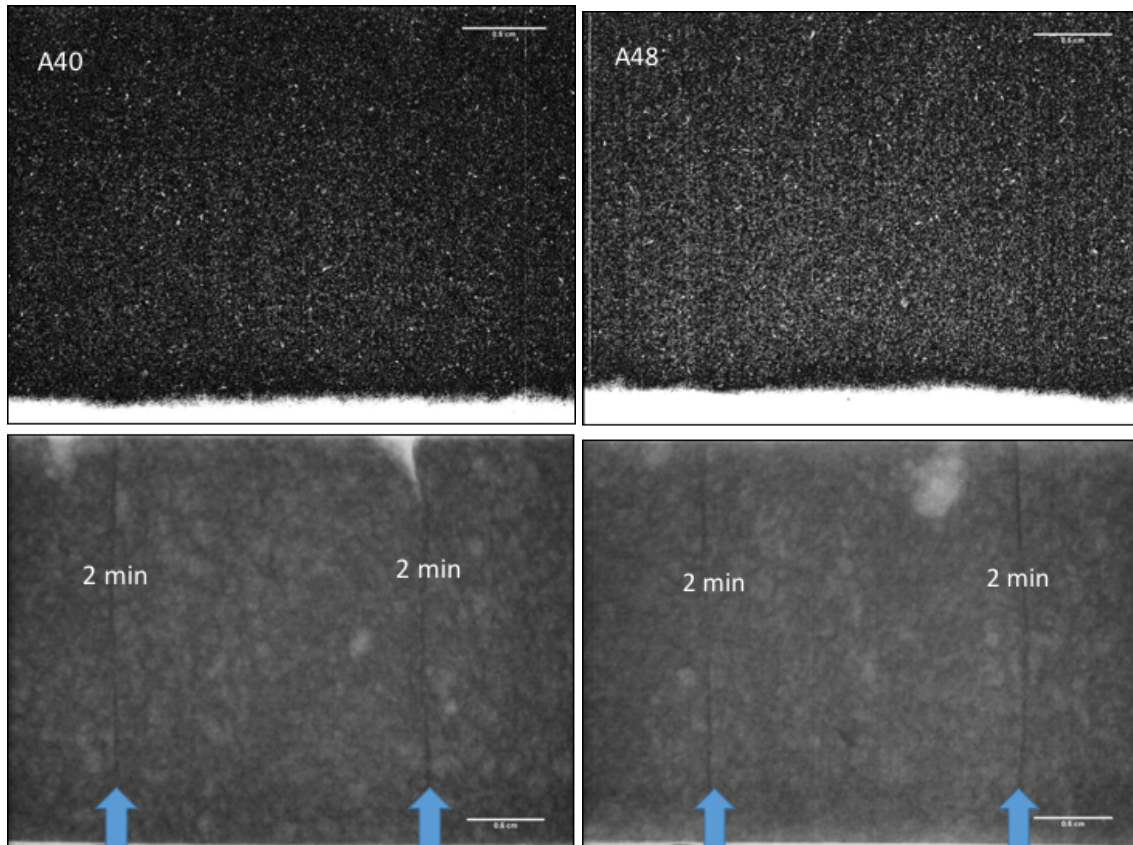
Figure 5.8: Image projection difference profiles (top) and dry reference images (bottom) for samples A62 and A55, which correspond to dry curing and wet curing, respectively. White areas in projection difference profiles correspond to areas of high moisture ingress. Blue arrows on dry reference images indicate location of layer interfaces, and waiting time between layers is indicated on image. Scale bars are equal to 0.5 cm on all images.

One can observe from these images that only the 24 hour delayed sample that was cured in an environment where it could dry out showed significant moisture ingress along the layer interface. This is in correspondence with [111].

5.4. Discussion

A recent study [43], clearly indicated that interfaces are present between layers of 3D printed mortar specimens. It was more evident in some cases than in others, but it all came down to the time intervals between the placement of subsequent

layers. Hence, the time interval has a significant influence on the quality of the interfaces or the bonds between layers [43,115]. As reported by Le et al [105], the interlayer strength is inversely related to the time interval, meaning that it is expected to decrease as the time interval increases.

The significance of the influence of the time interval between layers on the penetration depth, was not as strongly evident as the influence of the curing conditions. The 3-day drying period at 40°C in curing condition Q, made a difference in the depth of chloride and moisture ingress. This is of course not a surprise, as the drying condition would remove more water from the pores than the 65% curing to which the other samples were exposed, thus explaining the increase in the capillary rise of the Q-cured samples.

The results of the neutron imaging experiments partially corroborate the results of the chloride maps, but seemingly with less resolution. Only the 24 hour interface with an accelerated drying curing condition showed any moisture penetration, whereas the chloride ingress experiments were able to image chlorides entering in some interfaces at other layer interface waiting times. The fact that the chloride experiments lasted for 24 hours, versus 3-8 hours for the moisture transport, could have been a factor. In any case, the chloride mapping method seems to be better able to detect transport in interfaces, probably due to the fact that the neutron imaging method requires a certain amount of moisture across a particular cross section to ensure that an appropriate signal can be seen, and this could be smaller than that required for the chloride mapping method. Also, the chloride mapping method is much easier to perform, and with less expensive equipment, all the while imaging a species that is of chief concern in concrete durability.

There was however a somewhat contradictory result in terms of the effect of the time interval on the chloride ingress. If we examine the samples with curing condition Q in Figure 5.4 (A35, A36 and A50, A51), even though the samples show a considerable depth of penetration, the interfaces are less visible for samples with a longer interlayer time interval (A35, A36). If on the other hand, we examine the samples with curing condition P, (A29, A30 and A44, A45), the opposite can be observed. The penetration depth is small in both cases, but the samples with a longer time interval (A29, A30) show a more pronounced evidence of the interfaces between layers. This occurrence is in line with the discoveries of Sanjayan et al [115], where they reported that, in contrast to [105], interlayer strength does not necessarily decrease with increasing time interval, but it depends more on the amount of moisture on the surface of each extruded layer. They reported that (for their particular mix) the moisture level on the surface first decreased, and then increased with increasing interval times. This was also observed for the interlayer bond strength. Perhaps, this phenomenon is also valid for the mix studied in this chapter.

Though more analyses are required to corroborate this principle for this particular mix, as a first approximation the difference of the penetration depths was estimated using the chloride maps. The percent difference was calculated as seen in Figure 5.9. The calculation was done for each peak. Ten measurements were made for each depth in order to obtain an average value for D_{P1}, D_{P2} and D_B. The results of this rough calculation are presented in Figure 5.10.
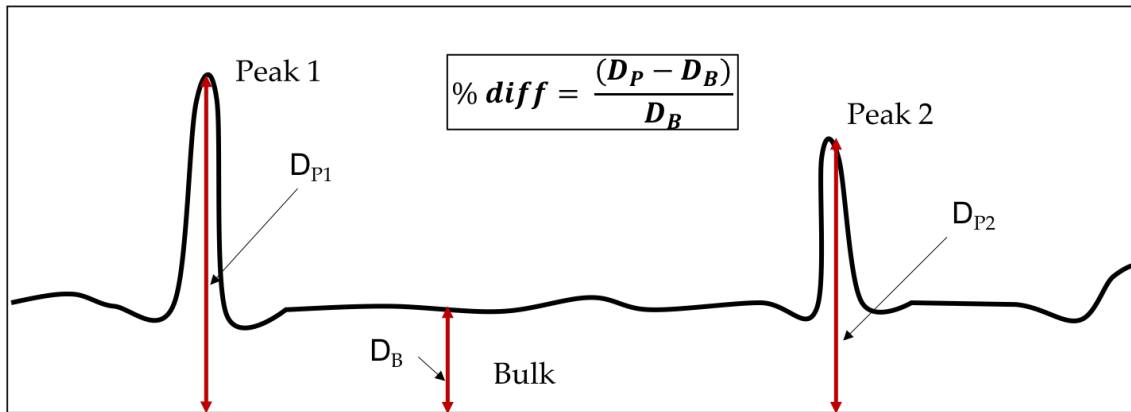
Figure 5.9: Sketch of a typical chloride ingress pattern where the ingress at joints are visually different than the bulk ingress.
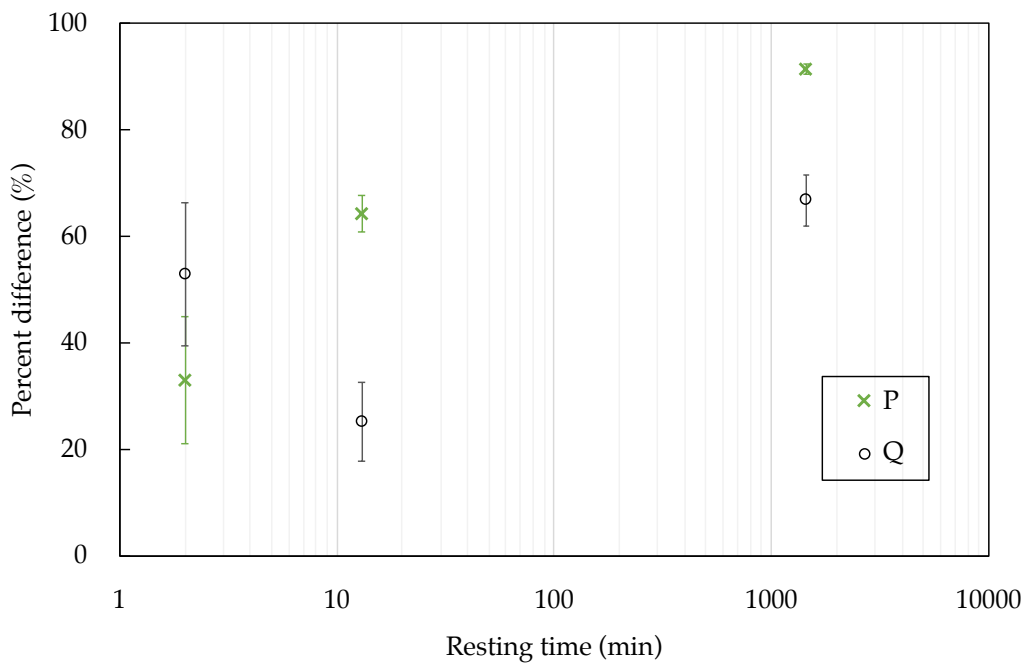
Figure 5.10: The percent difference between interface penetration depth and the bulk penetration versus the time interval between layers. The 'x' symbols represent the samples with curing condition P (curing / drying at 65% RH and 20°C), and the hollow circles are the samples with curing conditions Q (extra 3 day drying period).

As can be seen from Figure 5.10, the percent differences are more scattered for the samples with a 2 minute time interval than for the 13 minute interval. This suggests that there is something more than just the time interval that affects the difference in the penetration depths. Additionally, the curing conditions have a significant effect for samples with a 13 minute interval. While the drying condition at the end of curing leads to larger penetrations depths, the difference between the bulk and the layered interfaces is not so pronounced. Nerella et al [43] performed strength tests on similar samples to the ones being investigated here (with a curing regime similar to "P"), and they found that the flexural strength difference (calculated as the difference between the normal-to-interface flexural strength and the parallel-to interface flexural strength over the normal-to-interface flexural strength) does not linearly increase with increasing time interval, but it is rather a logarithmic relationship (see Figure 5.11). The time intervals are too far apart for us to directly compare to the results of [115], however the non-monotonic behavior does suggest that there is something other than simply the time interval at play.

$$y = 1.8\ln(x) + 10.0$$
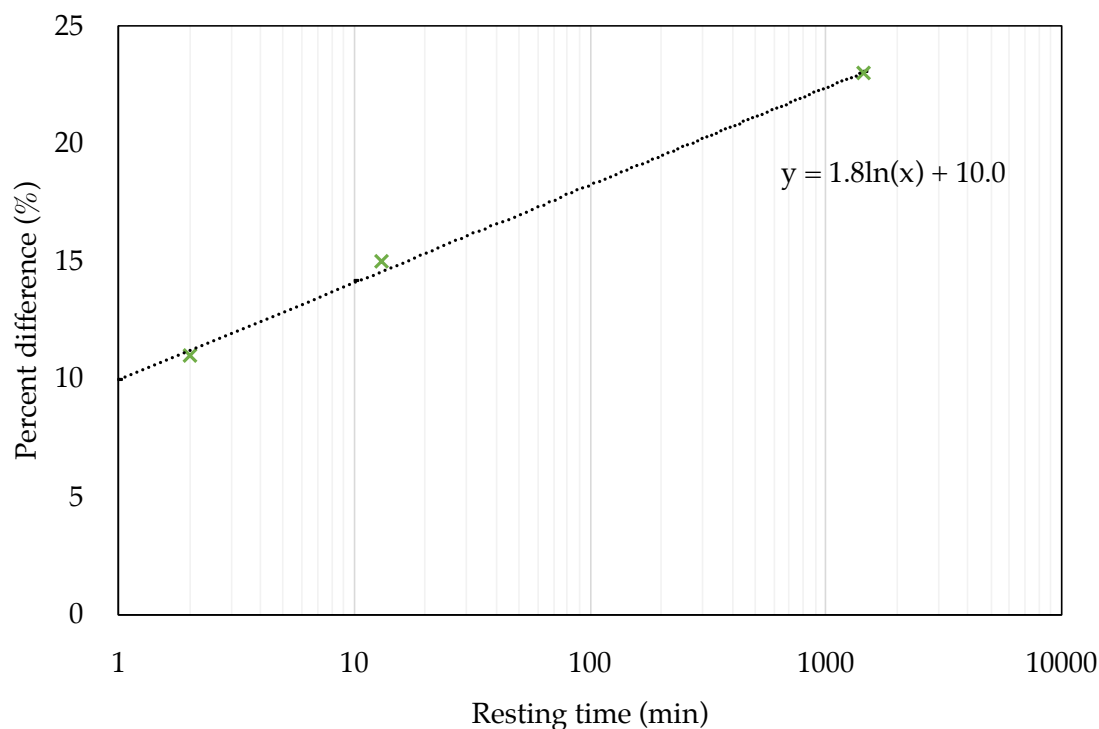
Figure 5.11: Flexural strength loss due to layered manufacturing given as the ratio of the difference in flexural strength normal and parallel (to interface) to the flexural strength in the normal direction, as a function of time gaps (or time intervals). Samples were tested at age of 28 day. Data from [43].

Another interesting finding is the effect of a cold joint on the resistance of concrete or mortar to chloride penetration. As it can be clearly seen from Figures 5.5 and 5.6, sample A60 was the one with the worst performance in terms of chloride and moisture ingress. This shows that the time interval between layers is finite and needs to be controlled as was discussed in [42]. Likewise, it can be seen in Figure 5.10, where the 24 hour time interval leads to almost 100% difference in the penetrations depths. It also confirms that the large time interval between layers could be detrimental for a concrete object or structure in terms of its durability. This is important, not only for chloride ingress, but also for other

substances that can damage the concrete or reinforcement, such as sulfates and CO_2.

Furthermore, since the possible formation of cold joints in 3D printed structures creates an imminent threat on the structure's durability, it is even more important to have access to a method that offers a spatial distribution of the aggressive agent, chlorides for example. For one thing, if the samples in Figure 5.5 were being analyzed for chloride content at a certain depth, the results with the conventional methods would certainly be misrepresentative. Like it can be seen in Figure 5.5, the penetration depth at the cold joint is much larger than in the rest of the sample. Henceforth, conventional methods used in practice to characterize chloride profiles do not work in this case. An average value over cross-sections is extremely misleading for the case of cold joints in 3D printed concrete.

It has been shown that chloride induced pitting corrosion in reinforced concrete has a stochastic nature, and that already in regular concrete it poses a misleading notion in terms of the critical chloride content at the concrete-steel interface for corrosion initiation [7,31,116]. Angst et al [31] stated that local chloride concentration as well as interfacial or defects on the surface of the reinforcement, all exhibit spatial variability, and that depassivation of the reinforcement only occurs by coincidence of the latter with a sufficiently high local chloride concentration. On top of this, as was stated in Chapter 2, section 2.3, the front of the chloride ingress in a concrete sample is not uniform, even if the parameters of exposure are controlled in a laboratory [7]. With all this being true for regular mold-cast concrete, the need for a spatial resolution of chloride ingress is only heightened in the case of 3D printed concrete. Without chloride mapping in 3D

printed structures, one would all too often conclude that chloride concentrations are not critical, while the contrary may be true.

Finally, we also note that all samples examined in this chapter had a 7 day wet curing after production. This represents a quite advantageous situation with respect to what can be expected for structure produced by 3D extrusion printing that for the most part are directly exposed to drying. Thus the fact that these samples evidence the issue of cold joints implies that this issue is probably even greater for normal extrusion printing that would not benefit from a 7 day wet curing.

5.5. Conclusions and Outlook

Although there is great potential for 3D printing of concrete to provide significant contributions to the construction industry, there are still many challenges that need to be addressed. As it was reported in other studies [43,105,111,115], and supported by the work done for this chapter, an important challenge is the bond quality of the interfaces between layers of a printed concrete or mortar, as it can have a direct impact on the strength. It is important to understand it, not only to improve mechanical properties of the printed objects, but ultimately for durability issues as well.

Overall, it was confirmed that the curing conditions play a very important role in the quality of the interfacial bond between layers, especially in terms of moisture and chloride ingress into the material. The role of the time interval between layers is slightly less straightforward. Although it is evident that a 24 hours delay time is not at all ideal, the difference between 2 and 13 minutes for

the studied mix is not so obvious. Sanjayan et al [115] indicated a dependence on surface moisture on the previously extruded layer, and on the material's plastic viscosity, respectively. Clearly, more detailed analyses are needed to clarify this phenomenon.

On the whole, the presence of cold joints proved to be a potentially detrimental aspect for a 3D printed concrete or mortar object in terms of its durability. Whether it is chloride induced corrosion (in case there is steel reinforcement present) or other substance attack (e.g. sulfate attack), a cold joint, similar to a crack, has little to no resistance to moisture penetration compared to the bulk. Micro XRF has recently been used to characterize chloride profiles in cracked concrete [117]. Furthermore, using conventional methods to characterize the chloride profile over a cross section in such conditions, for example, is extremely misleading and so a method that offers a spatial resolution, such as ours, is highly needed.

Implications for extrusion-based 3D printing of concrete is that the issue of cold joints should be handled with care. Their formation and consequence depend on many factors and can change substantially when a process is scaled up and the contour length increases substantially. Variations of drying conditions during production will increase the variability of the interface quality. Results presented in this chapter concern samples that had 7 days of wet curing, which most probably attenuates the extent of cold joint formation with respect to what could be expected in production. Finally, the question of the structure orientation with respect to chloride ingress will also play and important role, as well of course as the exposure conditions.

Chapter 6 - Global Conclusions and Outlook

Section 6.1 of this chapter is in part based on a paper published in the Microchemical Journal:

"Standard and sample preparation for the micro XRF quantification of chlorides in hardened cement pastes"

By Paula Bran-Anleu, Francesco Caruso, Timothy Wangler, Ekaterina Pomjakushina, Robert J. Flatt [1]

6.1. Main Outcomes

The main outcome of this thesis has been to develop and establish a methodology to reliably map and quantify chlorides in hardened cement paste using micro XRF. This involved setting up an effective protocol to prepare standards and defining their effective use to set up a calibration model. Additionally, the developed method performs well on hardened cement pastes with cements of different compositions as well as for different water to cement ratios. In the latter case, although the method is also functional, this study shows however that more

attention needs to be paid with respect to paste homogeneity in relatively high w/c ratios.

In particular, the micro XRF method for the quantitative analysis of chloride in hardened cement paste has been validated with respect to a widely accepted standard procedure (conventional XRF). Moreover, our approach offers two main advantages over other methods. The first is that it gives access to mapping over large surfaces, and the second is that it does not require samples to be excessively destroyed in the process.

While there exist other measurement methods for chlorides, most of these are destructive, time consuming, and/or do not offer any information on the spatial variability of chloride in concrete (or cement paste) [7–9,25]. In the case of EDS mapping in an Electron-Microscope, the sample preparation is more tedious and the range over which the mapping can be conducted is much more limited. With respect to the conventional XRF method, it should be underlined that measurements by micro XRF can be performed at ambient air conditions on freshly split surfaces, which is very practical. Additionally, if combined with the proper technique to quantify free chlorides, micro XRF can deliver important information about the inhomogeneities in chloride ingress, which we believe to be important for developing more reliable service life predictions of existing infrastructures.

Another main advantage of our method is that it can provide data both on the microscopic and macroscopic level, granting high spatial resolution. In the present work, only cement paste was used for the development of the method and, as expected, no spatial variability was seen. However, the end goal of developing this method is to extend it to concrete samples, where it has been

shown that, although exposure may be homogenous, the chloride front may not be (macroscopically) homogeneous whatsoever [7]. At the scale of concrete cover, this can play a major influence on corrosion initiation, so that the spatial resolution offered by micro XRF presents unique additional advantages.

Our initial intent of applying micro XRF was to gain more knowledge on chloride transport in cement pastes, both by diffusion and capillarity. However, as explained in Chapter 4, results fell short of our initial objectives. In particular the use of ions selective electrodes (ISEs) did not turn out to provide adequate results. In particular in capillary rise, the streaming potential turned out to produce major artifacts, while in the diffusion experiments the replenishing of the storage solution also perturbed the measurements.

Nevertheless, the related experiments led to a series of useful observations and conclusions. The most notable of these was that in the samples with W/C of 0.60 the microstructure was non-homogenous on the top and bottom of the samples, probably due to segregation. Specifically, the samples contained some very porous, horizontal bands that may represent collapse events of the flocculated microstructure between casting and final setting. Importantly, these bands enabled a much faster chloride ingress that would not have been detected if it were not for the micro XRF chemical imaging. This result can have major implications for the durability of cementitious systems, particularly pastes and grouts.

Regarding the capillary rise experiments, there were two significant conclusions. Firstly and as mentioned above, the streaming potentials completely compromised the results. Because of the nature of ionic solution flows in a porous material with charged pore walls, the equilibrium state between the electrolytic

solution and the electrical double layer is displaced. This can seriously perturb the potentials measured by the ISEs and thus compromises their reliability in capillary rise experiments for cementitious materials. This should be considered if such electrodes are to be used in situations where data is needed at times when the level of water saturation in concrete is changing.

The other important outcome from our capillary rise experiments is an indication that Friedel's salt formation is not necessarily fast compared to capillary ingress. This result is important because many transport models implicitly assume a very fast formation rate of Friedel's salt [102].

Lastly, we applied the mapping capacity of micro XRF to examine a very topical subject in concrete research. This relates to the durability of 3D printed concrete and in particular the question of whether the bond quality of the interfaces between layers can be problematic. While some studies have reported preliminary measurements on strength, the question of durability has not yet been dealt with systematically. In this context, micro XRF chemical imaging is particularly well suited. Specifically, our results prove that the presence of cold joints is a potentially detrimental aspect for a 3D printed cementitious system in terms of its durability. Actually, a cold joint has little to no resistance to moisture penetration compared to the bulk. Therefore, the issue of cold joints should be treated with caution. Their formation and consequence depend on many different factors that can substantially change when a process is scaled up.

6.2. Outlook

One of the main outcomes of this thesis is the development of an effective protocol to create standards for chloride quantification in hardened cement

pastes [1]. Appendix B, very briefly describes the different trials of creating standards that ultimately lead to the protocol presented in Chapter 1.

The high sensitivity of our method would allow for a more comprehensive study on the fundamentals of chloride transport in concrete, chloride binding in concrete, critical chloride content for pitting corrosion initiation, and the formation kinetics of Friedel's salt.

As it has been emphasized several times in this thesis, the characterization of chloride transport in cementitious materials is not trivial. In the last few decades, extensive research has been conducted with the intention to better understand the behavior of chlorides in concrete. More recently, the power of micro XRF has been implemented in hopes of obtaining more information regarding this topic [1,8,118]. Certainly, Khanzadeh et al [8] have reached very significant results, where they have successfully quantified chlorides in concrete using an extensive image processing of micro XRF data. However, their method is limited to quantifying and measuring chloride profiles and penetrations depths, where the quantifications are determined in regions rather than points in the chemical map. This ultimately leads back to having to draw upon the same over simplified mathematical models for determining the "apparent" diffusion coefficients of chlorides in concrete. This issue is specifically what we intended to address with the development of a more robust quantification technique. As can be found in Appendix A, the original plan was to use micro XRF to locally quantify transport coefficients of chlorides in concrete and their variation in the cover. Though this proved to be extremely challenging, the resulting method, if extended to concrete or stone samples, can ultimately promote further research concerning the behavior of chlorides therein.

The potential of the method is not limited to the study of transport coefficients. As it was found in Chapter 4, the rate of formation of Friedel's salt is slower than the capillary rise. This result could have major implications, and further investigations are needed. Unquestionably, in order to achieve this the micro XRF quantification method has to be coupled with another method to measure and quantify the free chloride in the system. As was described in Chapter 4, a valid and convenient technique to measure and quantify free chlorides in concrete is the use of ion selective electrodes (ISEs). However, close attention needs to be paid to the reliability of the potentials being measured.

As it is widely known, chloride binding reduces the free chloride concentration in the pore solution, and therefore the available chlorides that are mobile. Yet, as it was suggested by [119], chloride binding can also maintain higher concentration gradients in the exposed surface zone for longer periods of time. This effect increases the average velocity and quantity of chloride ions entering the concrete through diffusion. In other words, more chloride binding could be expected to cause a higher surface chloride content and a lower penetration depth. Also, a reduction in aggregate content in the surface zone due to packing constraints increases the cement paste content in said zone, which in turn increases the chloride content. This effect could in fact be as fast as the capillary rise process. Although more research is needed to confirm this phenomenon, it certainly underscores that designing perfect experiments to feed transport model remains a challenging task.

Importantly, since chloride binding, together with chloride transport ultimately affect the corrosion initiation, research concerning this issue can definitely benefit from the spatial quantification of chlorides. In a review [4], it was concluded that

given that there are many different procedures to evaluate a critical chloride content, it is very difficult to compare the results to select a reliable range of chloride threshold values. Moreover, one of the most important factors affecting said threshold is the interface between the reinforcing steel and the concrete matrix [4,119,120]. In this regard, the quantitative mapping of chlorides by micro XRF could potentially have significant contributions.

In reality, reinforced concrete structures are exposed to different environments where there may exist water/vapor pressure gradients. Still, many existing models [102,121] that consider migration and diffusion of chlorides are based on stationary liquid systems and/or steady state mechanisms [2,122]. Other transport processes that can occur are, for example, hydraulic flow, capillary suction in unsaturated pore systems, convection, and/or moisture flow and evaporation [2]. In a report written for the Danish Road Directorate by Nilsson et al [123], it was stated that because it is difficult or even impossible to quantify the effects of the combination of processes on the chloride transport in concrete, a better understanding and substantial data is needed before this quantification can be achievable. The mapping of chlorides by micro XRF, if further developed for the use with mortars and concretes, and with more carefully designed experiments, could open a door into that direction, in that it offers a unique insight into the inhomogeneous distribution of chlorides throughout concrete microstructure, something that has been defined as a very important but largely overlooked reality [7]. We strongly believe that it is in such directions that micro XRF can make its most important contributions to research and transport modelling.

Lastly, there is a modern growing concern regarding durability in the new and upcoming popular technology of digitally fabricated concrete. As was demonstrated in Chapter 5, the presence of cold joints could be detrimental for 3D printed concrete or mortar objects. Using conventional methods to characterize the chloride profile over a cross section, for example, is extremely misleading and so a method that offers a spatial resolution, such as ours, is highly needed to further study the implications of cold joints on durability issues surrounding 3D printed concrete. Our results suggest that chloride mapping offers a higher resolution to transport in cold joints that neutron imaging. Factors affecting cold joint formation are numerous and studying them systematically will imply having to measure numerous samples. Therefore, the great ease of use of micro XRF, represents a great advantage that researchers in the field should take advantage of if they want to address the legitimate concerns about the durability of concrete printed by 3D extrusion.

References

[1] P. Bran-Anleu, F. Caruso, T. Wangler, E. Pomjakushina, R.J. Flatt, Standard and sample preparation for the micro XRF quantification of chlorides in hardened cement pastes, Microchem. J. 141 (2018) 382–387. doi:10.1016/j.microc.2018.05.040.

[2] L. Tang, L.-O. Nilsson, P.A.M. Basheer, Resistance of Concrete to Chloride Ingress: Testing and modelling, CRC Press, 2011.

[3] U.M. Angst, R.D. Hooton, J. Marchand, C.L. Page, R.J. Flatt, B. Elsener, C. Gehlen, J. Gulikers, Present and future durability challenges for reinforced concrete structures, Mater. Corros. 63 (2012) 1047–1051. doi:10.1002/maco.201206898.

[4] U. Angst, B. Elsener, C.K. Larsen, Ø. Vennesland, Critical chloride content in reinforced concrete — A review, Cem. Concr. Res. 39 (2009) 1122–1138. doi:10.1016/j.cemconres.2009.08.006.

[5] Angst, U. M., Elsener, B., Chloride threshold values for corrosion in concrete - a myth?, in: Grantham, Michael (Ed.), Concr. Solut., CRC Press, 2016: p. 391.

[6] F.P. Glasser, J. Marchand, E. Samson, Durability of concrete — Degradation phenomena involving detrimental chemical reactions, Cem. Concr. Res. 38 (2008) 226–246. doi:10.1016/j.cemconres.2007.09.015.

[7] U.M. Angst, R. Polder, Spatial variability of chloride in concrete within homogeneously exposed areas, Cem. Concr. Res. 56 (2014) 40–51. doi:10.1016/j.cemconres.2013.10.010.

[8] M. Khanzadeh Moradllo, B. Sudbrink, Q. Hu, M. Aboustait, B. Tabb, M.T. Ley, J.M. Davis, Using micro X-ray fluorescence to image chloride profiles in concrete, Cem. Concr. Res. 92 (2017) 128–141. doi:10.1016/j.cemconres.2016.11.014.

[9] T. Yang, X. Yao, Z. Zhang, Quantification of chloride diffusion in fly ash–slag-based geopolymers by X-ray fluorescence (XRF), Constr. Build. Mater. 69 (2014) 109–115. doi:10.1016/j.conbuildmat.2014.07.031.

[10] E.P. Nielsen, M.R. Geiker, Chloride diffusion in partially saturated cementitious material, Cem. Concr. Res. 33 (2003) 133–138. doi:10.1016/S0008-8846(02)00939-0.

[11] E. Samson, J. Marchand, K.A. Snyder, Calculation of ionic diffusion coefficients on the basis of migration test results, Mater. Struct. 36 (2003) 156–165.

[12] A. Dehghan, K. Peterson, G. Riehm, L. Herzog Bromerchenkel, Application of X-ray microfluorescence for the determination of chloride diffusion coefficients in concrete chloride penetration experiments, Constr. Build. Mater. 148 (2017) 85–95. doi:10.1016/j.conbuildmat.2017.05.072.

[13] K.A. Snyder, D.P. Bentz, J.M. Davis, Using Viscosity Modifiers to Reduce Effective Diffusivity in Mortars, J. Mater. Civ. Eng. 24 (2012) 1017–1024. doi:10.1061/(ASCE)MT.1943-5533.0000524.

[14] G.K. Glass, B. Reddy, N.R. Buenfeld, The participation of bound chloride in passive film breakdown on steel in concrete, Corros. Sci. 42 (2000) 2013–2021. doi:10.1016/S0010-938X(00)00040-8.

[15] L. Tang, L.-O. Nilsson, A new approach to the determination of pore distribution by penetrating chlorides into concrete, Cem. Concr. Res. 25 (1995) 695–701. doi:10.1016/0008-8846(95)00058-K.

[16] J. Tritthart, Chloride binding in cement I. Investigations to determine the composition of porewater in hardened cement, Cem. Concr. Res. 19 (1989) 586–594. doi:10.1016/0008-8846(89)90010-0.

[17] J. Tritthart, Chloride binding in cement II. The influence of the hydroxide concentration in the pore solution of hardened cement paste on chloride binding, Cem. Concr. Res. 19 (1989) 683–691. doi:10.1016/0008-8846(89)90039-2.

[18] C. Arya, N.R. Buenfeld, J.B. Newman, Factors influencing chloride-binding in concrete, Cem. Concr. Res. 20 (1990) 291–300. doi:10.1016/0008-8846(90)90083-A.

[19] C. Andrade, Calculation of chloride diffusion coefficients in concrete from ionic migration measurements, Cem. Concr. Res. 23 (1993) 724–742. doi:10.1016/0008-8846(93)90023-3.

[20] P.F. McGrath, R.D. Hooton, Re-evaluation of the AASHTO T259 90-day salt ponding test, Cem. Concr. Res. 29 (1999) 1239–1248. doi:10.1016/S0008-8846(99)00058-7.

[21]   K.D. Stanish, R.D. Hooton, M.D.A. Thomas, Testing the chloride penetration resistance of concrete: a literature review, FHWA Contract DTFH61. (1997) 19–22.

[22]   ASTM C1202 - 17a - Standard Test Method for Electrical Indication of Concrete's Ability to Resist Chloride Ion Penetration, n.d.

[23]   M.-H. Zhang, O.E. Gjorv, Permeability of High-Strength Lightweight Concrete, Mater. J. 88 (1991) 463–469. doi:10.14359/2108.

[24]   Geiker, M., Thaulow, N., Anderson, J., Assessment of rapid chloride permeability test of concrete with and without mineral admixtures., in: Brighton, UK, 1990.

[25]   Schweizerischer Ingenieur- und Architekten-Verein, Swiss Society of Engineers and Architects, SIA 262.496, Products and systems for the protection and repair of concrete structures - test methods - determination of chloride content in hardened concrete, SIA, Zürich, 2008.

[26]   T. Luping, L.-O. Nilsson, Rapid Determination of the Chloride Diffusivity in Concrete by Applying an Electric Field, Mater. J. 89 (1993) 49–53. doi:10.14359/1244.

[27]   J. Marchand, E. Samson, Predicting the service-life of concrete structures – Limitations of simplified models, Cem. Concr. Compos. 31 (2009) 515–521. doi:10.1016/j.cemconcomp.2009.01.007.

[28]   A. Delagrave, J.P. Bigas, J.P. Ollivier, J. Marchand, M. Pigeon, Influence of the interfacial zone on the chloride diffusivity of mortars, Adv. Cem. Based Mater. 5 (1997) 86–92. doi:10.1016/S1065-7355(96)00008-9.

[29]   P. Goltermann, Variation of chloride profiles in homogeneous areas, Mater. Struct. 37 (n.d.) 608–614. doi:10.1007/BF02483290.

[30]   H. Yu, W.H. Hartt, Effects of Reinforcement and Coarse Aggregates on Chloride Ingress into Concrete and Time-to-Corrosion: Part 1—Spatial Chloride Distribution and Implications, Corrosion. 63 (2007) 843–849. doi:10.5006/1.3278434.

[31]   U.M. Angst, B. Elsener, C.K. Larsen, Ø. Vennesland, Chloride induced reinforcement corrosion: Electrochemical monitoring of initiation stage and chloride threshold values, Corros. Sci. 53 (2011) 1451–1464. doi:10.1016/j.corsci.2011.01.025.

[32]   K.D. Stanish, R.D. Hooton, M.D.A. Thomas, Testing the Chloride Penetration Resistance of Concrete: A Literature Review, (n.d.) 34.

[33]   ASTM C 1152/C 1152M – 97 Standard Test Method for Acid-Soluble Chloride in Mortar and Concrete, n.d.

[34]   Revision of NT BUILD 208 Concrete Hardened: Chloride Content, 1996.

[35]   ASTM C114 - Standard Test Methods for Chemical Analysis of Hydraulic Cement, n.d.

[36]   R.K. Dhir, M.R. Jones, H.E.H. Ahmed, Determination of total and soluble chlorides in concrete, Cem. Concr. Res. 20 (1990) 579–590. doi:10.1016/0008-8846(90)90100-C.

[37]   E. Proverbio, F. Carassiti, Evaluation of chloride content in concrete by X-ray fluorescence, Cem. Concr. Res. 27 (1997) 1213–1223. doi:10.1016/S0008-8846(97)00108-7.

[38]   ISO 29581-2, Cement Test Methods. Part 2: Chemical analysis by X-ray Fluorescence, na, 2002.

[39]   U. Angst, Ø. Vennesland, R. Myrdal, Diffusion potentials as source of error in electrochemical measurements in concrete, Mater. Struct. 42 (2009) 365–375. doi:10.1617/s11527-008-9387-5.

[40]   U. Angst, B. Elsener, C.K. Larsen, Ø. Vennesland, Potentiometric determination of the chloride ion activity in cement based materials, J. Appl. Electrochem. 40 (2010) 561–573. doi:10.1007/s10800-009-0029-6.

[41]   Y.S. Femenias, U. Angst, F. Caruso, B. Elsener, Ag/AgCl ion-selective electrodes in neutral and alkaline environments containing interfering ions, Mater. Struct. 49 (2016) 2637–2651. doi:10.1617/s11527-015-0673-8.

[42]   T. Wangler, E. Lloret, L. Reiter, N. Hack, F. Gramazio, M. Kohler, M. Bernhard, B. Dillenburger, J. Buchli, N. Roussel, R. Flatt, Digital Concrete: Opportunities and Challenges, RILEM Tech. Lett. 1 (2016) 67–75. doi:10.21809/rilemtechlett.2016.16.

[43]   V.N. Nerella, S. Hempel, V. Mechtcherine, MICRO- AND MACROSCOPIC INVESTIGATIONS ON THE INTERFACE BETWEEN LAYERS OF 3D-PRINTED CEMENTITIOUS ELEMENTS, (2017) 11.

[44]   N. Roussel, F. Cussigh, Distinct-layer casting of SCC: The mechanical consequences of thixotropy, Cem. Concr. Res. 38 (2008) 624–632. doi:10.1016/j.cemconres.2007.09.023.

[45]   H. Friedman, L.S. Birks, A Geiger Counter Spectrometer for X-Ray Fluorescence Analysis, Rev. Sci. Instrum. 19 (1948) 323–330. doi:10.1063/1.1741258.

[46]   T. Arai, Introduction, in: D.B. Beckhoff, D. habil B. Kanngießer, P.D.N. Langhoff, D. sc nat R. Wedell, D. sc nat H. Wolff (Eds.), Handb. Pract. X-Ray Fluoresc. Anal., Springer Berlin Heidelberg, 2006: pp. 1–31. doi:10.1007/978-3-540-36722-2_1.

[47]   R. Jenkins, X-ray fluorescence spectrometry, 2nd ed, Wiley, New York, 1999.

[48]   M. Haschke, Laboratory Micro-X-Ray Fluorescence Spectroscopy, Springer International Publishing, Cham, 2014. doi:10.1007/978-3-319-04864-2.

[49]   J.N. Miller, J.C. Miller, Statistics and chemometrics for analytical chemistry, 6. ed, Prentice Hall, Harlow, 2010.

[50]   M. Mantler, J. Willis, G. Lachance, B.A.R. Vrebos, K.-E. Mauser, N. Kawahara, R.M. Rousseau, P.N. Brouwer, Quantitative Analysis, in: D.B. Beckhoff, D. habil B. Kanngießer, P.D.N. Langhoff, D. sc nat R. Wedell, D. sc nat H. Wolff (Eds.), Handb. Pract. X-Ray Fluoresc. Anal., Springer Berlin Heidelberg, 2006: pp. 309–410. doi:10.1007/978-3-540-36722-2_5.

[51]   M. Schmeling, R. Van Grieken, Sample Preparation for X-ray Fluorescence, in: Handb. X-Ray Spectrom. Second Ed., CRC Press, 2001. doi:10.1201/9780203908709.ch14.

[52]   R. Rousseau, How to Apply the Fundamental Parameters Method to the Quantitative X-ray Fluorescence Analysis of Geological Materials, J. Geosci. Geomat. J. Geosci. Geomat. 1 (2013) 1–7. doi:10.12691/jgg-1-1-1.

[53]   R.M. Rousseau, Fundamental algorithm between concentration and intensity in XRF analysis 1—theory, X-Ray Spectrom. 13 (1984) 115–120. doi:10.1002/xrs.1300130306.

[54]   J. Injuk, R.V. Grieken, A. Blank, L. Eksperiandova, V. Buhrke, Specimen Preparation, in: D.B. Beckhoff, D. habil B. Kanngießer, P.D.N. Langhoff, D. sc nat R. Wedell, D. sc nat H. Wolff (Eds.), Handb. Pract. X-Ray Fluoresc. Anal., Springer Berlin Heidelberg, 2006: pp. 411–432. doi:10.1007/978-3-540-36722-2_6.

[55]   A. Erko, V. Arkadiev, A. Bjeoumikhov, A. Antonov, D.B. Beckhoff, I. Grigorieva, D. habil B. Kanngießer, B. Vidal, X-Ray Optics, in: D.B. Beckhoff, D. habil B. Kanngießer, P.D.N. Langhoff, D. sc nat R. Wedell, D. sc nat H. Wolff (Eds.), Handb. Pract. X-Ray Fluoresc. Anal., Springer Berlin Heidelberg, 2006: pp. 85–198. doi:10.1007/978-3-540-36722-2_3.

[56]   F. Scholze, A. Longoni, C. Fiorini, L. Strüder, N. Meidinger, R. Hartmann, N. Kawahara, T. Shoji, X-Ray Detectors and XRF Detection Channels, in: D.B.

Beckhoff, D. habil B. Kanngießer, P.D.N. Langhoff, D. sc nat R. Wedell, D. sc nat H. Wolff (Eds.), Handb. Pract. X-Ray Fluoresc. Anal., Springer Berlin Heidelberg, 2006: pp. 199–308. doi:10.1007/978-3-540-36722-2_4.

[57]   V.E. Buhrke, R. Jenkins, D.K. Smith, (Deane Kingsley), practical guide for the preparation of specimens for x-ray fluorescence and x-ray diffraction analysis, Wiley-VCH, 1998. http://agris.fao.org/agris-search/search.do?recordID=US201300313908 (accessed April 27, 2018).

[58]   R. Tertian, F. Claisse, Principles of Quantitative X-Ray Fluorescence Analysis, Heyden and Son Ltd, 1982.

[59]   P. Ambrosi, D. sc nat R. Wedell, W. Malzer, Appendix, in: D.B. Beckhoff, D. habil B. Kanngießer, P.D.N. Langhoff, D. sc nat R. Wedell, D. sc nat H. Wolff (Eds.), Handb. Pract. X-Ray Fluoresc. Anal., Springer Berlin Heidelberg, 2006: pp. 835–848. doi:10.1007/978-3-540-36722-2_8.

[60]   J. SHERMAN, The theoretical derivationof fluorescent X-rayintensities frommixtures, (n.d.) 24.

[61]   J. Sherman, The Correlation Between Fluorescent X-ray Intensity and Chemical Composition, in: Symp. Fluoresc. X-Ray Spectrogr. Anal., ASTM International, 100 Barr Harbor Drive, PO Box C700, West Consho hocken, PA 19428-2959, 1954: pp. 27-27–7. doi:10.1520/STP44075S.

[62]   T. Shiraiwa, N. Fujino, Theoretical Calculation of Fluorescent X-Ray Intensities in Fluorescent X-Ray Spectrochemical Analysis., Jpn. J. Appl. Phys. 5 (1966) 886. doi:10.1143/JJAP.5.886.

[63]   D.K.G. De Boer, J.J.M. Borstrok, A.J.G. Leenaers, H.A. Van Sprang, P.N. Brouwer, How accurate is the fundamental parameter approach? XRF analysis of bulk and multilayer samples, X-Ray Spectrom. 22 (1993) 33–38. doi:10.1002/xrs.1300220109.

[64]   R.M. Rousseau, The Quest for a Fundamental Algorithm in X-Ray Fluorescence Analysis and Calibration, Open Spectrosc. J. 3 (2009) 31–42. doi:10.2174/1874383800903010031.

[65]   R.M. Rousseau, M. Bouchard, Fundamental algorithm between concentration and intensity in XRF analysis. 3—Experimental verification, X-Ray Spectrom. 15 (1986) 207–215. doi:10.1002/xrs.1300150311.

[66]   R. Van Grieken, A. Markowicz, Quantification in XRF Analysis of Intermediate-Thickness Samples, in: Handb. X-Ray Spectrom. Second Ed., CRC Press, 2001. doi:10.1201/9780203908709.ch6.

[67]   K. Janssens, A. Rindby, Microbeam XRF, in: Handb. X-Ray Spectrom. Second Ed., CRC Press, 2001. doi:10.1201/9780203908709.ch11.

[68]   V.N. Vapnik, Statistical learning theory, Wiley, 1998.

[69]   N. Cristianini, J. Shawe-Taylor, An Introduction to Support Vector Machines and Other Kernel-based Learning Methods, Cambridge University Press, 2000.

[70]   B.H. Boyle, Support Vector Machines: Data Analysis, Machine Learning, and Applications, Nova Science Publishers, Incorporated, 2011.

[71]   B. Schölkopf, A.J. Smola, Learning with Kernels: Support Vector Machines, Regularization, Optimization, and Beyond, MIT Press, 2002.

[72]   F. Chauchard, R. Cogdill, S. Roussel, J.M. Roger, V. Bellon-Maurel, Application of LS-SVM to non-linear phenomena in NIR spectroscopy: development of a robust and portable sensor for acidity prediction in grapes, Chemom. Intell. Lab. Syst. 71 (2004) 141–150. doi:10.1016/j.chemolab.2004.01.003.

[73]   H. Zhao, F. Magoulès, A review on the prediction of building energy consumption, Renew. Sustain. Energy Rev. 16 (2012) 3586–3592. doi:10.1016/j.rser.2012.02.049.

[74]   K. Danzer, Analytical chemistry: theoretical and metrological fundamentals, Springer, Berlin ; New York, 2007.

[75]   S. Mitra, Sample Preparation Techniques in Analytical Chemistry, John Wiley & Sons, 2004.

[76]   Daniel C. Harris, Quantitative chemical analysis, 8th ed.; internat. ed., Freeman, New York, 2010.

[77]   D. Harvey, Modern analytical chemistry, McGraw-Hill, Boston, 2000.

[78]   P.A. Pella, M. Lankosz, Highlights of x-ray spectrometry for microanalysis, X-Ray Spectrom. 26 (1997) 327–332. doi:10.1002/(SICI)1097-4539(199711/12)26:6<327::AID-XRS230>3.0.CO;2-5.

[79]   F. Caruso, S. Saverwyns, M. Bos, D.F. Chillura Martino, A.-E. Ceulemans, J. Valck, E. Caponetti, Micro-X-Ray Fluorescence and the Old Masters: Non-destructive in situ characterisation of the varnish of historical Low Countries stringed musical instruments, Appl. Phys. A. 107 (2012) 197–202. doi:10.1007/s00339-011-6729-x.

[80]   H.A.O. Wang, D. Grolimund, L.R. Van Loon, K.D. Barmettler, C.N. Borca, B. Aeschlimann, D. Günther, High Spatial Resolution Quantitative Imaging by Cross-calibration Using Laser Ablation Inductively Coupled Plasma Mass Spectrometry and Synchrotron Micro-X-ray Fluorescence Technique, Chim. Int. J. Chem. 66 (2012) 223–228. doi:10.2533/chimia.2012.223.

[81]   R. Flatt, N.A. Mohamed, F. Caruso, H. Derluyn, J. Desarnaud, B. Lubelli, R.M.E. Marzal, L. Pel, C. Rodriguez-Navarro, G.W. Scherer, N. Shahidzadeh, M. Steiger, Predicting salt damage in practice: A theoretical insight into laboratory tests., RILEM Tech. Lett. 2 (2017) 108–118. doi:10.21809/rilemtechlett.2017.41.

[82]   K.L. Scrivener, Options for the future of cement, (2014) 11.

[83]   A. Yahia, S. Mantellato, R.J. Flatt, 7 - Concrete rheology: A basis for understanding chemical admixtures, in: Sci. Technol. Concr. Admix., Woodhead Publishing, 2016: pp. 97–127. doi:10.1016/B978-0-08-100693-1.00007-2.

[84]   ISO 5725-1:1994, - Accuracy (trueness and precision) of measurement methods and results -- Part 1: General principles and definitions, ISO, 1994. http://www.iso.org/iso/home/store/catalogue_ics/catalogue_detail_ics.htm?csnumber=11833 (accessed January 30, 2018).

[85]   Bureau International des Poids et Mesures, JCGM 200:2012 - International vocabulary of metrology – Basic and general concepts and associated terms (VIM), 2012.

[86]   M. Nič, J. Jirát, B. Košata, A. Jenkins, A. McNaught, IUPAC Gold Book - precision, (2009). doi:10.1351/http://goldbook.iupac.org/P04799.html.

[87]   A. Karatzoglou, Institut fur Statistik Ludwig-Maximilians-Universitat Munchen, (n.d.) 210.

[88]   R Development Core Team, R: A language and environment for statistical computing. R Foundation for Statistical Computing, Vienna, Austria, 2008. http://www.R-project.org.

[89]   U. Angst, ø. Vennesland, Detecting critical chloride content in concrete using embedded ion selective electrodes - effect of liquid junction and membrane potentials, Mater. Corros. 60 (2009) 638–643. doi:10.1002/maco.200905280.

[90]   Segui Femenias, Y., Angst, U. M., Elsener, B., Durability monitoring of reinforced concrete, in: Zurich, Switzerland, 2017.

[91]   J. Koryta, Theory and applications of ion-selective electrodes part II, Anal. Chim. Acta. 91 (1977) 1–85. doi:10.1016/S0003-2670(01)95921-5.

[92]   A.J. Bard, L.R. Faulkner, Electrochemical methods: fundamentals and applications, 2nd ed, Wiley, New York, 2001.

[93]   G. de Vera, A. Hidalgo, M.A. Climent, C. Andrade, C. Alonso, Chloride-Ion Activities in Simplified Synthetic Concrete Pore Solutions: The Effect of

the Accompanying Ions, J. Am. Ceram. Soc. 83 (2000) 640–644. doi:10.1111/j.1151-2916.2000.tb01245.x.

[94]   A. Hidalgo, G. De Vera, M.A. Climent, C. Andrade, C. Alonso, Measurements of Chloride Activity Coefficients in Real Portland Cement Paste Pore Solutions, J. Am. Ceram. Soc. 84 (2001) 3008–3012. doi:10.1111/j.1151-2916.2001.tb01128.x.

[95]   S. Jones, N. Martys, Y. Lu, D. Bentz, Simulation studies of methods to delay corrosion and increase service life for cracked concrete exposed to chlorides, Cem. Concr. Compos. 58 (2015) 59–69. doi:10.1016/j.cemconcomp.2014.12.014.

[96]   S. Jacobsen, J. Marchand, L. Boisvert, Effect of cracking and healing on chloride transport in OPC concrete, Cem. Concr. Res. 26 (1996) 869–881. doi:10.1016/0008-8846(96)00072-5.

[97]   T. Lorentz, C. French, Corrosion of reinforcing steel in concrete: effects of materials, mix composition, and cracking, ACI Mater. J. 92 (1995) 181–190.

[98]   Y. Schiegg, M. Büchler, M. Brem, Potential mapping technique for the detection of corrosion in reinforced concrete structures: Investigation of parameters influencing the measurement and determination of the reliability of the method, Mater. Corros. 60 (2009) 79–86. doi:10.1002/maco.200805042.

[99]   U. Angst, B. Elsener, R. Myrdal, Ø. Vennesland, Diffusion potentials in porous mortar in a moisture state below saturation, Electrochimica Acta. 55 (2010) 8545–8555. doi:10.1016/j.electacta.2010.07.085.

[100]   N. Massoussi, E. Keita, N. Roussel, The heterogeneous nature of bleeding in cement pastes, Cem. Concr. Res. 95 (2017) 108–116. doi:10.1016/j.cemconres.2017.02.012.

[101]   R. Myrdal, POTENTIAL GRADIENTS IN CONCRETE CAUSED BY CHARGE SEPARATIONS IN A COMPLEX ELECTROLYTE, (n.d.) 18.

[102]   Q. Yuan, C. Shi, G. De Schutter, K. Audenaert, D. Deng, Chloride binding of cement-based materials subjected to external chloride environment – A review, Constr. Build. Mater. 23 (2009) 1–13. doi:10.1016/j.conbuildmat.2008.02.004.

[103]   The third industrial revolution - Manufacturing, (n.d.). https://www.economist.com/leaders/2012/04/21/the-third-industrial-revolution (accessed July 17, 2018).

[104]   X. Wang, M. Jiang, Z. Zhou, J. Gou, D. Hui, 3D printing of polymer matrix composites: A review and prospective, Compos. Part B Eng. 110 (2017) 442–458. doi:10.1016/j.compositesb.2016.11.034.

[105] T.T. Le, S.A. Austin, S. Lim, R.A. Buswell, R. Law, A.G.F. Gibb, T. Thorpe, Hardened properties of high-performance printing concrete, Cem. Concr. Res. 42 (2012) 558–566. doi:10.1016/j.cemconres.2011.12.003.

[106] D. Marchon, S. Kawashima, H. Bessaies-Bey, S. Mantellato, S. Ng, Hydration and rheology control of concrete for digital fabrication: Potential admixtures and cement chemistry, Cem. Concr. Res. (n.d.). doi:10.1016/j.cemconres.2018.05.014.

[107] L. Reiter, T. Wangler, N. Roussel, R.J. Flatt, The role of early age structural build-up in digital fabrication with concrete, Cem. Concr. Res. (n.d.). doi:10.1016/j.cemconres.2018.05.011.

[108] R.A. Buswell, R.C. Soar, A.G.F. Gibb, A. Thorpe, Freeform Construction: Mega-scale Rapid Manufacturing for construction, Autom. Constr. 16 (2007) 224–231. doi:10.1016/j.autcon.2006.05.002.

[109] H.T. Cao, L. Bucea, A. Ray, S. Yozghatlian, The effect of cement composition and pH of environment on sulfate resistance of Portland cements and blended cements, Cem. Concr. Compos. 19 (1997) 161–171. doi:10.1016/S0958-9465(97)00011-5.

[110] DIN EN 12390-2 - Prufung von Festbeton - Teil 2: Herstellung und Lagerung von Probekorpern fur Festigkeitsprufungen, 2009.

[111] Schröfl, C., Nerella, V.N., Mechtcherine, V., Capillary water intake by 3D-printed concrete visualised and quantified by neutron radiography, in: Zurich, Switzerland, 2018.

[112] E. Lehmann, M. Raventos, R.P. Harti, P. Trtik, A. Kaestner, D. Mannes, C. Grünzweig, Methodical Progress in Neutron Imaging at PSI, Phys. Procedia. 88 (2017) 250–257. doi:10.1016/j.phpro.2017.06.035.

[113] NEUTRA: NEUtron Transmission RAdiography, Https://Www.Psi.Ch/Sinq/Neutra/Neutra. (n.d.). https://www.psi.ch/ (accessed July 17, 2018).

[114] C.A. Schneider, W.S. Rasband, K.W. Eliceiri, NIH Image to ImageJ: 25 years of image analysis, Nat. Methods. 9 (2012) 671–675.

[115] J.G. Sanjayan, B. Nematollahi, M. Xia, T. Marchment, Effect of surface moisture on inter-layer strength of 3D printed concrete, Constr. Build. Mater. 172 (2018) 468–475. doi:10.1016/j.conbuildmat.2018.03.232.

[116] C. Alonso, M. Castellote, C. Andrade, Chloride threshold dependence of pitting potential of reinforcements, Electrochimica Acta. 47 (2002) 3469–3481. doi:10.1016/S0013-4686(02)00283-9.

[117] T. Danner, K. De Weerdt, M.R. Geiker, μ-XRF – CHARACTERISATION OF CHLORIDE INGRESS AND SELF-HEALING IN CRACKED CONCRETE, Norsk Betongforening, 2017. https://brage.bibsys.no/xmlui/handle/11250/2475661 (accessed November 12, 2018).

[118] K. Peterson, G. Julio-Betancourt, L. Sutter, R.D. Hooton, D. Johnston, Observations of chloride ingress and calcium oxychloride formation in laboratory concrete and mortar at 5°C, Cem. Concr. Res. 45 (2013) 79–90. doi:10.1016/j.cemconres.2013.01.001.

[119] G.K. Glass, N.R. Buenfeld, The influence of chloride binding on the chloride induced corrosion risk in reinforced concrete, Corros. Sci. 42 (2000) 329–344. doi:10.1016/S0010-938X(99)00083-9.

[120] G.K. Glass, N.M. Hassanein, N.R. Buenfeld, Neural network modelling of chloride binding, Mag. Concr. Res. 49 (1997) 323–335. doi:10.1680/macr.1997.49.181.323.

[121] E. Samson, G. Lemaire, J. Marchand, J.J. Beaudoin, Modeling chemical activity effects in strong ionic solutions, Comput. Mater. Sci. 15 (1999) 285–294. doi:10.1016/S0927-0256(99)00017-8.

[122] D. Conciatori, H. Sadouki, E. Brühwiler, Capillary suction and diffusion model for chloride ingress into concrete, Cem. Concr. Res. 38 (2008) 1401–1408. doi:10.1016/j.cemconres.2008.06.006.

[123] L.-O. Nilsson, E. Poulsen, P. Sandberg, H. E. Sorensen, O. Klinghoffer, Chloride penetration into concrete: State of the Art, Transport processes, corrosion initiation, test methods and prediction models, Danish Road Directorate, 1996.

References

Appendix A – Original Plan

This appendix is in its majority, part of a grant proposal for the ETH Grant. The proposal was accepted in December of 2013. Grant number ETH-33 12-1.

A.1. Original objective

The proposed project specifically aims to develop a novel method to measure the transport coefficient of chlorides on existing reinforced concrete structures. This measurement method would operate at a micron to millimeter scale, and would be applied on concrete cores taken from real structures. This would provide the information needed to explain how the diffusion coefficient is affected by age, concrete's chloride binding capacity (both chemically and physically), among other factors. The method would not only be relatively fast, but also more representative of what really occurs in real structures to better understand the "natural" chloride transport in concrete. With the help of analytical chemistry techniques, we would obtain an average parameter with high spatial resolution of the chloride transport in a non-accelerated way. This new analytical procedure consists of quantitative high spatial resolution chemical imaging based on micro analytical techniques using micro- X-Ray Fluorescence. If successful, this novel

approach would be much faster than existing procedures and additionally provide spatial resolution of these transport coefficients. The objective, in other words, is to provide more reliable inputs for predictive models and to do so efficiently on a case-by-case basis.

A.2. State of the art for mathematical modeling of chloride transport in concrete

The subject of chloride transport in concrete is certainly broad and complex with controversial issues; however, there are a few generally accepted facts. One is that as concrete ages its transport coefficient evolves. This means that transport coefficients change as a function of time, as concrete continues to hydrate and the pore structure evolves. Second, carbonation that proceeds from the outside in can also modify transport coefficients. This implies that transport coefficients vary as a function of depth. Third, chlorides can be chemically bound to aluminate phases and physically adsorb on silicates. This implies that we are dealing with reactive transport in which the extent of reactivity is finite and is strongly dependent on the free chloride concentration in the pore solution (affects the physically bound chlorides) [9]. Presently, all these factors tend to be combined in empirical relations that have very little predictive power [1,3]. Although practical experience may suggest that one or another of these mechanisms may dominate, there is a clear lack of quantitative assessment that must be filled. For example, while carbonation may overall not be perceivable at substantial depths in concrete subject to chloride induced corrosion, it may significantly affect transport rates in the outermost part of the cover layer. It may also destabilize

Friedel's salt[4], thereby releasing chlorides into the pore solution that would otherwise be considered to be immobile.

A.3. Limitations of simplified models

Regardless of the important improvements in service-life models to predict the behavior of concrete structures exposed to chemically aggressive environments, engineers still rely on simplified approaches to do so [10]. The problem with these oversimplified models is the set of assumptions required to solve the diffusion equation for the complicated case of chloride transport in concrete. As was mentioned earlier, this phenomenon is complex; nonetheless, engineers and scientists adopted various simplifying assumptions making the solution unrealistic. One of the most commonly used models in practice today is the error function solution to Fick's Second Law of Diffusion (eq. (A.1))[10].

$$C_x = C_0 \left(\mathrm{erf} \left(\frac{x}{2\sqrt{D_{app}t}} \right) \right) \qquad \text{(A.1)}$$

where C_x is the chloride concentration at a depth x, C_0 is the concentration at the surface, t is time and D_{app} is the apparent diffusion coefficient. The validity of this solution is based on the assumptions discussed in the following paragraphs.

Collepardi et al. [12] was probably the first contribution on the quantification of the kinetics of chloride penetration into concrete using a mathematical equation.

---

[4] Friedel's salt: $Ca_4Al_2Cl_2(OH)_{12}.4H_2O$. It is one of the most important members of the AFm family (hydrate phase of cement). Chloride is an interlayer anion in the positively charged layers of calcium and aluminium that compose the mineral family (AFm). It results from the reaction that involves an AFm phase binding the chlorides in the pore solution [11].

One major assumption rapidly shown to be invalid was that the apparent diffusion coefficient, D_{app}, was a constant [10]. After this, numerous authors showed that the apparent diffusion coefficient depends on various parameters that were being neglected in the error function solution, especially in the case of material extracted from real reinforced concrete structures [12-14].

Firstly, equation (A.1) is valid only if the material is kept fully saturated and not subjected to any water movement. This is obviously not the case for real structures, since these are constantly subjected to wetting and drying cycles throughout their service life. The water loss at the surface contributes to a local reduction of the chloride concentration unlike what is predicted by Fick's Law during a drying cycle (Figure A.1). This complicates the determination of the chloride concentration at the surface C_0 that is required to solve equation (A.1). As can be seen in Figure A.1 the chlorides continue to penetrate but at a slower rate since the outside source is limited. This means that the boundary conditions and the modes of moisture transport fluctuate [10].
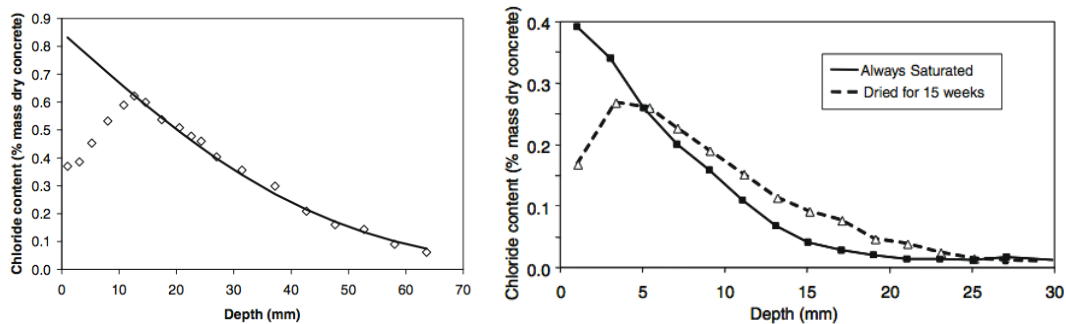

Figure A.1: [left] Typical chloride profile obtained from field samples (blank squares) and the chloride distribution curve predicted by Fick's diffusion model (solid line); [right] Impact of drying on (measured) chloride distribution within concrete [10].

Second, equation (A.1) is valid if the effect of the electrical coupling between the ions in the pore solution is neglected. This is clearly invalid since ions are charged species that do not move independently from one another. Electroneutrality has to be conserved in a system, and the ions in concrete's pore solution do not move at the same speed. Faster moving ions will create a local electric field and this will slow them down and accelerate the slower ions. This is called the diffusion potential [15], and it cannot be neglected [10].

Third, it was assumed that the influence of chemical activity gradients is minimal. In other words, the activity coefficients of the different species in the system are considered negligible. In reference [13] the authors noted that the diffusion coefficient in saturated pastes was strongly affected by the type of salt being used in the experiment. As can be seen in Figure A.2, there is a strong influence of the chemical environment on the penetration of the chloride ions in hydrated cement systems as was discussed in reference [13]. It can also be seen that the estimated apparent diffusion coefficient (obtained from fitting the chloride profiles to equation (A.1)) is not only affected by the type of salt being used, but also varies significantly with the chloride concentration of the test solution.
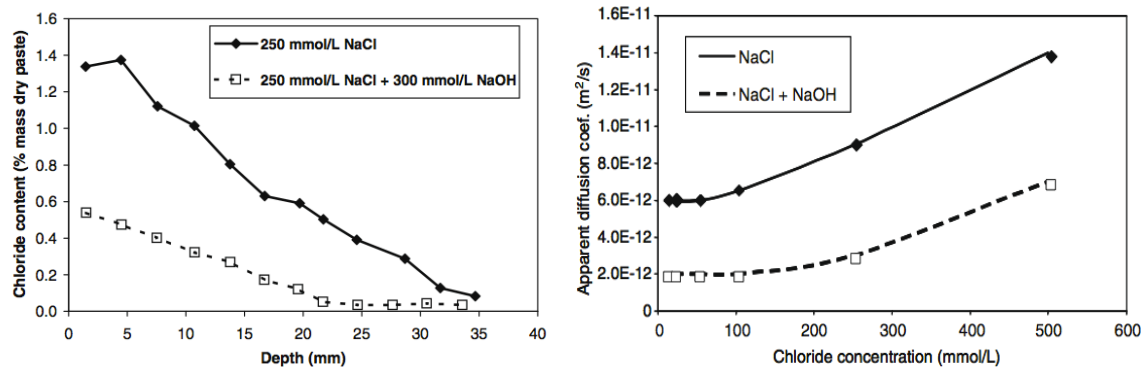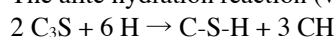
Figure A.2: [left] Chloride profiles for cement paste samples exposed to two different solutions; [right] Apparent diffusion coefficients evaluated from the chloride profiles of the same cement paste samples [10].

Finally, it was assumed that the amount of bound chlorides is a sole function of their concentration in the pore solution and that they are linearly correlated. However, chloride binding strongly depends on the hydration degree and the mineral admixtures of the concrete, and it is not simply a function of chloride in solution [9]. Luping and Nilsson [9] showed that the composition of the pore solution, especially the pH, significantly influences the binding of chlorides, and concrete's binding capacity strongly depends on the C-S-H (cement hydration product[5]) content. Additionally, it must be understood that C_x in equation (A.1) corresponds to the chloride content in the pore solution (free chlorides). Still, some papers were published where C_x was defined as the total concentration of chlorides (sum of free and bound chlorides) [16, 17], which completely violates the basic mass conservation equation at the derivation of equation (A.1).
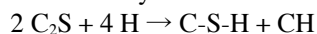
These fundamental limitations are further illustrated in Ref. [10] with an example of a twenty-year-old parking structure in Canada. Cores were extracted from the structure to measure the chloride profiles. Laboratory concrete cylinders were also prepared using known specifications of the parking structure concrete mix

---

[5] Cement Hydration. Cement reacts with water and the initially fluid paste transforms into a solid over time. The reaction of cement with water is a very complicated process, giving rise to several hydration products. Hydration of the calcium silicate phases leads to two products: calcium hydroxide (also known as portlandite, denoted as CH), and calcium silicate hydrate (denoted as C-S-H).
The alite hydration reaction (very simplified) is given below:
$2\ C_3S + 6\ H \rightarrow C\text{-}S\text{-}H + 3\ CH$
The belite hydration reaction (simplified) is given below:
$2\ C_2S + 4\ H \rightarrow C\text{-}S\text{-}H + CH$
Hydration of the aluminate phases in the presence of gypsum leads to two broad classes of products: AFt denotes a family of minerals referred to as aluminate ferrite tri-sulfate, and AFm denotes a family of minerals referred to as aluminate ferrite monosulfate. The most important AFt phase is ettringite. Its composition is: $3CaO.Al_2O_3.3CaSO_4.32H_2O$. [18]

design. These samples were cured at 100% RH for 3 years. Then samples were cut from one cylinder, and the cut surfaces were exposed to a NaCl solution for 90 days. Following this, chloride profiles were measured using a conventional and well-established method, and then the profiles were fitted to equation 1 to obtain C_0 and D_{app} (Figure A.4 left). These parameters were then used to simulate the profiles after 20 years. The chloride profiles done on the structure samples were also fitted to equation (A.1) to obtain C_0 and D_{app}.
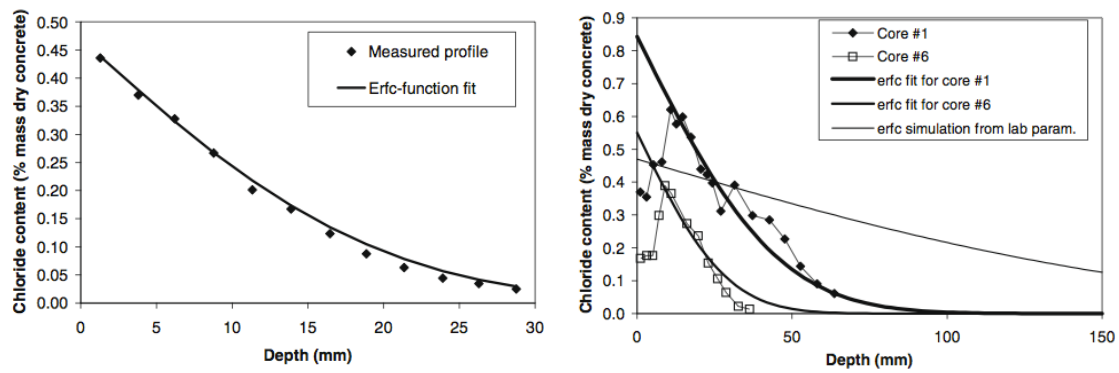
Figure A.3: [left] Measured chloride profile in laboratory concrete fitted with the erfc model; [right] Chloride profiles measured in cores from the parking structure compared to the estimations made on the basis of the simplified erfc model [10].

As shown in Figure A.4 on the right the profiles obtained using the parameters from the laboratory samples greatly overestimate the chloride ingress in the structure. The fitting procedure gave different values for D_{app} even though the results were obtained from similar materials (core from different parts of the structure and laboratory concrete). These results confirm that the use of apparent diffusion coefficient in a durability assessment cannot be considered safe, and that it is not possible to predict the long-term service life of a structure on the basis of laboratory experiments.

A.3.2. Free versus bound chlorides

Regarding binding capacity, there is plenty information available both from experiments and more recently from thermodynamic modeling. It is well known that cement has the ability to bind chlorides dividing their presence in concrete into free and bound chlorides (ions in the pore solution, and ions bound to hydration products in the form of Friedel's salt ($Ca_4Al_2Cl_2(OH)_{12}.4H_2O$) or sorbed to C-S-H) [9, 11, 19]. In other words, only free chlorides will be able to move, and concrete's chloride binding capacity may delay the penetration process to a certain extent.

A.3.2.1. Thermodynamic Modeling

As was mentioned before, many tests have been developed to characterize concrete's resistance to chloride ingress. These tests can be categorized into two categories: steady state and non-steady state tests. Under steady state conditions chloride binding has no influence on the results, whereas non-steady state transport can be affected by concrete's binding capacity. Accelerated testing methods to measure concrete's resistance to chloride ingress do not fully describe chloride transport considering concrete's complete binding capacity, because the strong current that is introduced in the system tends to reduce the amount of bound chlorides [20]. Therefore, different methods may lead to different results, and in the end they cannot be compared to each other.

Accordingly, an established thermodynamic modelling tool has been used at the Swiss Federal Laboratories for Material Testing and Research (EMPA) to study the chemical changes due to the ingress of chlorides into concrete. The influence

of permeability and chloride binding on concrete's resistance to chloride ingress was studied by combining experiments and thermodynamic modelling. The modelling tool that was used was the Gibbs Free Energy Minimization Program (GEMS) [21-23]. It was used to study the chemical changes linked to chloride penetration into concrete. GEMS is a geochemical modelling code which computes equilibrium phase assemblage and speciation in a complex chemical system from its total bulk elemental composition. It considers chemical interactions involving solids, solid solutions, and aqueous electrolytes concurrently.

Loser et al [24] used this modelling tool to calculate the changes in a concrete sample when NaCl is introduced. In the presence of high chloride concentrations (e.g. near the surface of the sample), ettringite and portlandite become unstable [24]. As a consequence, more Friedel's salt is formed. In the presence of NaCl leaching of portlandite, C-S-H, and Friedel's salt at the surface was observed. As it is well established, portlandite is much more soluble than C-S-H, and in contact with moisture it dissolves first giving Ca^+ and OH^- ions [25]. This effect is in turn slowed down by carbonation (carbonates), by the combination of the calcium ions (which diffuse outwards) and the carbonates (supplied by CO_2 from the atmosphere). Calcite ($CaCO_3$) is then precipitated on the surface creating a protective layer, which acts as a diffusion barrier [26, 27]. The thermodynamic model agrees with experimental observations where there is a decrease in chloride binding at high total chloride content, as well as a depletion of Friedel's salt and portlandite near the surface exposed to NaCl. Loser et al showed that for all their cases, chlorides are mainly in the pore solution [24]. Figure A.3 shows that conventional tests (e.g. accelerated tests) can exhibit consistent results. This

is somewhat surprising as the relative importance of chloride binding is a priori quite different in these tests.
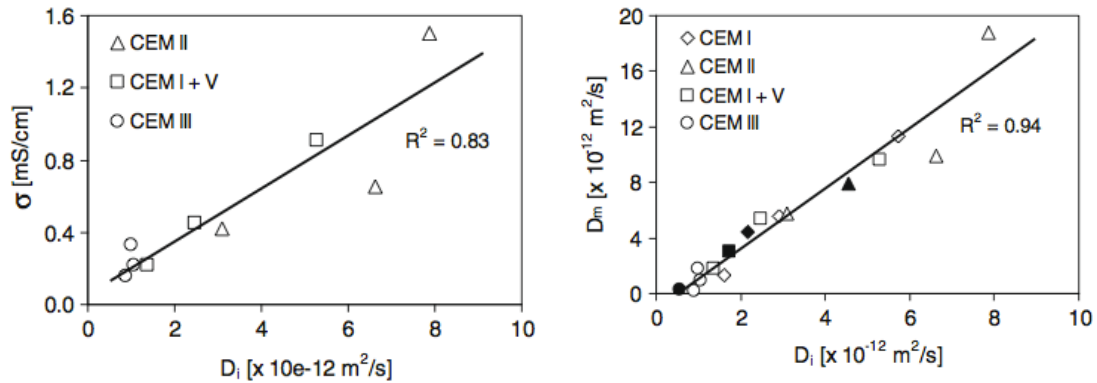

Figure A.4: [Left] Conductivity versus diffusion coefficient for the measured mixtures; [Right] Migration coefficient versus diffusion coefficient for all mixtures [24]

Both experiments and thermodynamic modelling show that chloride binding strongly depends on hydration degree and mineral admixtures, however as expected, concrete's resistance to chloride ingress is mainly due to its permeability. Yet, the methods the authors used to determine the diffusion coefficient are based on the testing procedures described previously. With the proposed method, a better estimate of the actual diffusion coefficient would be obtained. This would provide more realistic results, and fill in the gaps that are still lingering with a better understanding of the transport mechanisms of chlorides in concrete.

A.4. Experimental technique

An effective monitoring technique for the chloride concentration in concrete's pore solution is the use of Ion Selective Electrodes (ISEs) embedded in the material. Angst et al [28] discussed the applicability of Ag/AgCl ISEs as a non-

destructive chloride measurement technique in concrete. These ISEs are a solid-state membrane electrode that consists of a silver wire with a coating of silver chloride. Due to the low solubility of AgCl the sensor reacts to a chloride concentration and a potential difference, which follows Nernst Law, and it can be measured. Error sources such as interfering ions, activity versus concentration measurements, stability at high pH, and temperature changes were taken into account by the authors.

It was shown that these electrodes could be effectively used to measure the chloride ion activity in highly alkaline environments such as concrete. They pointed out that it is important to understand which potential is being measured, because diffusion potentials are a critical error source. It is also important to point out that this technique measures the activity of the free chlorides; still, in a nano-porous material such as cement paste, double layer effects, physical adsorption, and the chemical equilibrium between bound and free chlorides might affect the activity of dissolved chloride ions. This makes it unclear as to what chlorides the embedded ISEs respond to. These inaccuracy sources are being further researched in the Corrosion and Durability group of the Institute for Building Materials in an SNF funded project that aims to enhance this application. More insight on the different bonding status of chloride ions in cement-based materials were obtained by [29] in experiments with electrochemical chloride removal. It was clearly shown that all the free chloride ions were removed from the pore solution in few days. After two weeks the concentration of free chlorides increased (due to the dissolution of chemically bound chloride). Upon switching on the electric field a marked increase of the free chloride ions was detected, interpreted as desorption of physically bound chlorides. Thus the sensors react on free chloride ions only.

A.4.1. Analytical methodology for quantitative high spatial resolution chemical imaging based on micro-X-ray fluorescence

Many fundamental processes, such as chloride transport, are operational on the microscopic level, and to better understand these processes, we must gather knowledge on the corresponding microscopic scale. For this, a quantitative chemical imaging procedure using a micro-X-Ray fluorescence technique will be used. This methodology consists of an elemental analysis technique that allows for the investigation of very small sample areas. Micro X-ray Fluorescence uses direct X-ray excitation to induce characteristic X-ray fluorescence emission from the sample for elemental analysis, and uses X-ray optics to restrict the excitation beam size or focus the excitation beam to a small spot on the sample surface so that small features can be analyzed. This technique will allow us to improve our knowledge regarding reactive solute (chloride) transport mechanisms in heterogeneous media (concrete) [30].

The group in D-CHAB at ETH has employed this methodology to obtain high spatial resolution chemical images of Cesium (Cs) diffusion in Opalinus clay rock. A spatial resolution of approximately *3µm* was achieved using the synchroton radiation based micro-X-ray fluorescence. They were able to obtain quantitative information, which allows the identification of chemical processes, the specification of mass balances and the calculation of the corresponding reaction rates. This is an important outcome for the understanding of the basic reactive transport mechanisms that could lead to better and more reliable safety assessments or more efficient remediation strategies [31].

Bench top micro-XRF with high spatial resolution is now available. This is game-changing for chloride transport, as the number of cases that can be studied will increase. Thus if our method is successful, it can be expected that it would become a standard equipment for service companies involved in service-life predictions.

The National Institute of Standards and Technology (NIST) in The United States has used a similar method using a bench top μ-XRF. The method was performed on mortar samples previously exposed to potassium chloride solutions. It was shown that μ-XRF has the capability of tracking both species in the concrete, examining spatial distributions with 80 μm lateral resolution while visualizing distributions over centimeter distances [32]. A significant advantage of μ-XRF over other X-ray micro analytical techniques is its ability to produce elemental images from a heterogeneous surface at atmospheric pressure without the arduous surface requirements that other methods demand.

Researchers at NIST have also used μ-XRF to obtain detailed quantitative analysis of chloride ion profiles in mortars containing viscosity modifiers. The method allowed them to quantitatively estimate effective diffusivity by regression assuming ideal Fickian radial diffusion. Using this technique, they demonstrated that the use of viscosity modifiers could successfully reduce the effective diffusivity of chloride ions in mortar [33].

A.4.2. Strategy

The novelty of our approach to the old problem of chloride diffusion in concrete is to attempt to obtain spatially resolved information on the diffusion coefficients

inside the concrete cover. In particular, we wanted to obtain quantitative information on the dependence of these coefficients on local chloride concentration as well as phase assemblage (including the role of carbonation). Additionally, we anticipated doing this on samples taken from real structures.

The way in which we planned to do this includes the combination of micro-XRF, SEM-EDX, thermodynamic modeling, micro-chloride specific electrodes and a novel concept for the sample design. The later constituted the main originality of this project, the highest potential, but also the highest risk.

In short, the idea is represented in Figure A.5. There are various variants to it, but we use this specific one to illustrate the concept. A concrete core is cut into smaller pieces perpendicular to the longitudinal axis. One surface of these samples, normal to the surface of the structure from which they were taken is polished down to a close to mirror fineness in alcohol. After that, a hole is drilled into those samples (Figure A.5c). The idea is to fill this hole with a chloride containing solution and then follow the diffusion from above making use of the depth of penetration of micro-XRF.
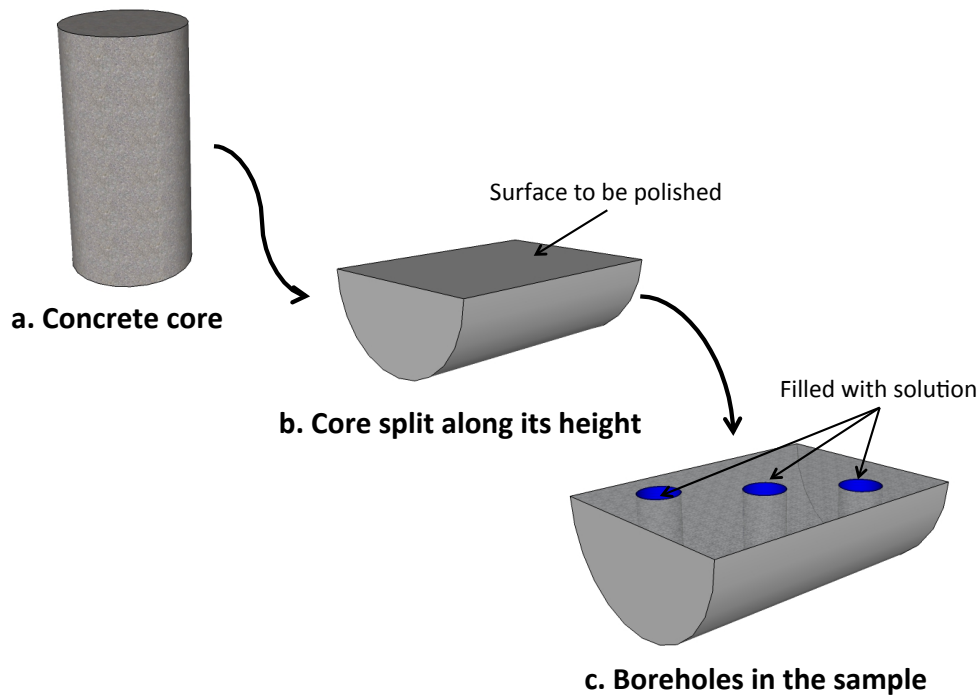
Figure A.5: Sketch of planned experiment

The great advantage is that the chloride determination would be nondestructive. For an inhomogeneous microstructure like concrete, this means that we can follow, in a given cross section how chlorides migrate, measuring at the exact same positions the evolution in their amount. This would provide a wealth of information for better representing diffusion in the composite material concrete. By drilling holes at different locations we would increase the amount of information and obtain the spatially resolved information on diffusion coefficients that we are targeting (see Figure A.6).

Presented like this, the experiment sounds almost trivial. There are however numerous hidden challenges that must be overcome. The first of these challenges consists in separating the amount of measured chlorides between bound and free chlorides. An important contribution in this step will come from the use of thermodynamic modeling (see state of the art section). For this, we will have to

rely on local chemical composition measurements of the cement paste. Indeed, with this in hand, it is possible to calculate the phase assemblage, including Fridel's salt (chloride containing AFm). This requires also local information on the amount of pore solution. These are delicate steps that have been dealt with from a macroscopic point of view in the code STADIUM©. Nevertheless, they could successfully use thermodynamic modeling to separate bound and free chlorides. The added value of our work is that we would do away with many of the empirical relations they used to express the permeability or the concentration dependence of the diffusion coefficient for example. Achieving this would give a much broader applicability to such modeling.

The second challenge probably major difficulty is to conduct the experiment in such a way that chloride diffusion would precede unaltered on the top surface of the sample. This is very tricky experimentally. Preliminary experiments with a die containing solution and bricks clearly underlined this as explained below.

Happily for us, both these challenges can be decoupled. Indeed, using destructive sample preparation, it is possible to obtain chloride profiles and work towards a proper local decoupling of bound and free chlorides. Various options are at hand, but we are currently favoring the use of small core drills, sealed on each extremity. These are ponded in a solution and the cut and analyzed. The disadvantage is that in composite materials, we lose the possibility to follow at a specific location the evolution of the chloride content. However, it can resolve in a simpler way most issues of the free and bound chloride decoupling.

For the second challenge, there are numerous options that can and will be considered. Up to now we have only undertaken the simplest possible tests. Much more work will be needed to make this experiment work. It is one of the

major challenges of this project and one for which we consequently do not yet have the solution at hand. Information is given below as to the state of ongoing research.

A.4.3. Preliminary Experiments

As was mentioned before, one of the main challenges of this method is the surface diffusion difference. At this point, initial assessments of geometries for transport of soluble species in porous media have been done for the purpose of finding solutions to the possible problems involved with the technique. There are three models being tested. The designs include an examination of outward radial diffusion (analogous to Transient Hot Wire), another one on inward radial diffusion (small cores submerged in solution), and a third one on 1D diffusion (one flat square surface exposed to solution) (Figure A.6). The 1D diffusion model serves as an alternative for the borehole. We have performed preliminary experiments on all designs using conventional clay bricks as the heterogeneous, porous media, and methylene blue as the diffusive solution.

The specimens were water saturated after the epoxy layers were casted on the appropriate surfaces. After this, they were exposed to the solution for one week and another set for two weeks. The disks were split lengthwise (Brazilian splitting method) after the exposure period. The final diffusion distances were measured using an optical microscope.
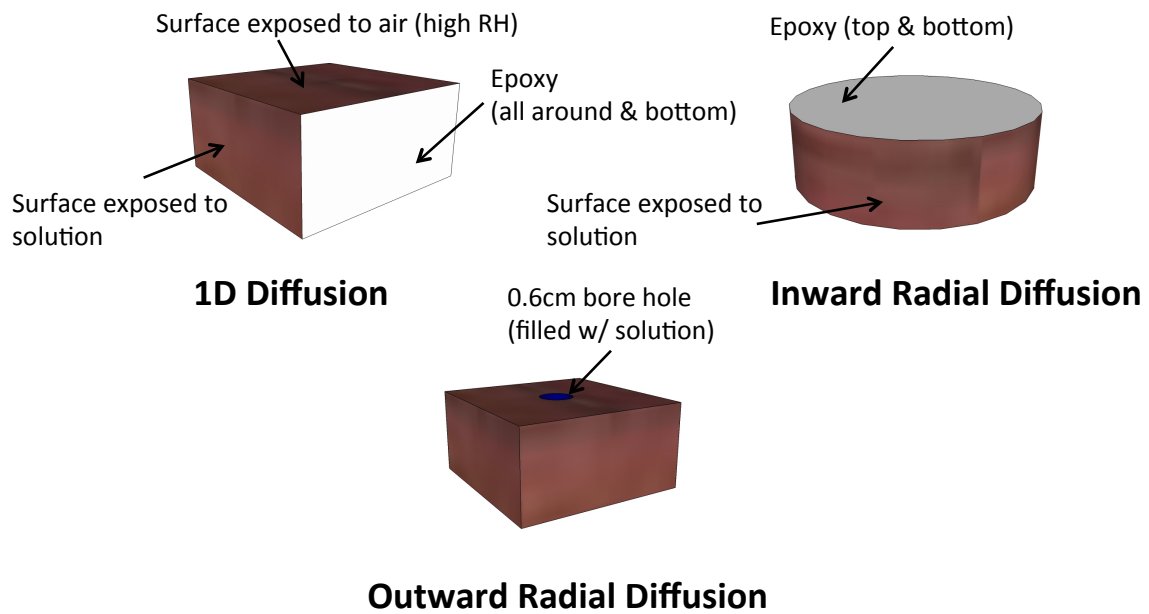
Figure A.6: Sketches of brick prototypes

The idea is to be able to verify our surface measurements with what is happening in the bulk; hence the disks are a suitable design. This technique has potential, as it was discussed earlier that NIST performed some experiments on cylinders exposed to chlorides in a similar manner [33]. NIST demonstrated the feasibility of using μ-XRF to quantify chlorides. We want to go beyond their study to understand what happens at the micron level. Furthermore, for a detailed understanding of the mechanisms of chloride transport in concrete a synchrotron-based μ-XRF might be needed (higher resolution), however this would not be part of the proposed technique.

Surface problems were identified in the following modes:

- The diffusion distance on the 1D and the borehole specimens is very irregular, and it is quite uniform in the disks

- The intensity on those surfaces is higher than in the disks that were split

There are various possible explanations for this phenomenon, which we are presently examining with the objective of defining a more adequate way to conduct these experiments without these artifacts.

A.5.References

[1]   Luping, Tang; Nilsson, Lars-Olof; Basheer, P.A. Muhammed. 2012. *Resistance of Concrete to Chloride Ingress*. New York: Spon Press, 1ᵃ Edition.

[2]   Samson, E.; Marhand, J.; Snyder, K.A. (2003) *Calculation of Ionic Diffusion Coefficients on the Basis of Migration Test Results.* Materials and Structures. 36, p. 156-165

[3]   Angst, U.; Hooton, R.D.; Marchand, J.; Page, C.L.; Flatt, R.J.; Elsener, B.; Gehlen, C.; Gulikers, J. (2012) *Present and Future Durability Challenges for RC Structures.* Materials and Corrosion. 63: 12, p. 1047-1051

[4]   Andrade, C., (1993) *Calculation of Chloride Diffusion Coefficients In concrete From Ionic Migration Measurements.* Cement and Concrete Research. 23: 3, p. 724-742

[5]   AASHTO T259. (1980) *Standard Method of test for Resistance of Concrete to Chloride Ion Penetration.* American Association of State Highway and transportation Officials, Washington, D.C., USA

[6]   Stanish, K., Hooton, R.D., Thomas M.D. (1997) *Testing the Chloride Penetration Resistance of Concrete: A Literature Review.* Department of Civil Engineering, University of Toronto, Toronto, Canada. FHWA Contract DTFH61-97-R 00022. Prediction of Chloride Penetration in Concrete

[7]   ASTM C1202 (1994) *Standard Test Method for Electrical Indication of Chloride's Ability to Resist Chloride.* Annual Book of ASTM Standards V. 04.02, ASTM, Philadelphia, p. 620-625

[8]   SIA 262/1:2003 Betonbau – Ergänzende Festlegungen. Abhang B. Seite 22-24.

[9]   Luping, T.; Nilsson, L-Ø. (1993) *Chloride Binding Capacity and Binding Isotherms of OPC Pastes and Mortars.* Cement and Concrete Research. 23. p. 247–253.

[10]   Marchand, J.; Samson, E. (2009) *Predicting the Service Life of Concrete Structures – Limitations of Simplified Models.* Cement and Concrete Composites. 31, p. 515-521

[11]   Jones, M.R.; McPhee, D.E.; Chudek, J.A., Hunter, G.; Lannegrand, R.; Talero, R.; Scimgeour, S.N. (2003) *Studies Using ^{27}Al MAS NMR of AFm and Aft Phases and the Formation of Friedel's Salt.* Cement and Concrete Research. 33, p. 177-182

[12]   Collepardi, M.; Marcialis, A.; Turriziani, R. (1972) *Penetration of Chloride Ions into Cement Pastes and Concretes.* Journal of American Ceramic Society. 55: 10 p. 534-535

[13]   Ushiyama, H.; Goto, S. (1974*) Diffusion of Various Ions in Hardened Portland Cement Paste.* Supplementary Paper. In: Proceedings of the VI International Congress on the Chemistry of Cement. Moscow, USSR

[14]   Cady, P.D.; Weyers, R.E. (1983) *Chloride Penetration and Deterioration of Concrete Bridge Decks.* Cement, Concrete and Aggregates. 5: 2, p. 81-87

[15]   Helfferich, F. Ion Exchange. New York (USA): McGraw-Hill; 1962, 1st Edition, p.624

[16]   Tamimi, A.K.; Abdalla, J.A.; Sakka, Z.I. (2008) *Prediction of Long Term Chloride Diffusion of Concrete in Harsh Environment.* Construction and Building Materials. 22 p. 829–36.

[17]   Detwiler, R.J.; Whiting, D.A.; Lagergren, E.S. (1999) Statistical Approach to Ingress of Chloride Ions in Silica Fume Concrete for Bridge Decks. ACI Materials Journal. 96, p. 670–675

[18]   Copeland, L. E.; Kantro, D. L.; Verbeck, G.J . Chemistry of hydration of Portland cement. Portland Cement Association, Research and Development Laboratories, 1960.

[19]   Sandberg, P. (1999) *Studies of Chloride Binding in Concrete Exposed in Marine Environment*. Cement and Concrete Research. 29 p. 473–477.

[20]   Luping, Tang. (1996) Chloride *Transport in Concrete- Measurement and Prediction.* PhD Thesis, publication P-96:6. Department of Building Materials, Chalmers University of Technology, Gothenburg, Sweden

[21]   Kulik   D.   GEMS-PSI   2.2.   PSI-Villigen,   Switzerland;   2013. http://gems.web.psi.ch/

[22]   Kulik D.A., Wagner T., Dmytrieva S.V., Kosakowski G., Hingerl F.F., Chudnenko K.V., Berner U. (2013): GEM-Selektor geochemical modeling package: revised algorithm and GEMS3K numerical kernel for coupled simulation codes. Computational Geosciences 17, 1-24.

[23]   Wagner T., Kulik D.A., Hingerl F.F., Dmytrieva S.V. (2012): GEM-Selektor geochemical modeling package: TSolMod library and data interface for multicomponent phase models. Canadian Mineralogist 50, 1173-1195

[24]   Loser, Roman; Lothenbach, Barbara; Leeman, Andreas; Tuchschmid, Martin. (2010) *Chloride Resistance of Concrete and its Binding Capacity- Comparison between Experimental Results and Thermodynamic Modeling.* Cement and Concrete Composites. 32. p. 34-42

[25]   Sugiyama, T.; Ritthichauy, W.; Tsuji, Y. (2008) *Experimental investigation and numerical modeling of chloride penetration and calcium dissolution in saturated concrete.* Cement and Concrete Research. 38, p. 49–67

[26]   Kubayashi, K.; Uno, Y. (1989) *Influence of Alkali on Carbonation of Concrete. Part I, Preliminary Tests with Mortar Specimens.* Cement and Concrete Research. 19, p. 821-826

[27]   Kubayashi, K.; Uno, Y. (1990) *Influence of Alkali on Carbonation of Concrete. Part II, Influence of Alkali in Cement on the Rate of Carbonation of Concrete.* Cement and Concrete Research. 19, p. 821-826

[28]   Angst, U.; Elsener, B.; Larsen, C.K.; Vennesland, Ø. (2010) Potentiometric Determination of the Chloride Ion Activity in Cement Based Materials. Journal of Applied Electrochemistry. 40, p. 561-573

[29]   Elsener, B., Angst, U. (2007) *Mechanism of electrochemical chloride removal.* Corrosion Science 49 4504 – 4522.

[30]   Wang, H.; Grolimund, D.; Van Loom, L.R.; Barmettler, K.; Borca, C.N.; Aeschlimann, B.; Günther, D. (2012) *High Spatial Resolution Quantitative Imaging by Cross-Calibration Using Laser Ablation Inductively Coupled Plasma Mass Spectrometry and Synchrotron Micro-X-Ray Fluorescence Technique.* Chimia 66: 4, p. 223-228

[31]   Wang, H.A.O.; Grolimund, D.; Van Loom, L.R.; Barmettler, K.; Borca, C.N.; Aeschlimann, B.; Günther, D. (2011) *Quantitative Chemical Imaging of Element Diffusion into Heterogeneous Media Using Laser Ablation Inductively Coupled Plasma Mass Spectrometry, Synchrotron Micro-X-Ray Fluorescence, and Extended X-Ray Absorption Fine Structure Spectroscopy.* Analytical Chemistry, 83, p. 6259-6266

[32]   Davis, J.M.; Newbury, D.E.; Fahey, A.; Ritchie, N.; Vicenzi, E.; Bentz, D. (2011) Bridging the Micro-to-Macro Gap: A New Application for Micro X-Ray Fluorescence. Microscopy and Microanalysis, 17, p. 410-417

[33]   Snyder, K. A.; Bentz, D. P.; Davis, J. M. (2012) *Using Viscosity Modifiers to Reduce Effective Diffusivity in Mortars.* Journal of Materials in Civil Engineering. ASCE. August. p. 1017-1024

[34]   Polder, R. B., Peelen, W. H. A., Courage, W. M. G. (2012). Non-traditional assessment and maintenance methods for aging concrete structures–technical and non-technical issues. Materials and Corrosion, 63(12), 1147-1153.

[35]   Samson, E., Marchand, J. (2008) Extending the Service Life of an Existing Structure Using a Predictive Modeling Software. Concrete Bridge Conference.

Appendix B : Standards preparation development

In the process of developing the method, many difficulties were encountered in the preparation of the standards. There was a trial and error process in coming up with the best protocol for preparing the standards. The few trials that we tested before coming up with the final process to make the standard are summarized below:

- The first trial was creating pressed pellets with a mixture of oxide powders containing the same composition as a cement paste. The chloride was added at known concentrations as well. The powders were ground using an automatic pestle and mortar for about 3 minutes. After this the pellets were pressed with a manual press at about 5 tons. This proved to be inconvenient for several reasons.

- To minimize fragility, the pellets were annealed to 600 degrees Celsius for about 20 hours. The pellets were however still too fragile.

- Next, the powders were first milled in a planetary mill for 2 minute intervals at 400 rpm. The pellets were then pressed with a manual press at 350 bar. Although they were more stable, the pellets still cracked very easily if not handled with care.

- The final attempt with the pellets was to use a wax binder in order to keep the pellets together. The powder mixture was mixed at 170 Hrz for 5 minutes with a glass bead inside to homogenize. After that they were pressed at 450 bar for 1 minute. The pellets are strong and were used to measure with the micro XRF. Even though this last attempt worked, it proved to be impractical. For one, the powders were hard to compress and keep together, as they were extremely fragile. And secondly, the matrix was not at all similar to regular cement paste samples, which can considerably affect the results.

- The next trial was to make cement paste samples with known chloride concentrations. The standards were casted in small molds of dimensions 3 by 3 by 1.5 cm^3. The water to cement ratio was 0.6. samples were placed in a 95 % RH room right after casting, and demolded 24 hours after casting. The samples were then placed in a >95% RH box for 28 days before measuring with micro XRF. The measurements were performed on one of the larger surfaces. The results showed a lot of scatter, which suggested that the high porosity might play an important role.

- Next trial was to try to optimize the data collection on the surface of the standards. At first, an area was measured. The maps showed the large scatter in the chloride maps. Instead, 100 points were randomly chosen to measure, and use as data. At the time, the SVMs were still being considered, and the model was providing good results. Considering this, the distance of 2.5 mm mentioned in chapter 3 was found (as the distance after which the cumulative average stabilized in a line scan on the surface of the sample).

- Finally, a lower water to cement ratio was chosen, and given that after cutting the samples and measuring the freshly cut surface showed different results that the original surface measurements, the sample mold was changed to a sealed plastic cylinder. This was the final protocol for the preparation of the standards, and the detailed description can be found in Chapter 3.